Norges miljø- og
biovitenskapelige
universitet

Master's Thesis 2018 60ECTS
Faculty of Sciences and Technology

Thermal Donors in Czochralski Silicon Wafers Investigated by Spectral Imaging

Malin Helander
Enviornmental Physics and Renewable Energy

ACKNOWLEDGEMENT

This thesis will complete my master's degree at the University Of Life Science (NMBU) and I am grateful for getting the opportunity to write my thesis within such an interesting field. As this has not been a straight road in terms of developing and executing this thesis, I would like to take the chance to thank my supervisors Ingunn Burud,Espen Olsen and Torbjørn Mehl for letting me be a part of your group and guiding me in this process. also like to take the chance to thank Rune Søndenå at IFE for the help with this research, by performing parts of the annealing process and sharing his time. I wish to thank Johanne Solheim and Alise Hjellebrekke for five wonderful years together at NMBU. And last but not least, I want to thank Marius for supporting me through these last months and helping in any way possible.

ABSTRACT

In oxygen rich CZ-material, thermal donors (TD) are formed at elevated temperatures of approximately 450°C. They are electrically active clusters of interstitial oxygen that act as double donors to the conduction band. In material that is exposed to higher temperatures donor concentration is reduced and it has been shown that it only takes a short time annealing at temperatures of 650°C to eliminate TDs. By investigating the creation and dissociation of these electrically active centres a fundamental knowledge of oxygen diffusion at elevated temperatures can be found. A study was performed on these electrically active centres with the use of hyperspectral photoluminescence imaging. The method gives both the spectral and spatial resolution of the defect luminescence present in the material. For the study, as cut samples from CZ-silicon material with high and low oxygen was selected. All the samples were exposed to thermal annealing in the range of thermal donors under different conditions. Additionally, a short time anneal was performed at 650°C with the purpose to eliminate possible thermal donors. The annealing was executed in multiple steps to see if a development in the spectral and spatial distribution could be seen with time. It was found that the spectral response in the samples changed drastically with annealing time at temperatures of 450°C. Multiple emission lines was found exhibiting photon energies between 0.66-0.767 eV and the intensity of these emission lines developed significantly with anneal time. The 0.767 eV emission line has been denoted as the P-line in other experimental work. Multiple new emission lines could also be seen in the spectral response at among others 0.807 and 0.9251 eV, and these are known from literature as the D1 and H line. The thermal annealing at 650°C resulted in the disappearance of almost all emission lines in the spectral response besides the P-line. These results show that long time annealing in the temperature range of thermal donors influences the spectral and spatial distribution of defect luminescence in CZ-material and that the method used in this study is suitable for tracking these changes.

CONTENT

1 Introduction 1
2 Theory 3
2.1 Intrinsic semiconductor 3
2.2 Extrinsic semiconductors 5
2.2.1 Direct and indirect band gap 6
2.3 Charge carrier generation and recombination 7
2.3.1 Generation of excess charge carriers 7
2.3.2 Radiative recombination of charge carriers 9
2.3.3 Shockley Read Hall recombination 10
2.3.4 Auger recombination 12
2.3.5 Surface recombination 13
2.4 Monocrystalline silicon 13
2.4.1 Silicon crystal structure 13
2.4.2 Monocrystalline growth 14
2.4.3 Czochralski silicon process 15
2.5 Defects in monocrystalline silicon 17
2.5.1 Impurities 20
2.5.2 Oxygen related defects 20
2.5.3 Spatial distribution of interstitial oxygen 24
3 Defect related luminescence 26
4 Experimental 29
4.1 Sample properties and processing 29
4.1.1 Sample properties 29
4.1.2 Thermal annealing processes 30
4.2 Hyperspectral Photoluminescence imaging 36
4.2.1 The set up 37
4.2.2 Mean spectrum and spatially resolved images 39
4.2.3 Sample properties effect on luminescence spectra. 40
4.2.4 Multivariate Curve Resolution 41
5 Results and discussion 42
5.1 Hyperspectral PL imaging 42
5.1.1 Spectral response as cut wafers 42
5.1.2 Spatial distribution of defect related luminescence - spectral range 0.667-0.767eV 45
5.1.3 Section discussion 46

5.2 Spectral response of thermally annealed seed end wafer 47
5.2.1 MCR analysis of thermally annealed seed end wafers 50
5.2.2 Spatial distribution of defect related luminescence - spectral range 0.667-0.767eV 51
5.2.3 Section discussion of defect related luminescence - spectral range 0.667-0.767eV 54
5.2.4 Spatial distribution of defect related luminescence - spectral range 0.804-0.810eV 57
5.2.5 Section discussion of defect related luminescence - spectral range 0.804-0.814eV 58
5.2.6 Spatial distribution of defect related luminescence - spectral range of 0.895-1.01 eV. 59
5.2.7 Section discussion of defect related luminescence - spectral range 0.895-1.01 eV 61
5.2.8 Spatial distribution of the band to band luminescence. 62
5.2.9 Section discussion of band to band luminescence 63
5.3 Thermal annealing of tail end samples 64
5.3.1 MCR analysis thermally annealed tail end wafers 67
5.3.2 Spatial distribution of defect related luminescence - spectral range 0.667-0.767 eV ... 68
5.3.3 Section discussion of defect related luminescence - spectral range 0.667-0.767 71
5.3.4 Spatial distribution of defect related luminescence - spectral range 0.804-0.810eV 72
5.3.5 Section discussion of defect related luminescence - spectral range 0.804-0.814eV 73
5.3.6 Spatial distribution of defect related luminescence - spectral range 0.895-0.925eV 74
5.3.7 Section discussion of defect related luminescence - spectral range 0.895-0.925eV 75
5.3.8 Discussion across seed and tail end sample sets 75
6 Conclusion 80
7 References 82

1 INTRODUCTION

Over the past centuries there have been a continuous growing demand for energy across the globe. The energy consumption is continuously increasing, and this is happing simultaneously as an increasing pressure for reducing the use of fossil fuel. Both these factors make it desirable to find alternative energy sources. Solar energy production is one the highest expanding alternatives for renewable energy, partly because of the large reduction in production cost. This leaves solar cells as one of the cheapest options for renewable energy today.

Silicon is a crucial part of the Photovoltaics (PV) industry as it is the main material used in commercially produced solar cells. Today the PV modules are primarily made from multicrystalline or monocrystalline silicon, where the former dominates the solar cell market because of its cost advantages. However, monocrystalline silicon solar cells are on average more efficient because of its high-quality material. The quality of the material depends on the production process of the silicon crystal and during the growth of the crystal a number of irregularities can arise in the crystal structure. These are referred to as defects and are reducing the quality of the silicon.

The Czochralski (CZ) [1] technique is commonly used in the growth of mono crystalline silicon ingots. In this process a range of defects can get introduced into the material, these can both be structural defects and impurities as a result of contamination. The biggest challenge in the CZ silicon production lays in reducing oxygen and carbon related defects. Both gets introduced into the material from multiple sources in the production process. There is one defect that is commonly found in oxygen rich material, and is known for affecting the electrical properties of the material [2]. The defect is formed in material that is exposed to temperatures around 450°C for a prolonged time, as at these temperatures interstitial oxygen diffuses and form electrically active clusters [3]. These defects, known as thermal donors, will introduce two new energy levels within the bandgap of silicon and result in that two electrons gets donated to the conduction band [4]. There have been reports of multiple types of TDs placed at different energy levels within the band gap. It has further been suggested that the various types of TDs differ in cluster size, and that larger clusters form with a long annealing time at 450°C [5]. Photoluminescence studies have shown that these energy levels exist both at a deep and at a shallow level in the band gap [6], and emissions that occur due to traps inside the band gap are categorised as defect related luminescence (DRL). Several deep

level DRL emissions have been connected to interstitial oxygen, such as 0.925eV and 0.767 eV, where the latter have been linked to thermal donors [6].

In this work, CZ silicon wafers was exposed to heat treatments at 450°C and 650°C with the purpose of both generating and eliminating thermal donors in the material. These treatments were carried out on samples with both high and low interstitial oxygen concentration in order to compare them. It was expected from the literature that the generation rate of thermal donors would be higher in oxygen rich CZ silicon [3, 7]. Hyperspectral imaging was used as a fast, non-destructive method that provided both a spectral and spatial response of the detected photoluminescence in the material [8]. By using hyperspectral imaging after each annealing process, it was investigated if any or several emissions could be linked to thermal donors or oxygen.

2 THEORY

This chapter aims to present some of the relevant physics and experimental work to motivate the methods used in this thesis, and to aid in analysis and when drawing conclusion from the results. The theory is divided into two parts, where first part build on semiconductor physics and introduce basic concepts around band gap theory, charge carrier generation and recombination paths of charge carries. Second part introduce theory connected to single crystal structure and the production process of CZ-silicon. It will also give an introduction to defects in CZ-silicon, with focus on oxygen related defects and present relevant research on the subject. Unless other is mentioned, the theory and equations in these two sections are taken from references [9, 10, 11]

2.1 INTRINSIC SEMICONDUCTOR

An isolated atom has discrete energy levels which the electrons can occupy. When the atoms are placed far apart the allowed energy states will be identical for all atoms of the same kind. However, in a solid the atoms are closely spaced, and the distribution of the energy levels will be forced to adjust to maintain their discrete nature. This is in accordance to the Pauli exclusion principle, which states that each quantum state can only be occupied by one electron in an electronic system, such as an atom or molecule. As a result, the discrete energy state is split into two levels that differ slightly in energy. With increasing numbers of atoms in close vicinity, this gives rise to energy bands of allowed energy states which the electrons can obtain. This is visually presented for silicon in Figure 2.1.

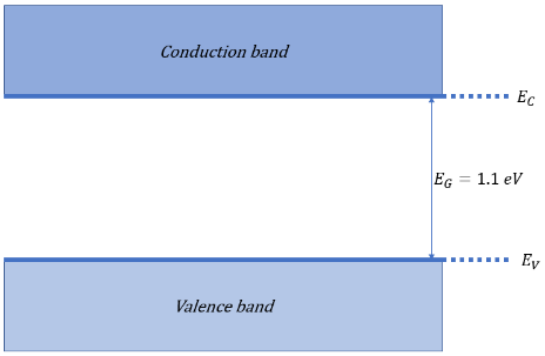

Figure 2.1: A simplified version of the allowed energy bands that form in silicon where the respective energy bands are marked as valance band E_V and conduction band E_C. The distance between the band gaps edges are denoted as the band gap, E_G.

The energy bands are referred to as the valence band and conduction band, and all distances are in units of energy. The distance between the upper valance band edge (E_V) and the lower conduction band edge ($E_{C.}$) is the band gap (E_G), and no electrons can exist inside this gap. The length of the band gap therefore

reflects the minimum energy an electron must obtain to leave its bound state in the valance band and excite over to the conduction band. Naturally, the band gap defines the conductive properties of the material, where the semiconductor material has a band gap length where it is possible for the electrons to excite over to the conduction band. As an electron excite over to the conduction band it leaves behind an empty energy state, a hole, in the valance band. Meanwhile, the electrons that are occupying the conduction band are in a free state. Electrons and holes are both carriers of electrical charge and both referred to as a charge carrier.

By using two assumptions it is possible to derive an expression of the probability of finding an electron at a certain energy state. First, that the material exist in thermal equilibrium, implying that no external forces such as voltage, electrical field, magnetic field or temperature gradients is acting on the material. And second, that the material is intrinsic and therefore free from impurity atoms. This means that no thermal excitation of electrons occur and that all the energy states in the valance band are filled with electrons which leaves the conduction band empty. At temperatures above T= 0K, thermal excitation will occur and the distribution of electrons between the valance band and conduction band changes. The probability of an electron occupying an energy state E at a given temperature T can be described through the Fermi-Dirac distribution in equation (2.1):

$$f(E) = \frac{1}{1 + e^{(E-E_F)/kT}} \tag{2.1}$$

Where E_F is the Fermi energy level that represent the maximum energy level of an electron at thermal equilibrium in an intrinsic material. Under these conditions the position of the Fermi energy level is defined as in the middle of the bandgap. T and k_b is the Boltzmann's constants.
By using the Fermi-Dirac distribution and the Boltzmann approximation, which says that $f(E) = e^{-(E-E_F)/kT}$ for $E\text{-}E_F >> 3kT$, an expression can be derived for the hole concentration, p_0 and the electron concentration, n_0:

$$p_0 = N_V \exp\left(-\frac{E_F - E_V}{k_B T}\right) \tag{2.2}$$

$$n_0 = N_C \exp\left(-\frac{E_C - E_F}{k_B T}\right) \tag{2.3}$$

N_V and N_C stand for the effective density state of the valence and conduction band respectively. When multiplied with the probability of being occupied by either an electron or a hole it gives the respective concentration.

When an intrinsic material is assumed to be in a state of thermal equilibrium the concentration of holes in the valence band is equal to the concentration of electrons in the conduction band.

$$n_0 = p_0 = n_i \tag{2.4}$$

Where, n_i is the intrinsic charge carrier concentration at thermal equilibrium.

2.2 EXTRINSIC SEMICONDUCTORS

In an extrinsic semiconductor the concentrations of holes in the valance band is not equal to the density of electrons in the conduction band. Extrinsic semiconductors are intentionally doped by introducing impurity atoms into the crystal lattice to alter the electrical properties of the material. The elements that are suitable for doping are either atoms with an excess electron, or atoms with a hole in its outer shell. The objective is for an impurity atom to replace a silicon atom in the crystal lattice, and share a covalent bond with the adjacent silicon atom. The doping agents have the purpose of introducing shallow energy levels in the band gap, meaning that the energy levels are close to the edges of either the valance or conduction band. So, when an electron is loosely bound it can act as a donor to the conduction band and increase the electron concentration. The alternative scenario is that a doping agent with an excess hole accept an electron from the valance band and thereby increases the hole concentration. Materials where donors are used are called n-type semiconductors and materials with acceptors are called p-type semiconductors. This introduces the concept of majority and minority charge carries. In n-type semiconductor the majority charge carriers are electrons, meanwhile the holes are regarded as the minority charge carriers. The opposite applies for a p-type semiconductor.

Naturally, the concentrations of holes and electrons in their respective bands can no longer be expressed through equation 2.3 and 2.4. By increasing electron or hole concentration the fermi level will change and therefore adjustment to the derived equation must be done. It is natural to assume that:

$$(E_C - E_F) = (E_C - E_{Fi}) - (E_F - E_{Fi}) \tag{2.5}$$

Where, E_{Fi} is the fermi level for intrinsic semiconductor and E_F for the fermi level for the extrinsic semiconductor. By inserting the new Fermi level into equations (2.2) and (2.3) an expression for the hole and electron concentrations can be derived:

$$p_0 = n_i \exp\left(-\frac{E_i - E_F}{k_B T}\right) \tag{2.6}$$

$$n_0 = n_i \exp\left(-\frac{E_F - E_i}{k_B T}\right) \tag{2.7}$$

Further, it has been proven that the product of the electron and hole concentration for doped semiconductors is constant and equal to the concentration of intrinsic charge carriers:

$$n_o p_o = n_i^2 \tag{2.8}$$

This relationship with intrinsic charge carrier concentration can viewed as a parameter of the semiconductor material. At room temperature the dopant is expected to be completely ionized and will therefore donate its holes or electrons to the opposite energy band. In this situation the equilibrium carrier concentration can be defined as:

$$p_0 = N_A \tag{2.9}$$

$$n_0 = N_D \tag{2.10}$$

Where N_A and N_D are the total acceptor and donor densities. To show how the Fermi level is affected by donor concentration the following expression can be derived:

$$E_F - E_V = kTln\ \frac{N_V}{N_A} \tag{2.11}$$

$$E_C - E_F = kTln\ \frac{N_C}{N_D} \tag{2.12}$$

Showing that the position of the Fermi level is determined by the doping concentration, hence moving toward the conduction band in a n-type material, and the valance band in the case of a p-type material.

2.2.1 Direct and indirect band gap

Semiconductors can have direct or indirect band gaps, depending on the alignment of the band gap edges compared to each other in terms of crystal momentum. Meaning, in direct band gap semiconductors the maximum energy level of the valance band aligns with the minimum energy level of the conduction band In indirect band gap semiconductors maximum and minimum energy levels of the valance and conduction band are misaligned. With direct band gap the electron can excite directly over to the conduction band. For the same to occur in an indirect band gap the electron must first gain momentum from a photon and then be further assisted by a phonon. This is a quantum mechanical manifestation of thermal vibrations in the crystal lattice and results in a particle with low energy and high momentum.

2.3 CHARGE CARRIER GENERATION AND RECOMBINATION

In this section a brief overview will be given of generation and recombination of excess carriers in direct and indirect band gap semiconductors. The reader must note that the physics presented does not have the purpose of providing in depth knowledge of the subject, but only to shed light on the physics behind the method used in the experimental part of this thesis.

2.3.1 Generation of excess charge carriers

When a semiconductor is in a state of non-equilibrium it is operating under new conditions and additional excitation of electrons can occur due to external forces, such as an excitation source (figure 2.2). The product of $n_o p_o = n_i^2$ that was valid for thermal equilibrium is no longer true as there are an excess of electrons and holes in their respective bands. As a result $n_o p_o > n_i^2$ and excess carriers must be considered in the equations for electrons and hole concentrations:

$$n = n_o + \delta n \tag{2.13}$$

$$p = p_o + \delta p \tag{2.14}$$

n and p are the electron and hole concentrations in the conduction and valance band, respectively. In a non-equilibrium state this is the sum of the electrons and holes at thermal equilibrium and excess electrons δn and holes δp.

The rate at which electrons and holes increase in the conduction and valance band is called the generation rate *G*. In thermal equilibrium the generation rates of electrons and holes must appear in pairs, implying that when one electron excites over to the conduction band it leaves behind a hole:

$$G_{th} = G_{n0} = G_{p0} \tag{2.15}$$

Where G_{n0} is the generation rate of electrons and G_{p0} is the generation rate of holes at thermal equilibrium. In non-equilibrium the total generation rate G is the sum of G_{th} and the generation rate of mechanism G' causing excess carriers:

$$G = G_{th} + G' \tag{2.16}$$

Figure 2.2 illustrates how a photon excites an electron over the band gap and into the conduction band and create an excess carrier. When light hit the surface of a semiconductor a photon is either reflected, absorbed or transmitted through the material. When absorbed, it can cause an electron in the valance band to gain enough energy to excite over to the conduction band. For the excitation to occur the energy of the photon must be greater or equal the band gap energy.

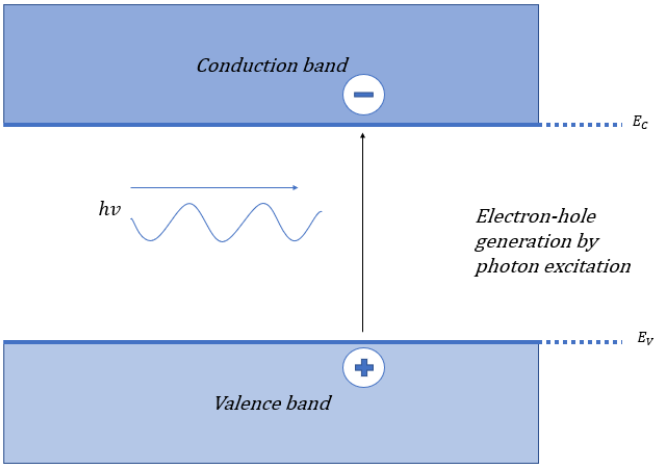

Figure 2.2: Illustration of electron-hole generation by photon excitation.

2.3.2 Radiative recombination of charge carriers

An electron that has been excited over to the conduction band is free and moves randomly in the energy band. Eventually the free electron come in close vicinity of a hole, and this can cause the electron to jump into the hole and fill the empty energy state in the valance band. The rate of annihilation of electrons and holes is denoted as the recombination rate R.

A recombination that occur directly between an electron in the conduction band and a hole in the valance band is said to be a radiative, or a band to band (BB) recombination, and is illustrated in Figure 2.3.

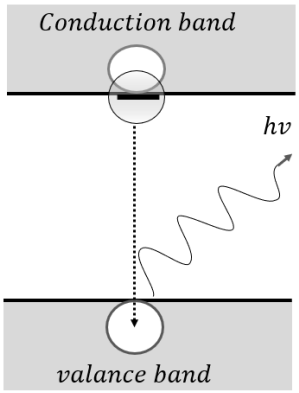

Figure 2.3: Band to band (BB) recombination process where an emission of a photon happens.

In thermal equilibrium the recombination rate of holes and electrons appear in pairs and therefore must:

$$R_{n0} = R_{p0} = R_{th} \tag{2.17}$$

Where R_{n0} and R_{p0} are the electron and hole recombination rate respectively, and R_{th} is the recombination rate at thermal equilibrium. R_{th} can further be expressed as:

$$R_{th} = \beta n_0 n_0 = G_{th} \tag{2.18}$$

Where β is the proportionality constant, also called biomolecular recombination coefficient, which is a parameter of the semiconductor material. For the product $n_o p_o$ to be constant the recombination and generation rate at must be identical. In non-equilibrium an expression can be derived for recombination rate R by using equations (2.13), (2.14) and the product np:

$$R = \beta np = \beta(n_o + \delta n)(p_o + \delta p) \tag{2.19}$$

A net recombination rate is defined as:

$$R_{net} = R - G_{th} = G' \quad (2.20)$$

$$R_{net} = \beta(np - n_0 p_o) = G' \quad (2.21)$$

To simplify the expression further, an assumption of a low injection level can be made. A low injection level means that the concentration of excess carrier is much less than the thermal equilibrium carrier ($n_o \gg \delta n$) and puts limits on the excess carrier concentration compared to the thermal equilibrium concentrations. In a n-type material under low level injection it can be said that ($n_0 \gg p_0$) and that $\delta p \ll \delta n$, and by applying this into equation 2.21 and assuming charge neutrality $\delta n = \delta p$ the following can be derived:

$$R_{net} = \beta n_o \delta p = G' \quad (2.22)$$

The net radiative recombination rate in a n-type semiconductor will therefore be dependent of these three factors. Here it is important to note that the proportionality constant β is connected to the material and will be smaller for indirect bandgaps than for direct band. This is logical considering that the probability for recombination is lower in an indirect band gap.

Continuing the assumption of low level injection the recombination rate can be used to express the minority carrier lifetime for a n-type semiconductor:

$$\tau_p = (\beta n_o)^{-1} \quad (2.23)$$

This life time describes the mean time between generation and recombination of a minority carrier. In other words example, it shows the average time it takes from a hole is generated by an excitation to it is filled with an electron.

2.3.3 Shockley Read Hall recombination

Defects in the crystal lattice in the form of impurity atoms and structural deformity can introduce energy levels within the band gap. These energy levels are referred to as traps within the band gap and can act as recombination centres for electrons and holes. The probability of recombination at an empty trap is higher than a band to band recombination, because the energy needed to recombine with a trap is less, and the net distance must be shorter than between the band gap edges. At the event of a recombination of an electron-hole pair in a trap, a photon can be emitted. The energy of the photon will depend on the energy needed for the electron to transition from its current state to the trap, and the photon energy emitted from a recombination at a trap inside the bandgap will be less than the bandgap energy.

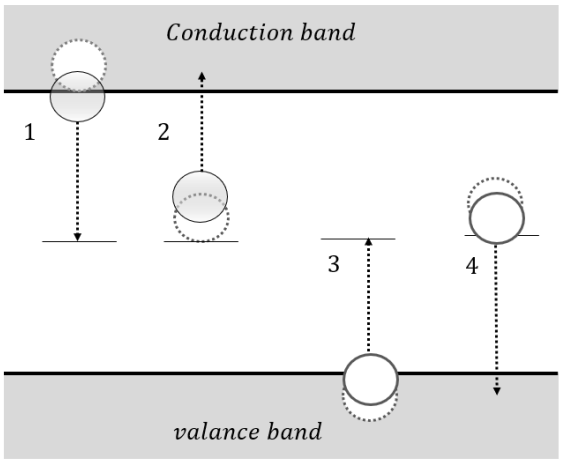

Figure 2.4: An illustration of the four recombination paths that can by SHR, 1) capture of an electron from the conduction band, 2) the emission of an electron from a trap to the conduction band, 3) capture of a hole from the valance band and 4) the emission of a hole from the trap to the valence band.

The recombination at a trap can happen through the four paths presented in Figure 2.4 which are described below:

1. The capture of an electron from the conduction by an empty trap
2. The emission of an electron from a trap to the conduction band
3. The capture of a hole from the valance band by a trap occupied by an electron
4. The emission of a hole from a trap to the valance band

At point 1 and 3 the traps act as generation and recombination centres and affect the excess carrier concentration in their respective energy bands. In the other two the level act as trap centres. In addition, an electron in the valance band can be captured by a trap and further emitted from the trap into the conduction band and counted as a generation process. The opposite can occur and is then seen as a recombination process.

The non-radiative recombination rate through a deep level trap with a trap energy E_T and concentration N_T is given by:

$$R_{SRH} = \frac{v_{th}\sigma_n\sigma_p N_t(pn - n_i^2)}{\sigma_p(p + p1) + \sigma_n(n + n1)} \qquad (2.24)$$

Where $n1 = N_C e^{\frac{-(E_C - E_T)}{kT}}$ and $p1 = N_V e^{\frac{-(E_T - E_V)}{kT}}$ are the SHR densities if the fermi energy is located at the trap level v_{th} is the thermal velocity of the electrons, σ_n and σ_p are the capture cross sections of the traps. For a more extensive derivation of the expression the reader is encouraged to read literature [9]. With equation (2.24) as a basis the lifetime τ_{SHR} can be expressed as:

$$\tau_{SRH} = \frac{\tau_{n_o}(p_0 + p_1 + \delta n) + \tau_{p_0}(n_o + n_1 + \delta n)}{p_0 + n_0 + \delta n} \quad (2.25)$$

The traps can be categorised as shallow and deep traps depending on their distance from the band gap edges. A deep trap is located in the proximity of the centre of the band gap while shallow traps are found closer to one of the bandgap edges. The deep traps are the most effective recombination centres, which also can be found by looking at the SHR densities $n1 = N_C e^{\frac{-(E_C - E_T)}{kT}}$ and $p1 = N_V e^{\frac{-(E_T - E_V)}{kT}}$. if the trap E_T is located at the intrinsic fermi energy, E_F, (middle of the bandgap) then both n1 and p1 will be small and the recombination rate will be higher. i.e. making them effective recombination centres.

2.3.4 Auger recombination

In the Auger recombination process three particles are involved. At the recombination of an electron-hole pair the energy is transferred over to an additional charge carrier and cause it to excite deeper into the energy band. When an electron-hole pair releases its energy as phonons it is seen as thermalization in the crystal and through this energy gets transferred to a third charge carrier as illustrated in Figure 2.5.

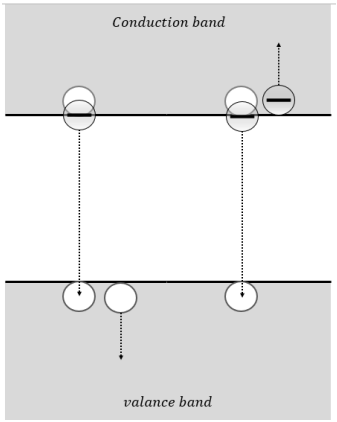

Figure 2.5: The Auger recombination process, an electron-recombination cause an additional charge carrier to excite deep in to the energy bands.

The Auger net recombination rate is expressed as:

$$C_n(n^2p - n_0^2p_0) + C_p(np^2 - n_0p_0^2) \quad (2.26)$$

Where C_n and C_p is the Auger coefficients based on the material. The Auger recombination rate is either proportional to n^2p or p^2n depending on if the reaction mechanism is being an electron-electron-hole process or an electron-hole-hole processes. The Auger recombination lifetime can be derived for low level injection (LLI) in a n-type material:

$$\tau_{auger}^{LLI} = \frac{1}{C_n N_D^2} \quad (2.27)$$

Where N_D is the density of donor concentration. This shows that the Auger life time goes down with higher doping levels.

2.3.5 Surface recombination

At the surface of a semiconductor material the periodicity of the crystal structure is broken. As a consequence, the atoms at the surface are left with unbonded atoms (dangling bonds) that are unfilled energy states that can be located inside the bandgap and act as recombination centres. The dangling bonds can also rearrange themselves and form bonds with neighbouring atoms and obtain energy states inside the bandgap. These energy states will be continuously distributed over the band gap. Because of this there will be high competition between recombination paths and the radiative recombination rate can be expected to be lower at the surface. As the bonding structure is dependent on the specific nature of the material surface it is challenging to find an expression that precisely explain the physics. But it is important to note that surface recombination is a part of the possible recombination paths and should be considered as a factor in the total lifetime of the semiconductor.

2.4 MONOCRYSTALLINE SILICON

The solid form of silicon has a band gap length that makes it suitable as semiconductor material and is appropriate for the production of a large variety of electrical components. This makes silicon the most commonly used material in wafer production for solar cells. There are several methods for producing silicon crystals, and monocrystalline silicon is known to result in wafers with high purity. The quality of the material is crucial for both efficiency and reliability, and is highly dependent on the production process. Defects in the material can cause unintended changes in resistivity and in worst case be detrimental for the device yield. Most defects in the silicon crystal have their origin in some structural irregularities, and this chapter will give an introduction of the defects that is relevant for this thesis.

2.4.1 Silicon crystal structure

Silicon is one of the most abundant elements in the earth's crust and is a member of group IV in the periodic table [11]. Silicon have four valance electrons and therefore four short from completing its valance energy shell. To fulfil the energy shell, silicon atoms favours to form covalent bonds with its neighbouring atom.

In a crystal structure the atoms arrange themselves in tetrahedral manner [12]. Figure 2.6 shows tetrahedral placement of silicon in a unit cell, which is a small volume of the crystal, and when appearing repetitively it forms the crystal lattice. One of the dots inside the unit cell represent a lattice point. The

bonds in a tetrahedral structure are strong and give silicon crystal a high melting point of approximately 1414°C [1].

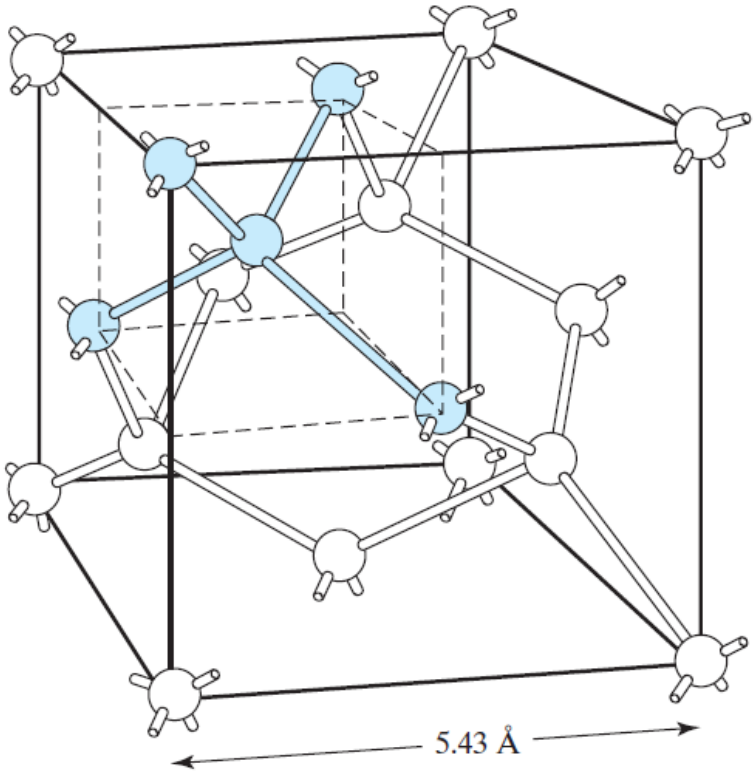

Figure 2.6: Unit cell of the tetrahedral structure of silicon, where the atoms marked in blue are neighbouring atoms in the structure. Illustration borrowed from [12]

In a perfect single crystal the atoms are arranged in a continuous pattern without any boundaries. The crystal is absent of point, linear and planar defects. But in reality, crystals are exposed to imperfections in its lattice due to crystal growth defects. This prevent it from being completely pure and can alter the physical properties of the crystal. If compared to other crystal forms, the single crystal material has high degree of order, as it is free from grain boundaries that are prone to accumulate impurities [11].

2.4.2 Monocrystalline growth

To obtain silicon in a pure form it must be extracted from sands and quartz which are made from silica (SiO_2). The extraction is performed chemically by using carbon and is the main process step to produce polycrystalline. The first process results in low purity silicon (metallurgical-grade silicon) as iron and aluminium is also present in sand or quartz. To obtain semiconductor grade silicon two additional purification steps are performed. First, a distillation step where metallurgical-grade silicon reacts with hydrogen chloride (HCl) and produce trichlorosilane ($HSiCl_3$). Second, usually the Siemens process is used which is a high energy process step that grow polycrystalline silicon at high temperatures, and where hydrogen react with ($HSiCl_3$) and produce HCl and silicon. [13]

Once polycrystalline silicon is obtained, the conversion into single crystal silicon is done through the Czochralski (CZ) or Float zone (FZ) process. In both processes, single crystal is pulled from the polycrystalline melt and formed into ingots. Both methods result in a high purity material and ingots that can consist of 99.997% silicon atoms [1]. The various techniques differ in production costs, growing speed and slightly in purity. CZ-process is favoured due to its fast production rate and cost, and is the most common process for creating single crystal silicon used in technology today, even though the FZ-process result in slightly higher purity.

Due to the high melting point of silicon, there are challenges when it comes to contaminations during the growing process of the ingots. Between the two processes, CZ-silicon is more exposed to oxygen impurities than FZ-silicon, which on the other hand is more exposed to carbon contamination. The sources of contamination in CZ silicon has it origin in the production process. [1]

This chapter will continue by giving a more detail explanation on the production steps and main impurities of Czochralski silicon, while FZ silicon is not in the scope of this paper.

2.4.3 Czochralski silicon process

This section will give an overview of the Czochralski technique, with the main component of the furnace and the growth process of the ingots. Unless other is mentioned, the theory in this section is extracted and combined from references [1] [14]

Czochralski furnace

The Czochralski process take place in an isolated furnace that is equipped with the components represented in Figure 2.7. The chamber inside the furnace is split into a hot and a cold zone, where the first zone is for the melt of polycrystalline and growth of the crystal. The second zone is the area for the finished ingot to grow into and cool down and is conventionally referred to as the puller. For a controlled atmosphere an inert gas is used to flush down on the growing crystal to cool it through convection, and simultaneously has the purpose of flushing away silicon monoxide (SiO) that evaporates from the melt zone. Water is used as a cooling element in a shell around the chamber to maintain stable temperatures.

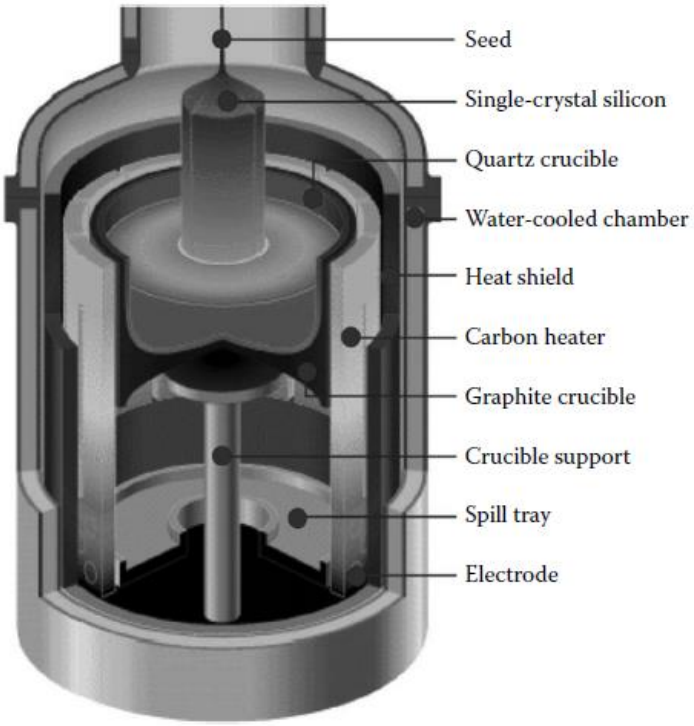

Figure 2.7: Inside of Czochralski furnace, where the sing crystal is pulled by a seed and grow into a solidified Czochralski silicon ingot. Borrowed from [1].

In the hot zone polycrystalline pieces gets fed into a crucible and is melted from the sides by a graphite heater. The crucible material must sustain temperature of at least 1417°C, be chemically inactive and maintain thermal stability. These requirements limit the options of crucible material and a commonly used material is silica, which is structurally strong up to 1450°C. The crucible is supported by an external graphite crucible that is not in physical contact with the melt.

Growth of the Czochralski ingot

To initiate the growing process a silicon crystal seed is lowered into the cooler surface of the melt. Through rotating motion of the pulling rod solidifying crystal gets pulled out of the melt and the CZ crystal ingot starts to form, and the first solidified part of the ingot is called the crown or seed. When continuing the growth process a cylindrical shaped rod is formed until the end of the ingot which is referred to as the end-cone or tail.

Thermal history of the ingot

During the growth of the ingot the silicon will go from liquid form into a solidified crystal. It is likely to assume high variations in temperature gradient inside the furnace, from the melt surface and up to the seed end of the ingot. As the seed end is the first solidified part it will experience the lower temperatures in the cold zone for a prolonged time compared to the tail end that is the last solidified part. Therefore,

the thermal history of the crystal will vary along the length of the ingot and cause deviation in defect distribution. Mapping the thermal history and providing a concrete overview of the temperature gradient inside the chamber is extremely challenging. Most experimental work done on this subject is limited to point measurements or simulations, where Figure 2.8 shows simulations done by E. Dornerberger [15]. It presents the temperature distribution along a 4" crystal, where each isotherm is spaced in steps of 25K. These simulations were performed for three different models and compared with experimental results, and the temperature gradients in Figure 2.9 is show the M2 model plotted in the graph. The seed end will typically experience a temperature around 400°C for an extended amount of time before the finished crystal is sent up to the upper chamber for cooling down.

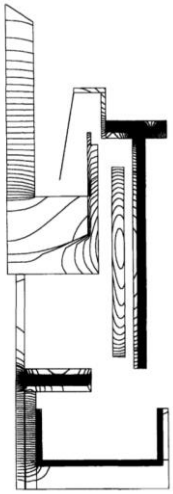

Figure 2.8: Temperature distribution along a 4" crystal measured by E. Dornerberger. The picture shows half a furnace, and each line represents a 25K difference in temperature. Created from the simulations of M2 model in figure 2.9. [15]

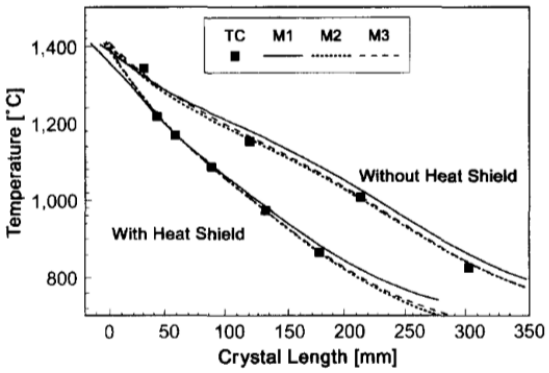

Figure 2.9: shows the graph of the simulations connected to the isotherms in figure 2.9. Computed (M1, M2 and M3) and measured temperatures (TC) in one crystal with and without heat shield. Crystal length 0mm corresponds to the melt surface [15].

The temperature profile will in addition be influenced by the diameter of the ingot since the heat transfer is dependent on the thickness of the material. This is because the surface of the ingot is the first to cool down [14].

2.5 DEFECTS IN MONOCRYSTALLINE SILICON

Imperfections in the crystal structure are viewed as defects and creates points or regions in the lattice that deviate from the perfect crystal structure. One deviation could be the result of an impurity atom, an absent silicon atom in one of the lattice point in the tetrahedral structure and so on. The extent or occurrence of defects mostly comes from the circumstances in which the crystal was pulled.

This chapter will now categorise and discuss these defects. First on a superior level and then down to a more detailed discussion on relevant defects for this thesis. Unless other is mentioned, the theory in this section is extracted and combined from references [11] [14] [13]

Point defects

A point defect occurs at or around a single lattice point and can be classified as an intrinsic or extrinsic defect.

An *Intrinsic* defect arise when a silicon atom is not at its lattice point, implying that it is either displaced or absent, and is called a self-interstitial or a vacancy defect respectively. A self-interstitial is a silicon atom that occupy an interstitial site in the lattice, and a vacancy describes an empty lattice site that leaves its neighbouring atoms with dangling bonds. Both are illustrated in Figure 2.10 and shown as a.) and b.).

Extrinsic point defects are foreign atoms in the lattice that can either be substitutional or interstitial. A substitutional point defect occur when a foreign atom is incorporated at a one of the lattice sites, see Figure 2.10 c.) and d.). Substitutional atoms can be intentionally introduced into the crystal to manipulate the conductive properties of the material and is then referred to as a dopant. When a foreign atom is unintentionally present in the crystal structure it is viewed as an impurity and can lower the quality of the crystal. In CZ-silicon the most common impurities are interstitial oxygen, substitutional carbon and to some extent transition metals. The origin and effects of these impurities will be discussed in its own chapter.

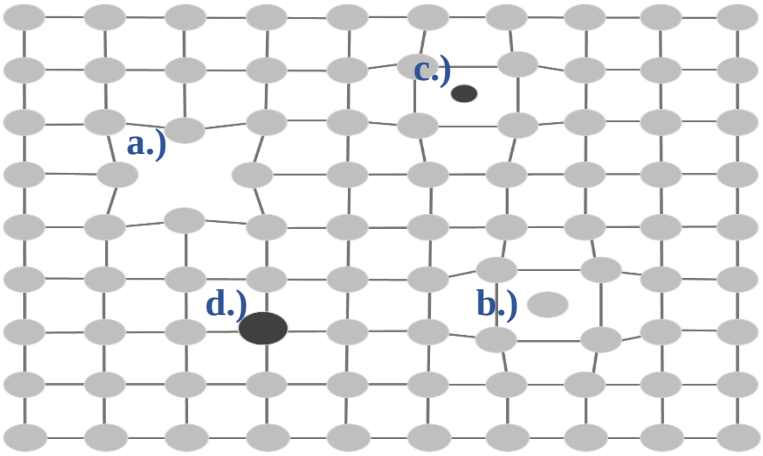

Figure 2.10: Types of defect in the crystal. a.) illustrates a vacancy defect and b.) a self-interstitial defect. Both are versions of intrinsic defects. c.) is an interstitial defect, while d is a substitutional defect, and both referred to as extrinsic defects.

Line defects involves rows of atoms and not just small regions or points. Agglomeration of point defects can create a line of defects across the lattice. Line defects like these are called dislocations and can

consist of a row of vacancies or interstitials through the lattice. They can further be categorized into edge dislocations and screw dislocations. As dislocations is not a part of this thesis it will not be presented in depth. But as the edge dislocation is easy to visualize it can be beneficial to give small introduction to create an understanding on how these dislocations can form. Edge dislocation can be described by viewing it as a simple cubic crystal, and come from a missing or additional line in the lattice.

Figure 2.11 under shows an edge dislocation in a simple cubic structure with an additional half column of atoms in the middle of the lattice. It creates a dislocation line along x direction in the lattice where these connect. Along the dislocation line the neighbouring lattice planes are forced to bend to adjust from the additional half lattice. This will cause a strain on the lattice plane and the areas in its vicinity. Above the dislocation the crystalline structure will be preserved and not affected by the line defect.

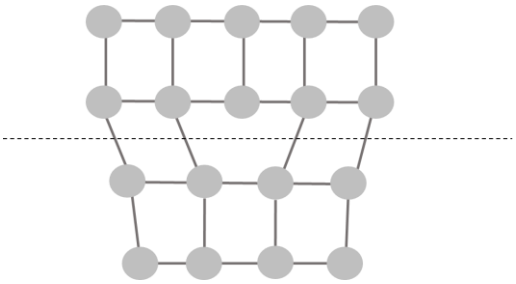

Figure 2.11: Edge dislocation defect in a simple cubic structure.

Spatial distribution of point defects

The distribution and extent of point defects can be manipulated in the growth process of the crystal. As it involves both complex melt and temperature patterns only a general overview will be given on the subject.

In the CZ-process the seed rotates in an upward motion and pull crystal out of the liquid-solid interface. Simultaneously the crucible rotates in an opposite direction to stabilize the melt flow and control the oxygen concentration in the crystal. Therefore will rotation speed, pulling rate and axial temperature gradient at the liquid-solid interface all be important parameters that are crucial to the quality of crystal and the distribution of defects [14].

V.V. Voronkov showed that the distribution of interstitials clusters and voids (vacancies in an extended region in the lattice.) can be controlled by the ratio V/G, where V represent the growth rate and G the axial temperature gradient at the liquid – solid interface [16]. Interstitials are mainly introduced into the crystal by diffusion during the cooling. Diffusion rates are temperature dependent, hence the temperature gradient is an important parameter in controlling interstitials. Vacancies are created by the rotational

parameters, which depend on the crystal growth velocity. The value of the ratio V/G varies among manufacturers.

2.5.1 Impurities

Impurity atoms can get incorporated into the crystal through multiple contamination sources, both from the CZ-process and from the polycrystalline silicon itself.
Table 2.1 give an overview of the impurities found in CZ material and the possible sources of contamination. The concentrations of the impurity atoms are not uniformly distributed throughout the ingot, and there will be areas that is more prone to accumulate one type of impurity compared to others [14] [13].

Impurity	Main contamination source
Oxygen	Quartz crucible Polycrystalline slabs
Carbon	Graphite components Polycrystalline slabs – silicon carbide (SiC.)
Iron	Polycrystalline slabs

Table 2.1: Main sources of contamination of the silicon CZ-growth

It is important to note that the concentration of interstitial oxygen will be substantially higher compared to the other contaminants. Interstitial oxygen is incorporated into the whole ingot, with the highest concentration in the seed end [14]. The contamination source for oxygen is mainly the quartz crucible where oxygen diffuses into the melt, but oxygen is also present in significant concentrations in the polycrystalline slabs and will naturally cause some contamination. A deeper discussion on the distribution and effect of oxygen is covered in the next subchapter. The second most common impurity is carbon with the main contamination sources being the graphite components around the chamber. The presence of carbon in the melt and in the solidified ingot has been connected to the concentrations of CO in the chamber as it can decompose into carbon and oxygen in the melt.

2.5.2 Oxygen related defects

Oxygen can get introduced into the crystal by multiple channels, where the crucible and the feedstock material polycrystalline are the main sources. When oxygen gets incorporated into the crystal it places itself as an interstitial in the lattice. As suggested by Kaiser in 1957, an isolated interstitial oxygen (O_i) atom is believed to bond with two neighbouring silicon atoms as in Figure 2.12, and an O_i in this type of configuration will be electrically neutral [3]. High O_i concentrations can give rise to several types of

defects such as oxygen precipitates and thermal donors (TD) [17, 3]. These defects are formed under different temperature ranges and the effect they have on the crystal varies between the defects.

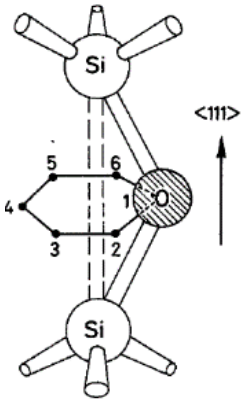

Figure 2.12: Kasier's suggested configuration of one interstitial oxygen in silicon. And the six possible positions of the oxygen atom. [7]

Thermal donors

Thermal donors are electrically active clusters of interstitial oxygen that form in the temperature range of 400-500°C [2]. TDs act as double donors to the conduction band and give undesirable changes to the electrical properties of the material, and introduces two energy levels inside the bandgap [6].

The structure of these clusters has been extensively investigated but is yet to be fully understood.

The first reports of thermal donors were done as early as 1956 by C.S Fuller where it was discovered that CZ-silicon exposed to heating temperatures of 400-500°C caused a significant increase of donor concentration [2].This result was found through resistivity measurement where the electron concentrations could be estimated. When exposed to long annealing time in the temperature range of 320-500°C the donor concentration eventually reached a maximum, and with continued heating a slow decrease started before reaching what is viewed as an equilibrium state. The required time to reach a maximum depended on temperature and ingot position of the sample. When the samples were exposed to anneals at temperatures around 600°C and above the experiment showed a rapid decrease in donor concentration and ended up with in pre-anneal donor concentrations (see Figure 2.13, Figure 2.14 and Figure 2.15).

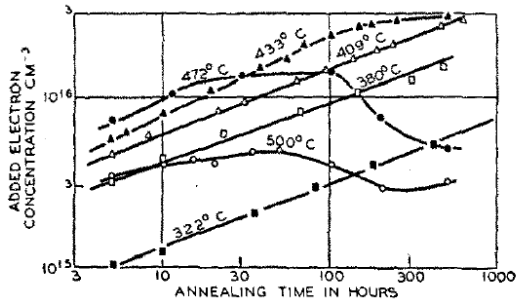

Figure 2.13: One of the plots from C.S fullers research in 1958, showing added electron concentration against time for various temperatures of anneal. It shows that a maximum electron concentration can occur, before going down to an equilibrium. This is dependent of the temperature. Plot borrowed from [2]

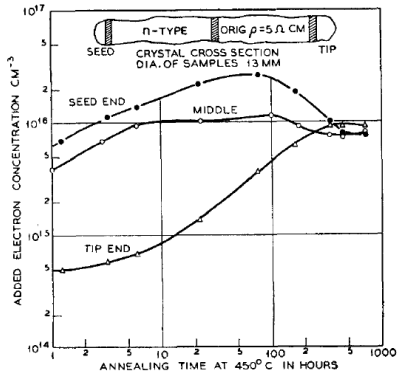

Figure 2.14: Another of the plots from C.S Fullers research. Here the added electron concentrations against time for various samples taken from different ingot parts. It shows a more rapid increase in donor concentrations for seed end sampels. Lowest in the tip end. Plot borrowed from [2].

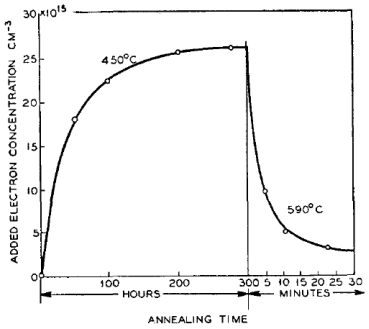

Figure 2.15: Another of the plots from C.S Fullers research. Here illustrating the change of electron concentration with time for a typical Si crystal annealed at 430°C and subsequently at 590°C. A rapid decrease can be observed at the higher temperatures. Plot borrowed from [2].

The results made by C.S fuller was followed by Kaisers establishment of the presence of interstitial oxygen in silicon. Kaiser found that the initial rate of the donor concentration was proportional to the fourth power of the exitance of O_i and at the donor maximum it proved to proportional to the third power of the existence of O_i [3]. He was therefore the first to draw the first link between TDs and O_i. Since then extensive experimental work have confirmed that interstitial oxygen is involved in the generation of thermal donors. The consensus in present time is that it exists multiple types of TD that have a common core, into which oxygen agglomerates [18]. The size of these clusters has been proposed to be affected by the annealing time [19], and each type of TD will introduce an energy state in the band gap and act as a double donor. [18]

The decrease of TDs after reaching its maximum (seen in figures 2.13 and 2.14) have been reported of in other published work and the dependency on O_i concentrations and the annealing time needed to reach this maximum is well established [7, 3, 17].The generation rate of TD is most probably affected by other point defects in the material as these could interact with the diffusing oxygen. As an example, high

concentrations of carbon have shown an inhibiting effect in the formation of TDs, proposed to be due to creation of CO-complexes [19]. There are conflicting reports on which role self-interstitials or vacancies play in the structure, but a recent study done by Voronkov in 2012 showed that higher concentrations of self-interstitials (Si_i) had an enhancing effect on the thermal donor generation rate and therefore indicated an involvement [20].

Temperatures above 600°C causes the defect behind TDs to disappear, and these temperatures seem to be enough to cause the O_i atoms to out-diffuse from their specific centres. Only a short time anneal is needed for donor concentrations to reduce significantly, as seen already in 1956 (Figure 2.15). In a more recent work by Götz, the elimination process of thermal donors was performed on samples with both high and low concentrations of TDs [21]. The samples were exposed to temperatures in the range of 520-700°C and the results showed that donor concentration reduced in the sample with high initial TD concentration. But increased in the sample with low initial TDs concentration. Figure 2.16 show one of the results found by Götz, here presenting the a.) electron and b.) O_i concentrations at annealing temperatures of 550°C. Similar results was obtained when the annealing was performed at higher temperatures, only at a higher rate.

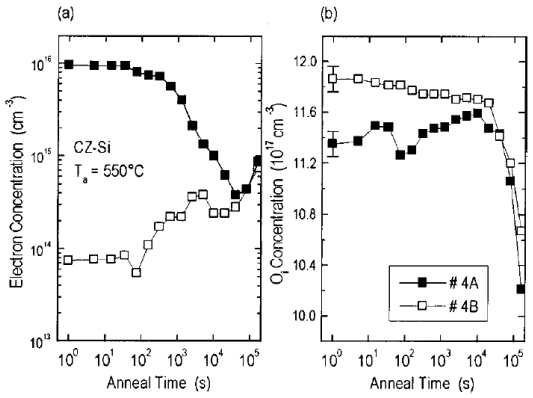

Figure 2.16: Electron contentration (a.) and interstitial oxygen concentration (b.) against anneal time for sample pair No. 4A/B. Sample No. 4A contained a high and sample 4B contained a low initial concentration of TD. It can be observed an increase in electron concertation in 4B and a decrease in 4A. Plots are borrowed from [21].

Oxygen precipitates

Oxygen precipitates are outside the scope of this study but will be briefly introduced as it is a part the behaviour of oxygen at high temperatures. Precipitates are small particles that are introduced into the matrix by solid state reactions in the crystal. They develop at high temperatures around 1000-1200°C and form at nucleates that have been created at temperatures between 600-900°C [4]. As explained by R.C Newman precipitates develop at random sites in post growth anneals in dislocation free CZ silicon

where they can act as sinks for other impurity atom such as fast diffusing metal atoms [17]. This is a positive effect as transition metals are considered detrimental for device yield in semiconductor material.

2.5.3 Spatial distribution of interstitial oxygen

The distribution of oxygen along the ingot length depend greatly on the conditions of the growth process. The silica crucible has been identified as a main contamination source, and the dissolution of the silica crucible can be expected to be highest at the walls as these will be closest to the graphite heater at the sides. The dissolution rate, thermal convection, forced convection, and surface evaporation are all complex parameters that interplay in the result of the distribution of interstitial oxygen and are further illustrated in Figure 2.17 [14].

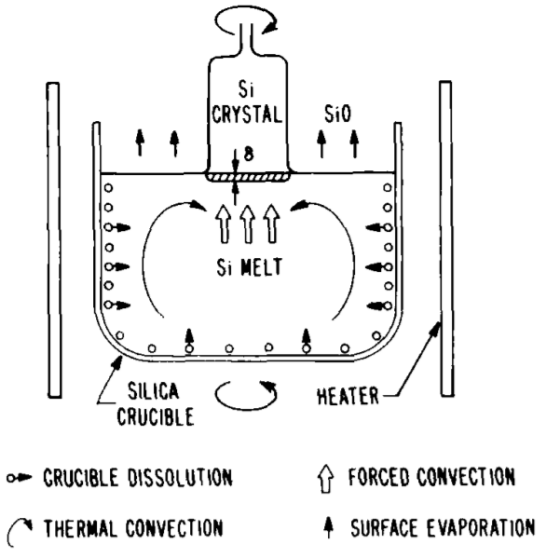

Figure 2.17: Parameters that affect the how interstitial oxygen gets incorporated into the crystal. It will determine the distribution and concentrations of oxygen in the ingot. The parameters that are listed are the following; Oxygen dissolution from crucible, thermal convection, forced convection and surface evaporation. Illustration borrowed from [14].

As all these parameters are both hard to control and measure, there is no definite answer of how oxygen is distributed in in every CZ-ingot. But some major characteristic traits have been reported of in literature, most importantly that the highest concentration of interstitial oxygen is expected to be toward the seed and declining towards the tail end. This is partly a result of a reduced contact surface between the silica crucible walls and melt at the end of the growth process, and here the dissolution rate of the crucible plays a significant role [14, 1]. Smaller concentrations can generally be seen toward the edges of the ingot, which is suggested to be an effect of surface evaporation. Lin and Benson performed a study on oxygen evaporation from the melt surface and the concentrations along the crystal diameter (see Figure 2.18) At small diameters in the initial part of the growth process the oxygen evaporation was

very sensitive to diameter change. It was further found that when the diameter covered the majority of melt surface a stabilization of the evaporation at the melt occurred [14].

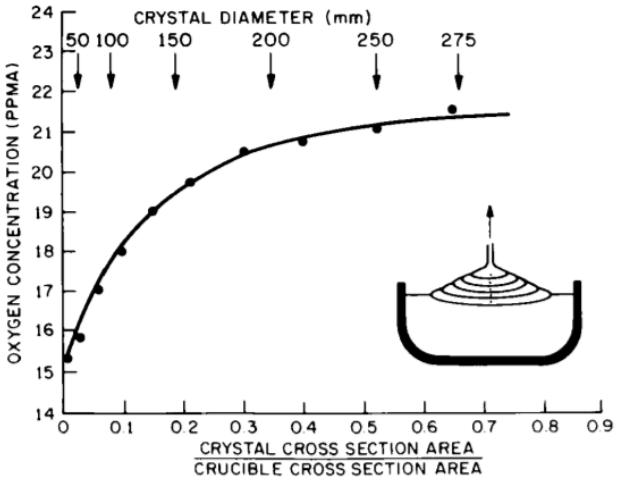

Figure 2.18: Oxygen concentration is measured as a function of the fraction of melt surface, the area covered with crystal at the melt surface. Where oxygen concentrations stabilize at larger diameter. Borrowed from [14].

In addition, changes in the parameters discussed above could cause fluctuations in the growth rate and result in swirl pattern. Defects created by interstitials, vacancies and impurities have all shown tendencies to be distributed in these type of ring patterns. A connection has therefore been made between interstitial oxygen concentration and these ring structures. Work done by T. Niewelt, in 2014 found that the spatial distribution of the rings were in fact connected to interstitial oxygen [22]. In the same study it was performed several annealing steps at 450°C, and the result showed a change in the distribution of the ring pattern and elevated TD concentrations in the same regions.

3 DEFECT RELATED LUMINESCENCE

Luminescence can be used to detect an emission of a photon. If this occurs in the recombination process at a trap inside the band gap, the luminescence will be observed with an energy that is lower than the bandgap. Hence the name defect related luminescence (DRL), and the detection and measurement of DRL signals in a material can be used to map the origin of the defect. The conventional methods are based on single point measurements, which give the spectral response of the photoluminescence in a limited region of the sample [10]. The peaks seen in the spectral response will be equal the energy difference between the initial energy state and the final energy state at which recombination of the charge carrier occur, and this is as explained in section 2.3.3.

There exists extensive literature on DRL related to CZ-silicon where conclusions have been drawn towards oxygen related defects and dislocations. One of the first reports of DRL connected to oxygen was presented by Minaev and Mudryi in 1981 [23], where thermally induced defects in silicon containing oxygen and carbon was investigated. Multiple long-time annealing steps at 450°C was performed on CZ silicon with both high and low oxygen and carbon content.The same was done on FZ silicon with high carbon content and very low oxygen content. Some of the spectral response of the DRL detected from the samples can be seen in Figure 3.1. The growth of numerous DRL peaks can be seen in the spectral range of 0.75 – 1.20 eV after all the respective annealing steps. Minaev and Mudryi drew connections between oxygen and the DRL peaks at 0.767 eV (P-line.) and 0.925 (H-line.).

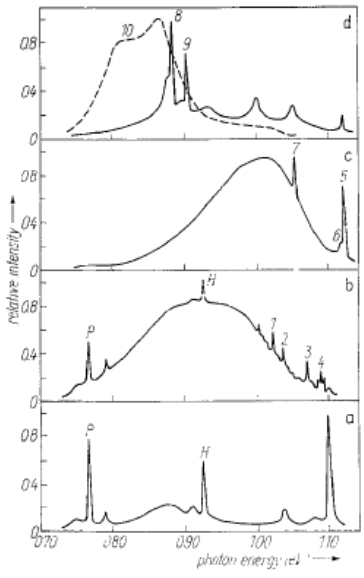

Figure 3.1: Photoluminescence spectra of oxygen rich CZ-1 n-Si crystals after heat treatment at 450C during: a.) 1h, b.) 100h, c.) 200h, d.) 300h (the full line.), 450h (dashed line.), the spectra show multiple emission bands that forms under heat treatment at 450°C. Plots are borrowed [23].

In 1983 Tajima established a connection between interstitial oxygen, thermal donors and the emission signal at 0.767. In a wide study of over 60 commercially produced n-type CZ-silicon samples the P-line appeared consequently when heated at 450°C for 24 hours, and then disappeared at annealing temperatures above 550°C [6]. Simultaneous measurements of interstitial oxygen and TD concentration were performed. As other research discussed in section 2.5.2 it showed a connection of TD generation and annealing time at 450°C, and it further presented a dependency between interstitial oxygen concentration and the intensity of the P-line as demonstrated in Figure 3.2 a.) and b.). A Close relation can be seen between the two at annealing temperatures of 450°C. In the same work it was suggested that the 0.925 eV signal was caused by a CO complex, produced from oxygen and carbon at the same annealing temperatures, as it appeared at strong intensities in samples with carbon concentrations above $4x10^{16}$ cm^{-3}.

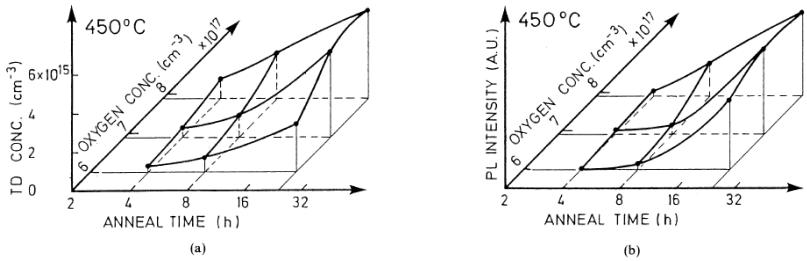

Figure 3.2: (a.) The change in TD concentration vs annealing time at 450C and on initial oxygen concentration. (b.) PL intensity of the P-line at 77 K vs annealing time at 450C and on initial oxygen concentration. Borrowed from [6]

Hyperspectral PL imaging is another method that is suitable for detecting DRL, as the method provides both the spectral and spatial distribution of the defect over the entire sample. Mehl was the first to use this method on CZ-silicon wafers in 2017 [24]. It showed that the DRL signal of 0.767eV was distributed in a ring-like pattern and that regions showing high intensities of the P-line signal could be connected to interstitial oxygen.

Other DRL emissions in the spectral range of 0.7-1.0 eV have been identified and collectively been named as D-line and further categorised with their respective energy levels into D1-0.812 eV (with a shift towards 0.807eV), D2-0.875eV, D3-0.934eV and D4-1.000eV, and all of these have been connected as radiative defects at or around dislocations [25]. The emissions has been separated into pairs, D1 together with D2, and D3 together with D4, as each appear under similar circumstances. The origin of D-lines is well investigated and D1 and D2 have been connected to electronic transitions at the dislocation kinks or jogs (dislocations are not straight lines) [26], and further connected to impurities or point defects trapped in the strain field around the dislocation. D3 and D4 have been reported to be a result of the electronic transitions within the dislocation cores [26]. The D lines have generally been reported to appear after high temperature anneals, as shown in multiple works done by S.Pizzini [27, 4]. the D-lines first appear after anneals at around 650°C and above. In one study it was used CZ-silicon

samples that were induced with dislocations or thermally annealed [27]. And the D1 line did appear as a sharp peak in the samples with dislocations, but it also appeared as a broad luminescence band in one of the p-type sample that was absent of dislocation. This sample had only been exposed to an anneal for nucleation and precipitation of oxygen.

4 EXPERIMENTAL

4.1 SAMPLE PROPERTIES AND PROCESSING

The goal for this study was to perform a comparative study of DRL in n-type CZ silicon wafers in the temperature range of thermal donors. The objective has been to of connect relevant DRL to thermal donors and to identify how these were distributed in the wafer, where thermal annealing was a part of the method in generating and eliminating thermal donors in the material.

To achieve this, samples expected to have both high and low content of TDs was used and processed. This was done by using samples from both the seed and tail end part of the ingot, as the seed end is exposed to temperatures known to generate TDs for a prolong time, and the opposite applies for the tail end part. Furthermore, the seed samples had high concentrations of interstitial oxygen versus low concentrations of interstitial oxygen in the tail end. Some variation in concentration of substitutional carbon was also present in the samples.

The samples were kept as cut, as possible passivation layer could be affected of annealing process and partly dissolve. In addition, from a commercial aspect investigating as cut samples is relevant so no etching was done

The heating process was performed at two different temperatures, one for generating thermal donors and the other with the purpose of eliminating thermal donors in the wafers. The time intervals for the annealing was performed stepwise with the longest consecutive annealing at 100h.

4.1.1 Sample properties

The samples used in the study were supplied from Norsun and came from commercially produced Czochralski silicon ingots. The samples were taken from the upper and bottom most part of ingot. The wafers were expected to be low in extended defects, such as dislocations and metallic impurities. The samples were received as cut and were kept as cut under the study.

First set of samples originated from the same ingot and were neighbour wafers selected from the seed and tail end. The second set of samples had also been selected from the seed and tail end in the same manner but originated from two different ingots. In other words, the study involved in total 4 sample sets from 3 different ingots. The neighbouring wafers could not be expected to be identical in terms of the defect distribution.

The sample sets were given a name and within the sample sets each sample was given a name that starts with the sample set notation and end with a number that indicate the placement the wafer had with respect to the other wafers in the set. Table 4.1 gives an overview of the sample sets and the name of the samples within each sample set. In the same table the concentrations of interstitial oxygen, substitutional

carbon and resistivity are listed for each sample set. So, the respective sample sets was; S1, S2, T1 and T2 where S1 and T1 came from the same ingot.

SAMPLE SET	SAMPLE	Oi [ppma]	Cs [ppma]	RESISTIVITY[Ω]	Ingot
S1	S1-1	17.67	0.00	11.8	1
	S1-2				
S2	S2-1	17.23	0.07	11.8	2
	S2-2				
	S2-3				
	S2-4				
	S2-5				
T1	T1-1	12.44	0.06	9.37	1
	T1-2				
T2	T2-1	8.37	2.68	2.2	4
	T2-2				
	T2-3				
	T2-4				
	T2-5				

Table 4.1: Overview of samples with their respective oxygen and carbon concentrations, resistivity and which samples that came from the same set and ingot.

The table lists the sample specifications of interstitial oxygen, substitutional carbon and resistivity and applies for all the samples in each sample set. The seed end sample sets had relatively similar concentrations of O_i and C_s, meanwhile the tail end sample set differed in both O_i and C_s concentrations.

4.1.2 Thermal annealing processes

The thermal annealing was performed with two separate methods where the condition and annealing steps varied between the two methods. This was done by using two different furnaces and by doing one annealing in ambient air and the other in the presence of inert air and had the purpose of ruling out contaminations that can occur under the annealing. The sample sets S1 and T1 was annealed under the same conditions in inert air, while S2 and T2 shared the same annealing process in ambient air. This section will give a stepwise explanation of the respective annealing processes that was performed.

Set up of thermal annealing process for the S1 and T1 sample sets

The thermal annealing of S1 and T1 sample sets was performed at NMBU in a Nabertherm N 11/H muffle furnace. The furnace had a three-side heating with two on the wall sides and one at the bottom. The bottom heating was protected by conducting SiC tiles, and the furnace had a temperature uniformity up to +/- 10°C. The samples were placed in a protective annealing box from Nabertherm, which was

made out of heat resistant alloy 314 (AISI)/(DIN material no. 1.4841), essentially stainless steel. The annealing box had a piping for gas inlet and outlet. Extra pieces of CZ-Si wafers were placed at the bottom of the box and between the sample sets to protect them from contamination. All the anneals of S1 and T1 was performed in ambient air.

Stepwise description of thermal annealing process for the S1 and T1 sample sets

The S1 and T1 wafers were annealed over multiple steps, meaning that the samples experienced multiple heating and cooling processes. Figure 4.1 shows the annealing process for the S1-1 and T1-1 wafers, and these wafers only experienced anneals of 450°C.

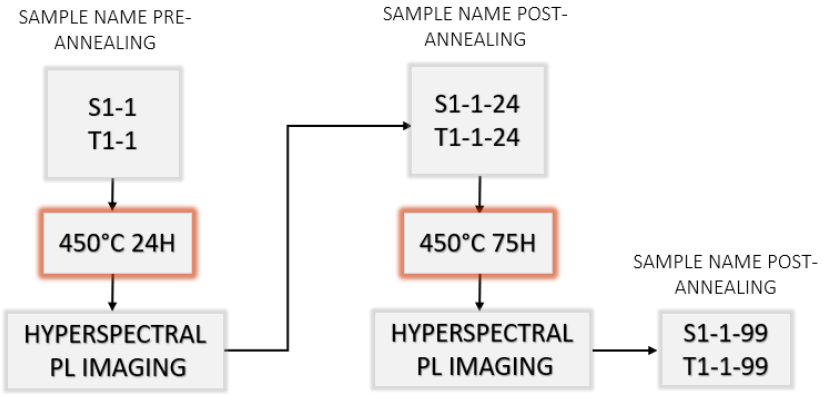

Figure 4.1: A stepwise description of the heat treatment of the S1-1 and T1-1 wafers.

The first annealing step was performed on S1-1 and T1-1 at 450°C for 24 hours, followed by a slow cooling inside the annealing box. After this hyperspectral PL imaging was performed on the samples. The samples were renamed after each annealing step to mark where in the process the hyperspectral imaging was performed. Here the samples have been renamed as S1-1-24 and T1-1-24 and will be denoted under this sample name for the whole thesis. The second annealing step was then performed on S1-1-24 and T1-1-24 and this was performed at 450°C for an additional 75 hours, resulting in a total annealing time of 99 hours. These samples went through a slow cooling inside the box and then again hyperspectral PL imaging was performed. These samples will be denoted as S1-1-99 and T1-1-99.

The thermal annealing of S1-2 and T1-2 followed the same steps as presented in Figure 4.1, but had an additional annealing step after the 99-hour annealing. This was a short time anneal for 1 hour at 650°C. Figure 4.2 shows all the anneals performed on S1-2 and T1-2.

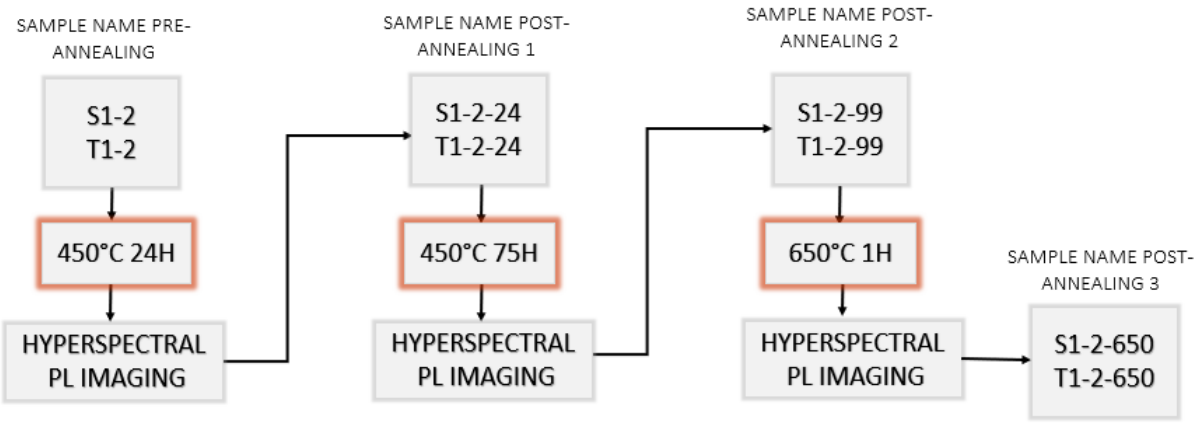

Figure 4.2: Stepwise description of the thermal annealing process of the S1-2 and T1-2 wafer.

The first annealing step was performed on the as cut samples S1-2 and T1-2 at 450°C for 24 hours, followed by a slow cooling inside the steel box. After this hyperspectral PL imaging was performed on the samples, and they were named S1-2-24 and T1-2-24. A second annealing step was then performed on S1-2-24 and T1-2-24 and this was performed at 450°C for an additional 75 hours. The samples were exposed to a slow cooling inside the box and then again hyperspectral PL imaging was performed. These samples were named as S1-2-99 and T1-2-99. A final heating step was then performed, and this was done on the S1-2-99 and T1-2-99 samples. They went through a short time annealing at 650°C for 1h, followed by room temperature cooling outside the protective annealing box. These samples were named S1-1-650 and S1-2-650.

Set up of thermal annealing process for the S2 and T2 sample sets

The thermal annealing of S2 and T2 samples sets were performed at IFE in a tube furnace produced by Tempress. The surfaces around the furnace were made from quartz and a N_2 flushing was used to reduce oxidation. The wafers were placed on a quartz stand and had no physical contact with any other surface under the annealing process.

Stepwise description of thermal annealing process for the S2 and T2 sample sets

In this annealing process a clean were performed prior to the annealing, both a HF dip and Piranha cleanse. Only the samples exposed to the short time annealing at 650°C was heated and cooled two times. Figure 4.3 shows all the annealing steps of the S2-2, S2-3, S2-4, S2-5, T2-2, T2-3, T2-4 and T2-5 wafers.

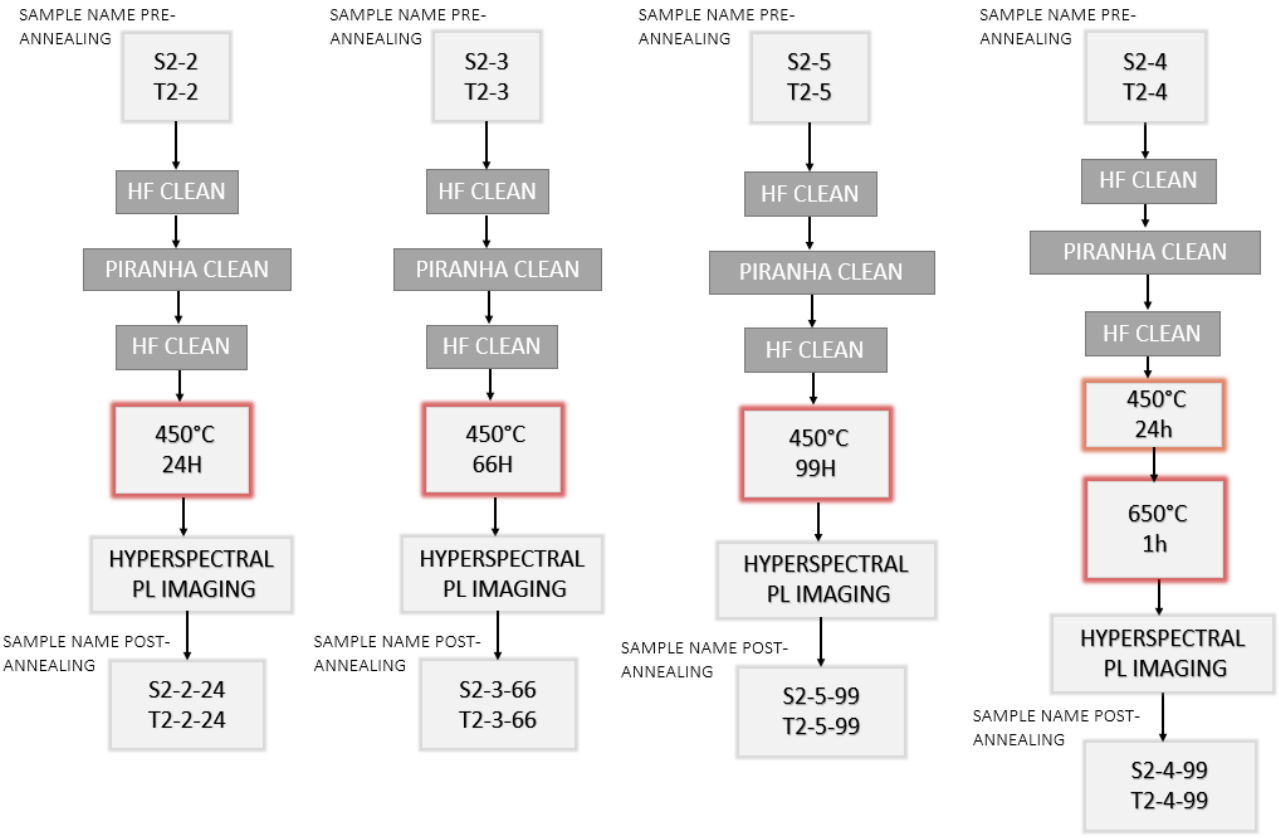

Figure 4.3: A full overview of the annealing steps of the S2-2, S2-3, S2-4, S2-5, T2-2, T2-3, T2-4 and T2-5 sample and their new names after heating: S2-2-24, S2-3-66, S2-4-650, S2-5-99, T2-2-24, T2-3-66, T2-4-650 and T2-5-99 .

The cleaning process was the same for all the wafers, and between each cleaning the samples was dipped in distilled water (hereafter DI) and dried in a N_2 well. Note that these steps are not shown in the chart above. The first clean was an HF dip for 2 minutes, before a dip in DI and then dried in N_2. After this an 8-minute deep clean was performed in a piranha solution, H_2SO_4:H_2, and after this a dip in DI and again dried in N_2. And lastly, again a cleanse with HF for 2 minutes before it was dipped in DI and dried

in N_2. After the cleaning process the annealing of the wafers was performed. S2-2 and T2-2 was exposed to one anneal at 450°C for 24 hours. Directly after the heating process the wafers was extracted out of the tube furnace and cooled in room temperatures. This will be referred to as a short time cooling in this thesis. In accordance to the first annealing process the S2-2 and T2-2 samples were named S2-2-24 and T2-2-24. Note that sample T2-2-24 broke under the cleaning process and only half a sample was used in the study. Next was the annealing of S2-3 and T2-3 which was performed at 450°C for 66 hours and before a short time cooling, and named as S2-3-66 and T2-3-66. The S2-4 and T2-4 were the only samples that experienced multiple anneals, first a 24-hour annealing at 450°C followed by a short time cooling in room temperature. And then a last annealing step at 650°C for 1 hour and then the same short time cooling. These wafers were named S2-4-650 and T2-4-650. Samples S2-5 and T2-5 were exposed to the longest annealing time of 99 hours at 450°C and experienced the same short time cooling before being named S2-5-99 and T2-5-99.

Table 4.2 give an overview of all the sample names after all the various annealing steps, and the samples will be referred to with these names for the remainder of this thesis. The table also show the progress of the sample names to clarify and avoid confusion throughout the rest of this thesis.

SAMPLE SET	PRE ANNEALING SAMPLE NAME	POST ANNEALING SAMPLE NAME
S1	S1-1	S1-1-24, S1-1-99
	S1-2	S1-2-24, S1-2-99, S1-2-650
S2	S2-1	KEPT AS CUT
	S2-2	S2-2-24
	S2-3	S2-3-66
	S2-4	S2-4-650
	S2-5	S2-5-99
T1	T1-1	T1-1-24, T1-1-99
	T1-2	T1-2-24, T1-2-99, T1-2-650
T2	T2-1	KEPT AS CUT
	T2-2	T2-2-24
	T2-3	T2-3-66
	T2-4	T2-4-650
	T2-5	T2-5-99

Table 4.2: A full overview of all sample names after the various annealing steps.

Deviation between the samples as an effect of thermal annealing method

As the samples experienced different annealing methods this could cause some deviation between the sample properties post annealing. Firstly, the contamination risk will differ between the furnaces. The tube furnace used at IFE is expected to have had a cleaner and more controlled environment compared to the oven used at NMBU. The protective box used in the muffle oven was made from stainless steel and could be a possible source of contamination for the wafers in the S1 and T1 sample sets. The quartz stand used in the tube furnace for the heat treatment of S2 and T2 sample set is not expected to have had introduced any new impurities into the samples but oxygen might have been existing at the contact surface.

Secondly, S1 and T1 samples were annealed in ambient air and this could have caused increased oxidation at the surface, although this is expected to be limited in the long time anneals at 450°C because of the low temperatures. The S2 and T2 sample sets was annealed in the presence of N_2.

Thirdly, the S1 and T1 wafers were not exposed to a clean prior to the heating process and dirt at the surface from the production process could act as a contamination source. The cleaning also created an etching effect on the wafers and this could reduce some of the roughness at the surface. Some of the wafers attached to each other under the cleaning process, so the etching effect could appear uneven.

Even though there was to some extent contamination sources present during the annealing of S1 and T1 sample sets it is expected that the low temperatures of 450°C should lower the contamination risk. The 650°C annealing are at greater risks and here contamination must be considered to a greater extent when analysing the results.

A temperature profile of the S2 and T2 annealing could be presented and this would show a small deviation in temperatures. However, the temperatures under annealing of S1 and T1 was not monitored and possible deviation could have taken place. As the specification of the muffle oven reported of a temperature uniformity of +/-10°C the deviations are expected to be within this range.

The samples with the slow cooling were in the temperature range of TD slightly longer. It is not known how long but it should be considered insignificant compared to the long annealing time.

4.2 HYPERSPECTRAL PHOTOLUMINESCENCE IMAGING

The use of Photoluminescence (PL) imaging has been widely used for characterization of solar cell material. PL imaging is based on capturing the photoluminescence that gets emitted when recombination of an electron and a hole occur. Standard PL imaging methods used on CZ-silicon material is limited to mapping the band to band recombination and is lacks the spectral resolution [10]. However, hyperspectral photoluminescence imaging can extract both the spectral and spatial information. The hyperspectral camera can detect emissions in the infrared or near infrared wavelength region, and not only band to band (BB) luminescence. If an emission is detected at other wavelengths than at the BB wavelength it could possibly show that a defect is present within the bandgap, allowing an electron to recombine (section 2.3.3). The hyperspectral imaging system divide the radiation received from each pixel into many sections, i.e. narrow spectral bands, before detecting them. The camera scans one pixel line at a time and captures two-dimensional images (2D), one showing the spatial dimension of the sample and the other the spectral dimension corresponding to the wavelength, as shown in figure 4.4 a.) [8, 24]. By allowing the camera to move over the sample it scans multiple pixel lines and creates an additional spatial dimension in the y direction, creating what is known to as a hypercube (see figure 4.4 b.)). The data can be viewed as a batch of monochromatic images, where each corresponds to one spectral band. The y and x axis represent the two spatial dimensions and λ represent the spectral bands. In the setup used in this thesis the wavelengths will be presented with the energy of the emitted photon, which is in the units of electron volt (eV).

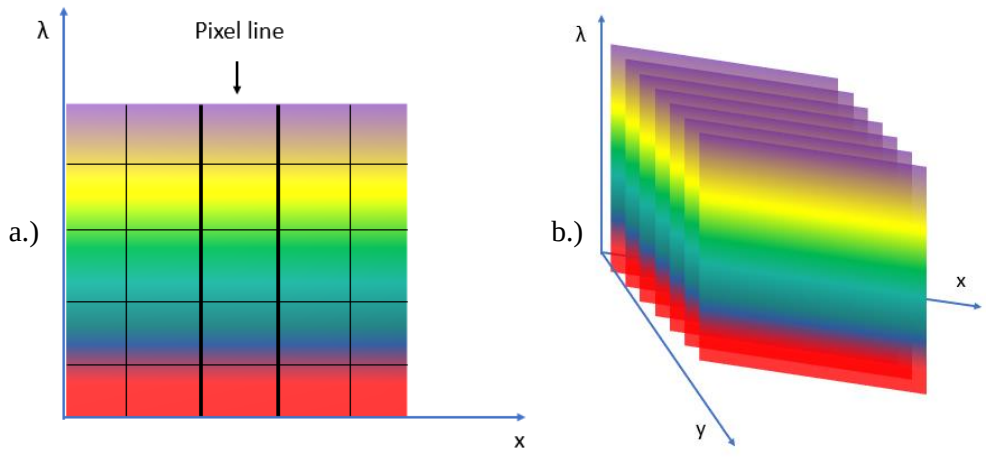

Figure 4.4: Spectral and spatial images (a.), creates a hypercube by moving the camera (b.)

4.2.1 The set up

The set up for hyperspectral imaging is dependent of many factors in order to get the best results of both spectral and spatial resolution. Figure 4.5 shows the setup used in this study and the components are marked from 1-5. The camera (1) is attached to a movable rig (2) and it is the movement of the rig that creates the additional spatial dimension in the y direction. A line laser (3) is mounted to the same rig and illuminate the wafer simultaneously as the camera operates. The excitation source needs to be adjusted for an even distribution in injection level across the sample. The wafers are placed (5) on top of a cryogenic cooler (4) under the hyperspectral PL imaging.

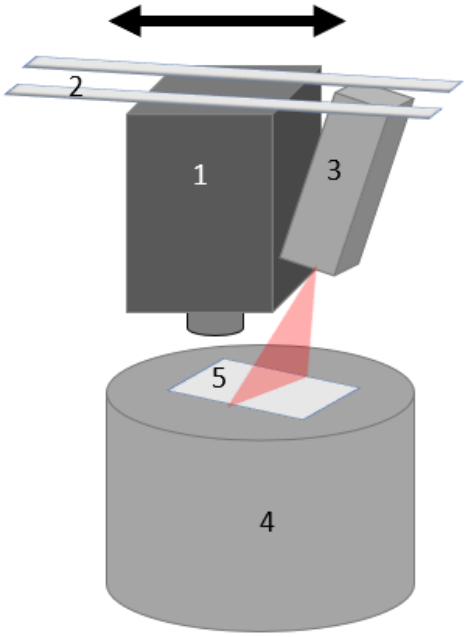

Figure 4.5: The setup. 1) Hyperspectral camera, 2) movable rig to scan the wafer to create the second spatial dimension in the hypercube, 3) excitation source, line laser with a wavelength of 808nm, 4) cryogenic cooler that is filled with liquid nitrogen and 5) the placement for wafers on top of the cryogenic cooler .

Hyperspectral camera

The hyperspectral camera is marked as 1 Figure 4.5 and is a NIR Pushbroom camera of the brand SWIR (Specim, Spectral Imaging, Ltd, Oulu Finland.), with a HgCdTe detector with a spectral sensitivity in the 929-2531 nm, equivalent to 0.49-1.33 eV. In this study the camera was set to record 25 pictures per second with an exposing time of 20.0 ms. The scanning speed of the camera is dependent of the distance from the sample and will vary between 10.26-12.45 mm/s depending of the sample set. All the images were photographed with the same resolution of 510 µm.

In addition, the camera was equipped with an 850 nm long pass filter. As the laser wavelength was 808nm and therefore caused a second-order wave refraction at 1616nm, this was within the detection range of the camera. The long pass filter shuts out wavelengths shorter than 1000nm.

Laser

The excitation source is an 808nm line laser from Coherent (Lasiris Magnum II, Gamatada Instrument AB, Uppsala, Sweden). It has a maximum beam power of 5600mW and can be regulated manually by adjusting the bias voltage between 0.5-5.0 V with a potentiometer. In this study a bias voltage of 5.0 V was used.

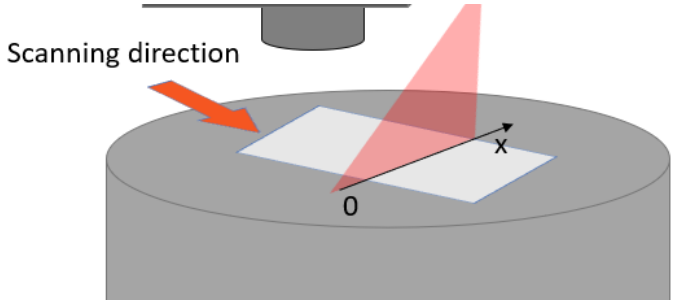

Figure 4.6: show how the laser illuminates the sample as the camera scans and photograph the wafer. Due to uneven laser intensity the sample is place closer to the x direction, as the laser evens with its length [28].

The laser beam does not provide a completely even illuminated line, as the spatial distribution of the laser has been shown to be stronger close to the edge marked as 0 in Figure 4.6. The intensity of laser line is more evenly distributed further in, toward the x direction. The intensity peak seen at the edge was therefore adjusted to not illuminate the sample when scanning over. For further information on the distribution of laser intensity the reader is encourage to read paper listed as reference [28].

The penetration depth of the laser is dependent of the wavelength and the material, but the average penetration depth in the CZ-silicon wafers was expected to be approximately 12.5 µm.

The hyperspectral PL imaging was performed under the same settings and conditions for each sample in the sample set. The hyperspectral PL imaging of the S1 and T1 sample set had a laser intensity of around 2 W/cm^2, and S2 and T2 had a laser intensity of 1.8 W/cm^2. Note that, possible deviation in laser intensity can occur if the laser line hits the samples in an askew angle.

Cryogenic cooler

A cryogenic cooler was used to freeze out phonons as this enhances the defect related luminescence. The cryogenic cooler was made from aluminium and covered with Styrofoam isolation to maintain sufficiently low temperatures. On top of the cooler there was an uninsulated area with an aluminium plate for the placement of the wafers. A thermometer (TE-NME 72-7712-T-type) was connected to the cooler top to monitor the temperature at the surface. In this study liquid nitrogen was used as a cooling medium and the hyperspectral PL imaging was performed at temperatures at around 85-90K.

4.2.2 Mean spectrum and spatially resolved images

After obtaining the data hypercube from the hyperspectral PL imaging the spectral response in each pixel needs to be extracted. This is done by taking the mean pixel value of the wavelength bands in the x-y plane in the hypercube, and putting this together as a total mean spectrum of the entire hypercube. An example of such a plot can be seen in Figure 4.7 a.) where the wavelengths has been recalculated into units of electron volts that represent the photon energy. The spatially resolved images are created by integrating over the wavelengths (photon energies) of interest, as demonstrated in Figure 4.7 a.), where 1 and 2 are the chosen integration limits spanning over the spectral range of 0.667-0.767eV. Here the spectrally resolved image in Figure 4.7 b.) show how these signals are distributed in the wafer. The integration limits will be chosen based on the results found in the mean spectrum.

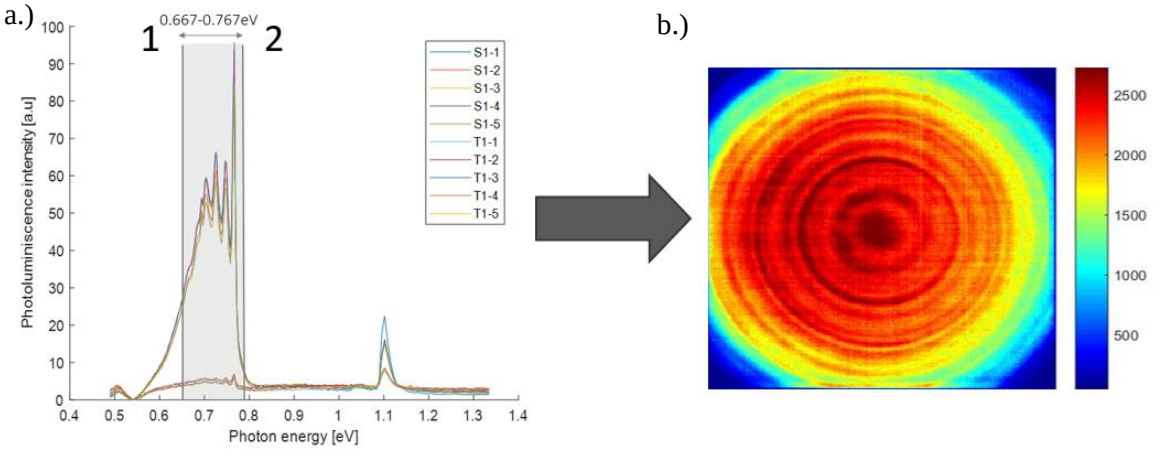

Figure 4.7: a.) show the total mean spectrum that is put together by taking the mean pixel value of the wavelength bands in the x-y plane in the hypercube, b.) show the spatially resolved image that are created by integrating over the photon energies(wavelengths) of 0.667-0.767eV.

4.2.3 Sample properties effect on luminescence spectra.

As cut samples that have not been exposed to any surface preparation can be expected to have a rugged surface from the sawing of the wafers. The variations in surface condition can therefore cause the optical properties to vary between the samples. Roughness in the surface can cause more scattering of the laser beam and lead to increased diffuse scattering. If the roughness in the surface is on a smaller scale than the wavelength of the laser, the surface will appear flat and there would be significantly less scattering. The irregularities from the sawing process is expected to be around 10 µm which is much larger than the wavelength of the laser (808nm). The S2 and T2 sample sets was exposed to a clean in a piranha solution, a mixture of sulfuric acid and hydrogen peroxide, and this will have an etching effect on the surface of the wafer and reduce some of the roughness.

In addition, as cut samples are strongly affected by surface recombination due to interruption of the periodicity of crystal lattice at the surface. This will further affect the spectral response of the BB signal and radiative defects.

The laser has a penetration depth of approximately 12.5 µm, while the total thickness of the wafer is 125 µm, meaning the luminescence in the spectral response will originate from a region close to the surface.

4.2.4 Multivariate Curve Resolution

The data retrieved from hyperspectral PL imaging consists of mixed emissions signals at their respective spectral bands. The signals can overlap and become mixed when they are close in energy and spatially present in the same regions. To assist in the separation of signals the Multivariate Curve Resolution (MCR) algorithm was used. MCR mathematically decompose the data in the hypercube created from the hyperspectral PL imaging into different components and concentrations of the components [29, 28]. The method uses the bi-linear model where:

$$D = CS^T + E \tag{4.1}$$

This is a version of alternating least squares (ALS), where D ($r \times c$) is the matrix of data in the hypercube, and that gets decomposed into two smaller matrixes C ($r \times n$) and S^T ($n \times c$). C contains the concentration profiles and S^T contains the correspondent spectra for the components [29]. r and c represent the number of rows and columns of the original data matrix D and n is the number of components. The number of components that is chosen will therefor put constrains on the dimensions of the C and S^T matrices. The number of components of D is the first step in the operating procedure of the MRC-ALS and is chosen manually, and the number used in this study varied between 3 to 7 components. By choosing to many a "forced" separation of signals can occur, and this appear as a vertical wave pattern in the MCR images. If choosing too few components the MCR algorithm can fail to separate signals. In this work the suitable number of components was chosen by testing.

5 RESULTS AND DISCUSSION

5.1 HYPERSPECTRAL PL IMAGING

Hyperspectral PL imaging was used as a method to investigate if thermal donors could be detected as a part of the DRL in thermally annealed CZ silicon. As hyperspectral PL imaging obtain both spectral and spatial resolution, a big part of the results will be based on these findings and further followed by a discussion.

5.1.1 Spectral response as cut wafers

Spectral imaging was performed on all the as cut samples in the temperature range of 85-90K under a laser intensity of 1.8 W/cm^2 and 2.0W/cm^2. Figure 5.1 shows the mean spectra of sample sets a.) S1 and T1 and b.) S2 and T2. Multiple emission lines can be observed within the spectral range of 0.667-0.767 eV. The peaks are located at 0.767ev, 0.746eV, 0.724eV, 0.703eV and with a shoulder at 0.667eV. The DRL is present in all sample sets except the T1 set.

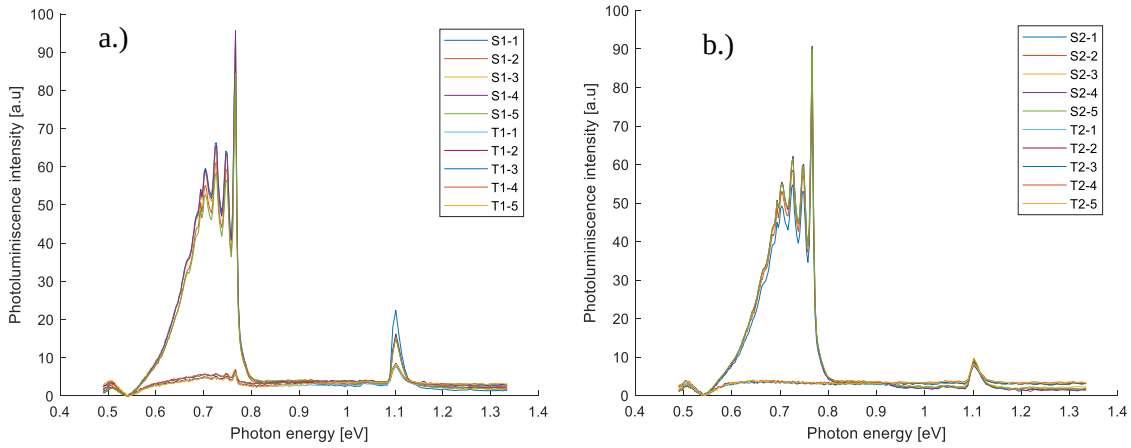

Figure 5.1: Mean spectra of all the wafers in a.) S1 and T1 set and b.) S2 and T2 set. These are as-cut wafers and have not been exposed to any heat treatment.

The emission lines found in the as cut samples have been marked from 1-6 in Figure 5.2, where 1-5 are DRL emissions. The emission lines are listed with assigned names, D069 at 0.698, D070 at 0.703 eV, D072 at 0.724 eV and D074 at 0.746 eV. The signal at 0.767 eV has been denoted as the P-line in other experimental work [23].

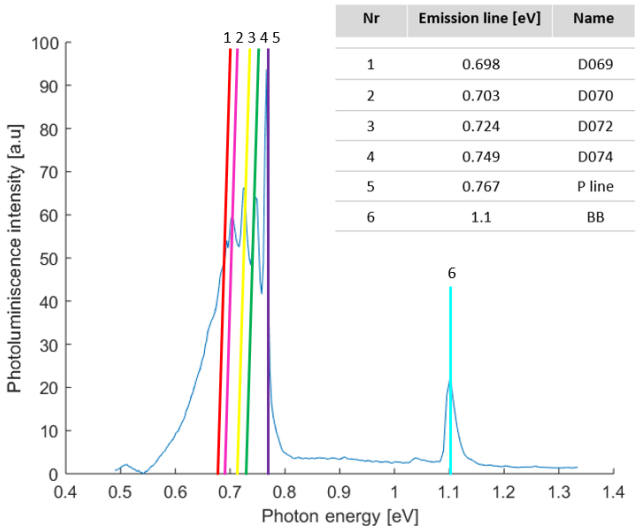

Nr	Emission line [eV]	Name
1	0.698	D069
2	0.703	D070
3	0.724	D072
4	0.749	D074
5	0.767	P line
6	1.1	BB

Figure 5.2: The emission lines that was detected in the as-cut sample set S1, S2 and T2 have been marked and listed with emission energy and name.

Differences in mean spectra - Setup differences

The spectral imaging was not performed under identical conditions for all the sample sets. S1 and T1 set was photographed with a laser intensity of 2.0 W/cm^{2,}, while S2 and T2 was photographed with a laser intensity of 1.8 W/cm^2. As the samples in S1 and T1 were put through several heat treatments it was not possible to retake the images with the same laser setting. However, one as cut sample was kept from each set, and these were photographed with the same laser settings. Figure 5.3 shows the mean spectra of S1-1 and S2-1 under a laser intensity of approximately 1.8 W/cm^2. When comparing the spectral response of these samples some differences can be seen in the intensity of the DRL emission. This could indicate that there are natural differences in the defect distribution between the two sets.

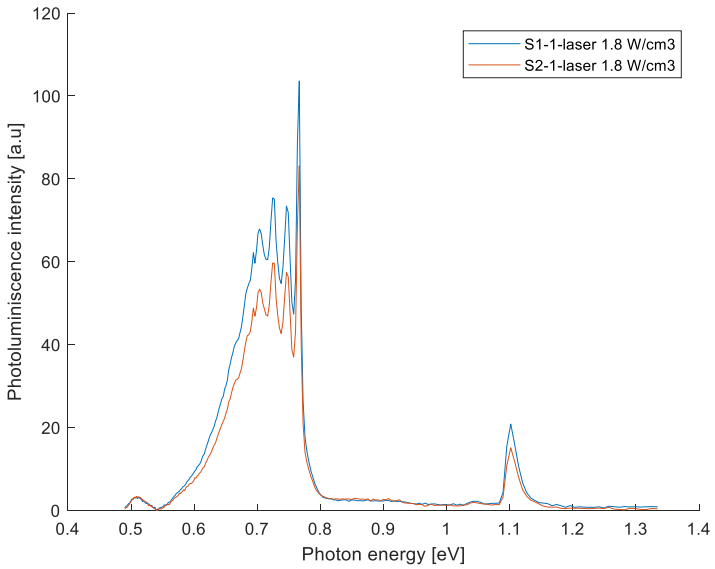

Figure 5.3: The mean spectra of S1-1 and S2-1 under a laser intensity of approximately 1.8 W/cm^2. The small differences in intensity could indicate natural differences in the presence of the defect.

5.1.2 Spatial distribution of defect related luminescence - spectral range 0.667-0.767eV

This section will present the spatial distribution of the DRL in the spectral range of 0.667-0.767eV. Figure 5.4 highlights which part of the spectra this will cover, and lists the samples presented in the section.

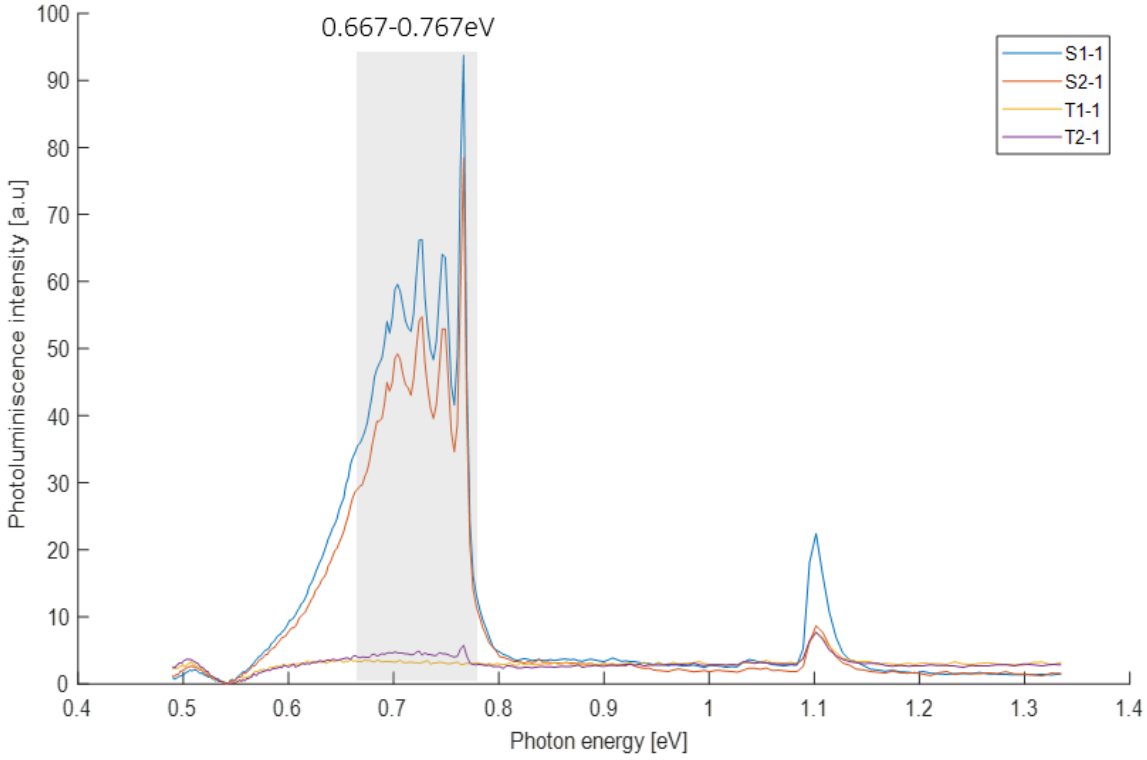

Figure 5.4: The covered spectra in this section is highlighted in the graph, and the relevant samples are listed.

Figure 5.5 shows the spatial distribution of the DRL signals in a.) S1-1, b.) S2-1 and c.) T1-1. All the samples in S1, S2 and T1 show a high degree of similarity in the distribution of the signal, so only a couple of examples from each sample set have been extracted and presented in figure 5.5. The images were created by integrating the luminescence signal over all the wavelength between 0.667-0.767 eV. The general characteristic of the spatial distribution of the signal is that it accumulates in a ring-like pattern and radially increase toward the centre of the wafer. The signal is absent at the edges of the wafers and hardly present in the tail end sample T1 shown in c.).

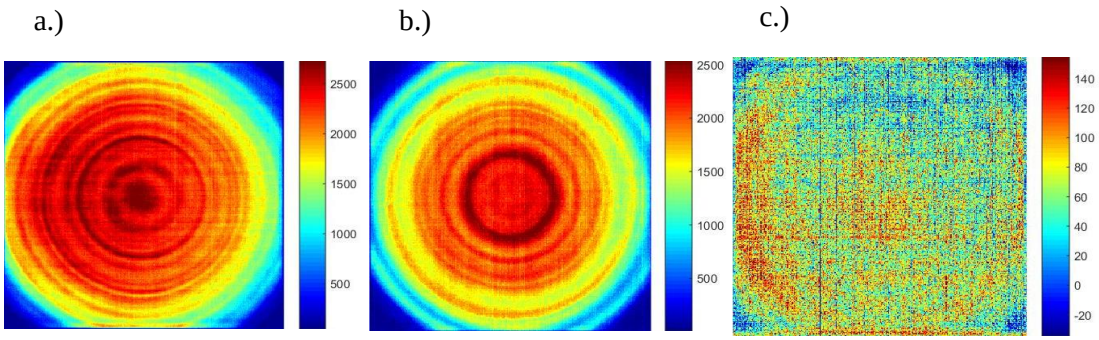

Figure 5.5: Spatial distribution of the DRL signals in the spectral range 0.667-0.767eV for sample a.) S1-1, b.) S2-2, c.) T1-1.

5.1.3 Section discussion

The samples within the same set show a high degree of similarity in the spectral and spatial distribution of the DRL signals. When comparing the concentrations of interstitial oxygen (Figure 4.1) with the intensity of the DRL signals a pattern can be seen. The intensity of the DRL emissions are clearly higher in the oxygen rich seed end samples. As mentioned in section 3 the emission at 0.767 has been denoted as the P-line in earlier studies [23] and has been connected to thermal donors as it first appeared in thermally annealed samples with high oxygen content. The seed end part of the ingot is generally considered to contain high concentrations of thermal donors (section 2.5.3).

The sharp peaks at D069, D070, D072 and D074 have only been described in earlier work done By Mehl [24]. There it was concluded that the emission lines (and the P-line) were due to thermal donors and that the defect was spatially distributed in a ring like pattern. This further indicates that the DRL emissions seen in the as cut samples in figure 5.4 could be due to thermal donors.

In addition to the DRL signals, the BB signal can be observed in the spectra at 1.1 eV. The intensity of the BB signal is very low, which can be expected in as cut samples, as this is an effect of a high level of surface recombination and increased scattering of the laser. However, when comparing the relationship between the DRL signal and the BB signal, peaks connected to DRL appear at much higher intensities. The emissions seen in the spectral range of 0.667-0.767eV will be due to recombination at traps placed near mid gap, and are therefore considered as deep level traps (section 2.3.3). These are known to be effective recombination centres, and can possibly explain the high DRL signals. Further, the recombination rate is directly proportional to the number of empty traps and the concentration of electrons in the conduction band. The defect responsible for the DRL at the P-line must therefore be present in high densities to cause the high peaks seen in the mean spectra.

5.2 SPECTRAL RESPONSE OF THERMALLY ANNEALED SEED END WAFER

Figure 5.6 shows the spectral responses from each annealing step of the samples in the S1 set. From observing the spectra it is evident that the DRL is affected by heat treatment. The peaks between 0.669-0.767 eV show a strong increase in height and is almost identical in both S1-1-24 and S1-2-24. The relationship between the peaks has not changed and the peak at the P-line (0.767eV) is still the most prominent. The annealing process also introduced several new emission lines into to the mean spectra, at 0.807eV, 0.904eV and 0.925eV. Two of the signals have been named in existing literature, where the signal at 0.807 is referred to as the D1 signal and the signal at 0.925 is referred to as the H-line, see section 3.

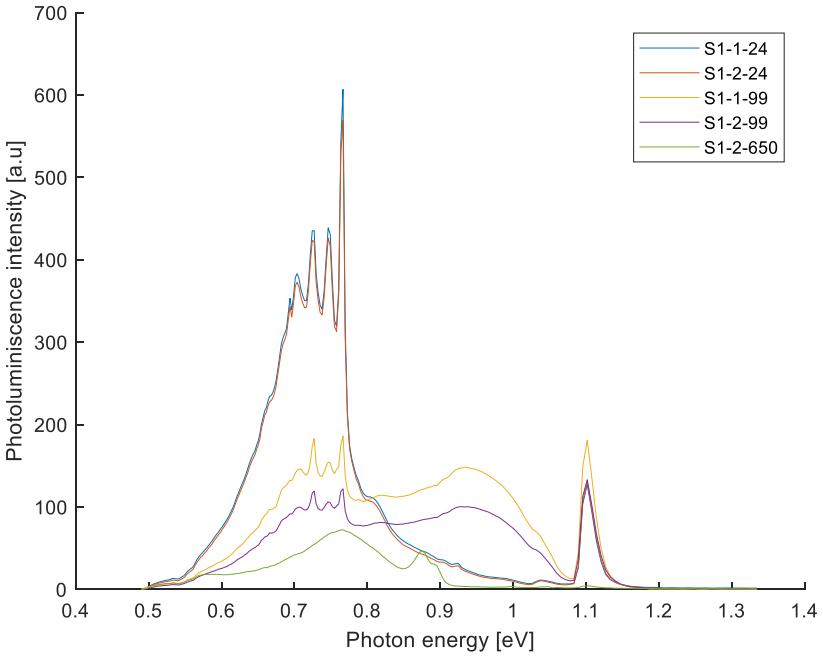

Figure 5.6: S comparison of the spectral responses from each heat treatment step of the samples in the S1 set. Multiple new emission lines are formed in the energy range of 0.807-1.001eV at temperatures of 450°C, and at temperatures of 650°C many of the same emission lines is eliminated from the spectra.

Figure 5.6 also presents the mean spectra for the second heat treatment of 99 hour at 450°C of wafers S1-1-99 and S1-2-99. When comparing this to the mean spectra of wafers S1-1-99 and S1-2-24 an obvious change can be seen in the DRL signals. The height of the peaks between 0.66-0.767 eV have been reduced significantly, and the relationship between some of the peaks has changed. The D072 signal is now almost at the same intensity as the P-line. Also, a wide emission band has formed between the 0.904 eV and 1.001 eV with a peak at 0.9251 eV.

When comparing all the heat treatments at 450°C an unexpected growth of the BB luminescence can be spotted. Before the thermal process the intensity of the BB signal was considerably smaller than the

DRL signals in the sample. After the last annealing step the height of the BB signal exceeds any other emission signals in the sample.

At 650°C the mean spectra of samples S1-1-650 and S1-2-650 show a complete redistribution of the DRL. This eliminated the peaks at D069, D070, D072, D74, D1, D090 and the H-line. Instead a wide emission band has formed between 0.66-0.85 eV with a peak at the P-line. Besides this, a new emission line is present at 0.87 eV and is know from literature as the D2 defect. Here the BB intensity goes back to as cut values.

The mean spectra of the thermally annealed samples from S2 set can be seen in Figure 5.7. The samples in the S2 set was heated and cooled once. The exception is the S2-4-650 sample that had a two-step annealing, and section 4.1.2 give a detail description of the thermal processes.

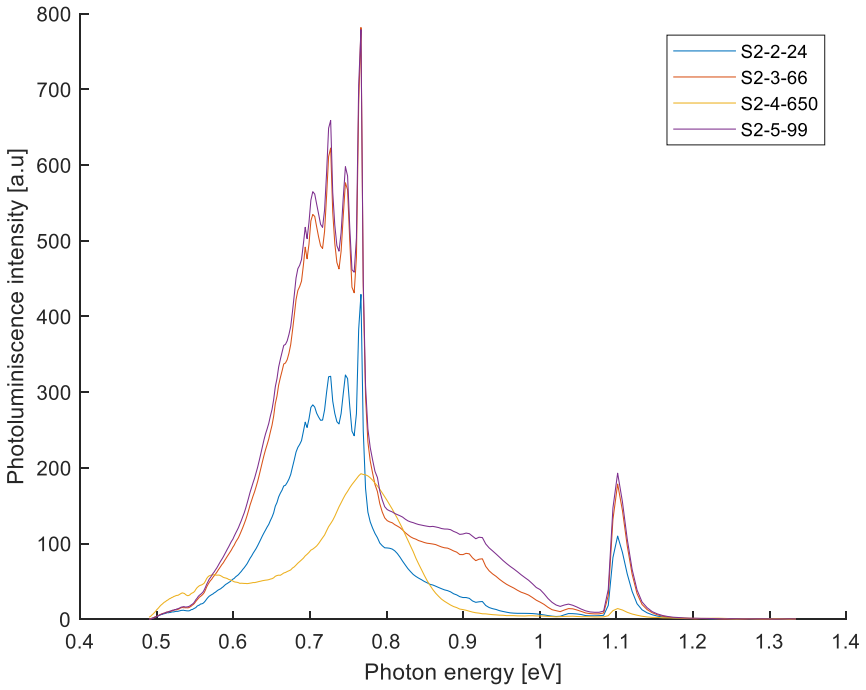

Figure 5.7: Comparison of the mean spectra from each heat treatment step of the samples in the S1 set. Multiple new emission lines formed in the energy range of 0.807-1.001eV at temperatures of 450°C, and at temperatures of 650°C many of the same emission lines is eliminated from the spectra.

The mean spectra from S2-2-24 fits well with the results of the S1 samples after 24 hours (Figure 5.6). Both show a clear growth of the peaks between 0.70-0.767 eV, and new emission lines are present at D1, 0.90 and the H-line. The growth of the DRL signals continue up to somewhere between 66-99 hours of annealing, as it is evident that the height of the peaks are almost identical in S2-3-66 and S2-5-99. Only small changes can be seen in the growth of the intensity between the D090 and the H-line signals.

In line with the first sample set the BB luminescence was affected by the annealing and have increased. However, the intensity of the BB signal never exceeded the intensities of observed emission lines between 0.70-0.767 eV.

The results of the short time annealing of S2-4 at 650°C fits with the findings from the S1 sample set. There is one wide emission band with the P-line as a local peak, and the BB signal have been reduced to intensities that was seen in the as cut samples, prior to any of the process steps.

Table 5.1 gives a summary of the DRL signals identified in the seed end sample sets, S1 and S2, after the performed annealing processes. Additional information has been specified under notes.

SAMPLE	P LINE	H LINE	D1	D074	D072	D070	D069	D090	NOTES
S1-1-24h	✓		✓	✓	✓	✓	✓		
S1-2-24h	✓		✓	✓	✓	✓	✓		
S1-1-99h	✓	✓	✓	✓	✓	✓	✓	✓	Broad band 0.89-1.01 eV
S1-2-99h	✓	✓	✓	✓	✓	✓	✓	✓	Broad band 0.89-1.01 eV
S1-2-650C	✓								Broad band with P line peak. D2 present. Shoulder at 0.89 eV
S2-2-24h	✓		✓						
S2-3-66h	✓	✓	✓	✓	✓	✓	✓	✓	
S2-4-650C	✓								Broad band with P line as peak
S2-5-99h	✓	✓	✓	✓	✓	✓	✓	✓	

Table 5.1: DRL signals identified in the seed end sample sets, S1 and S2, after the performed annealing processes.

5.2.1 MCR analysis of thermally annealed seed end wafers

The annealing processes resulted in large changes in the spectral response, and in some of the mean spectras wide emission bands could be observed. A MCR analysis was therefore performed to aid in the separation between signals. The MCR plots are presented in order of annealing time and only the MCR plots with reliable and relevant results will be shown in this section. Figure 5.8 shows the MCR plot for the S1-2-24 sample, with 5 components. MCR divided the new emission lines into different signals, with D1 as a sharp peak and one wide band with the H-line as another peak. The emission lines D07, D072, D074 and the P-line could not be divided into different signals.

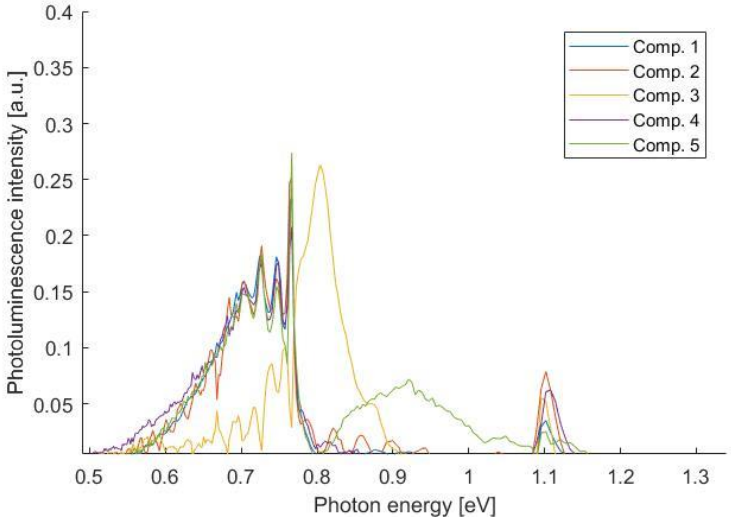

Figure 5.8: The MCR analysis of S1-2-24 with the loadings plots for each of the 5 components.

Figure 5.9 a.) and b.) shows the MCR plot for S2-3-66 where a total of 7 components was used. When comparing component 1 and component 2 in plot a.) it appears as if some separation has been done between the P-line and the other peaks, but it does not identify any of the peaks as its own component. Still, the H-line and D090 can observed as one wide emission band in component 3.

a.) b.)

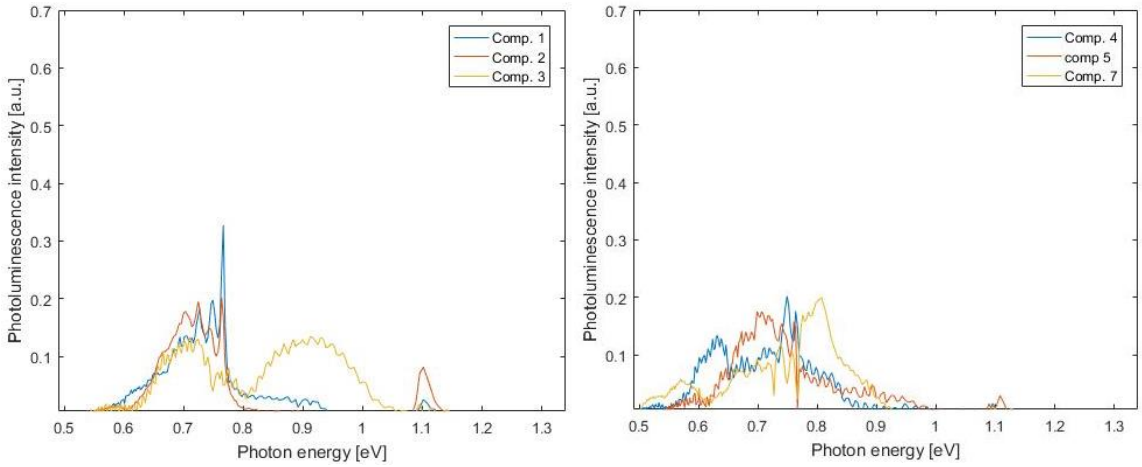

Figure 5.9: The MCR analysis of S2-3-66 with the loadings plots for components a.) 1-3 and b.) 4-7.

The MCR analysis for S1-2-99 is shown in Figure 5.10 and this analysis managed to divide the wide band between the energies of 0.80 and 1.001 eV into 3 components. The D1 signal can be seen in component 5 with a clear peak at 0.807. Components 1 and 4 are parts of the wide emission band and stretches over almost the whole spectral range. These components are most likely a superposition of emission lines.

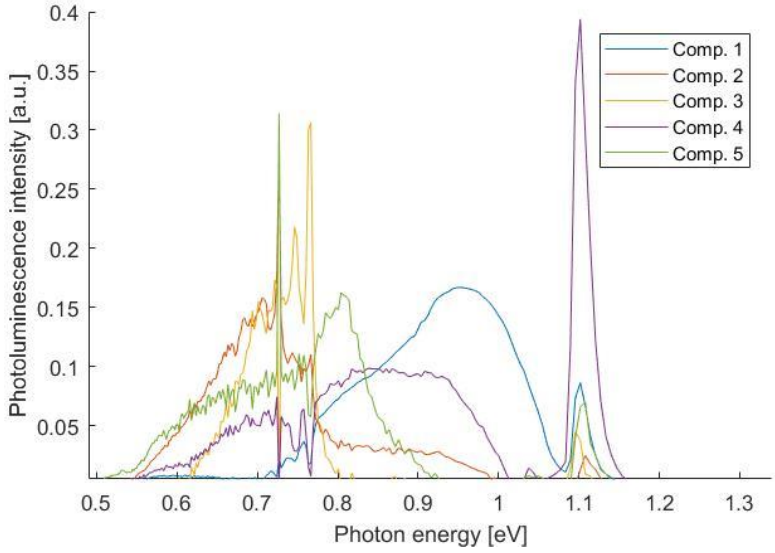

Figure 5.10: The loadings plots for components 1-5 of the MCR analysis for S1-2-99.

5.2.2 Spatial distribution of defect related luminescence - spectral range 0.667-0.767eV

This section will present the spatial distribution of the DRL in the spectral range of 0.667-0.767eV. Figure 5.11 shows which part of the mean spectra this will cover, and an overview of the samples presented.

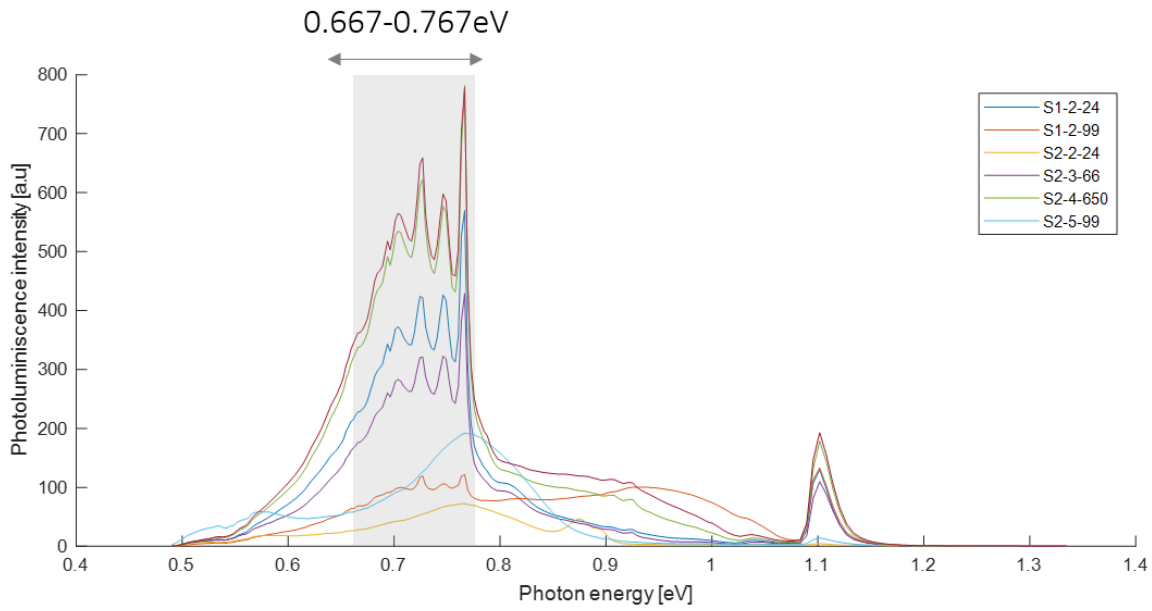

Figure 5.11 Covered spectra in this section is highlighted in the graph, and the plot shows the mean spectra of some selected samples from both S1 and S2 set.

Figure 5.12 shows the DRL distribution in a.) sample S1-2-24 and b.) sample S2-2-24. When comparing this to the as cut samples S1-1 and S2-1 in Figure 5.5, it is evident that the DRL signal has diffused into a larger region of the wafers. The spatially resolved images show that the signal is still distributed in a ring like pattern, and the DRL decreases radially towards the edges of the wafer.

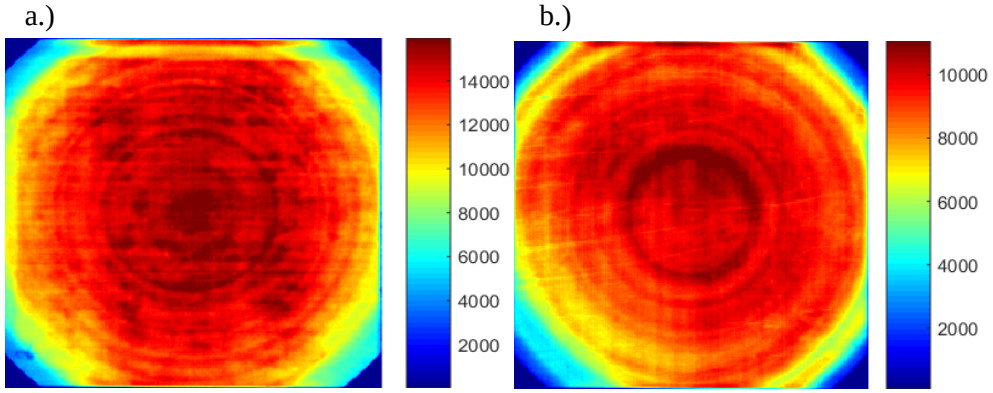

Figure 5.12: Distribution of the DRL signals in the range of 0.667-0.767eV in wafers a.) S1-2-24 and b.) S2-2-24. These samples were heat treated for 24 hours at 450°C.

Only sample set S2 was exposed to a singular annealing for 66 hours, and Figure 5.13 shows the spatial distribution of the signal in sample S2-3-66. This resulted in no significant changes in in the spatial distribution of the signal and the features are essentially the same, except that the ring pattern appear

less prominent. Also, the pattern that swipes across parts of the sample was caused by mist that circled over the wafers when the hyperspectral imaging was performed.

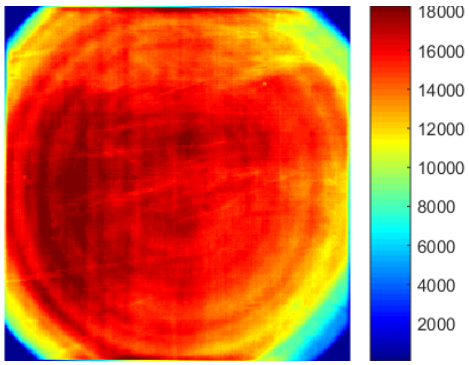

Figure 5.13: Distribution of the DRL signals in the range of 0.667-0.767eV in wafers S2-3-66. This sample was heat treated for 66 hours at 450°C.

Figure 5.14 shows the spatial distribution of a.) sample S1-2-99 and b.) sample S2-5-99. When comparing the mean spectra of the two samples remarkable differences can be seen in the DRL. The images in a.) and b.) are completely opposite of each other. In a.) one large ring formation can be seen close to the edges, meanwhile in b.) the DRL signal is almost uniformly distributed in the whole sample, except at the edges.

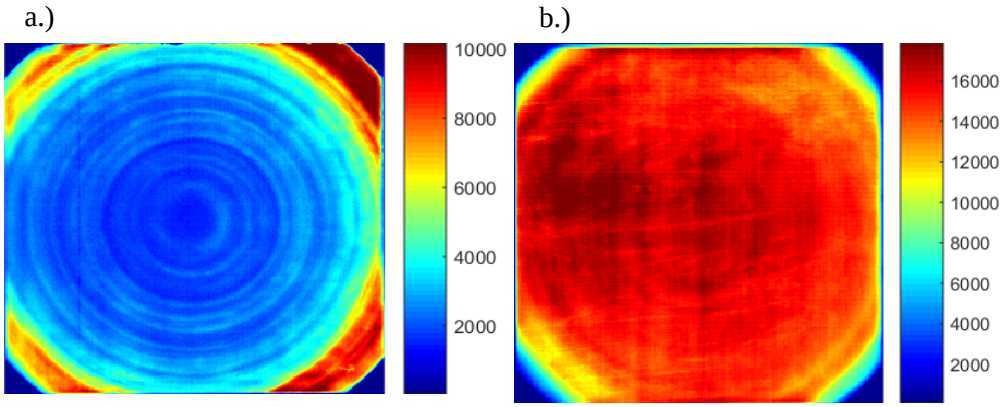

Figure 5.14: Spatial distribution of the DRL signals in the range of 0.667-0.767eV in wafers a.) S1-2-99 and b.) S2-5-99. These samples was heat treated for 99 hours at 450°C.

In addition to the 450°C anneals, a short time heating at 650°C was performed on both S1-2-650 and S2-4-650. This gave the mean spectra one wide emission band at 0.667-0.767, where a peak could be seen at the P-line energy, and all the other peaks between D069-D074 had disappeared. The spatial distribution of the DRL signal can be seen in Figure 5.15 for samples a.) S1-2-650 and b.) S2-4-650. These images of the signal are not identical in a.) and b.) but similarities can be seen. When comparing the two, both show a more uniform distribution of the DRL compared to the sample annealed at 450°C. The ring like pattern previously seen in the centre of the samples are reduced in a.) and not present in b.).

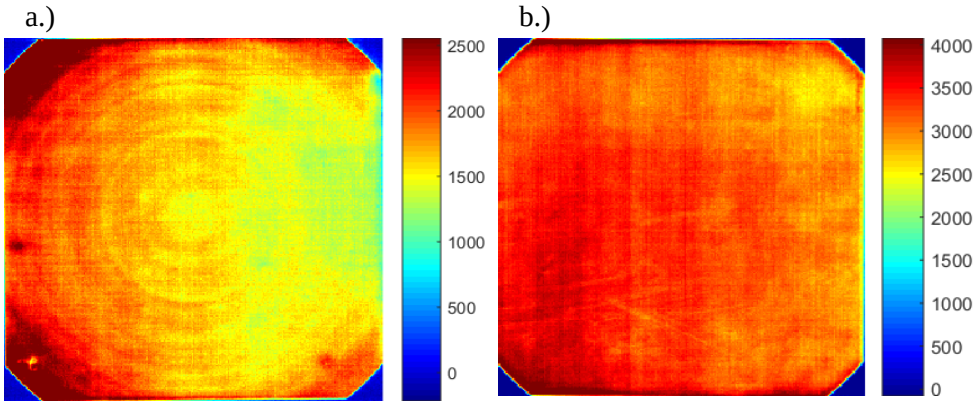

Figure 5.15: Distribution of the DRL signals in the range of 0.667-0.767eV in wafers a.) S1-2-650 and b.) S2-4-650. These samples were heat treated for 1 hour at 650°C

5.2.3 Section discussion of defect related luminescence - spectral range 0.667-0.767eV

Several emission lines are present in this spectral range, and an overview of the relevant peaks discussed in this section can be seen in Table 5.2.

Name	Peak
P line	0.767eV
D069	0.693eV
D070	0.702eV
D072	0.724eV
D074	0.746eV

Table 5.2: An overview of the peaks that can be observed in the spectral range of 0.667-0.767eV in Figure 5.11.

When comparing the spectral luminescence across the S1 and S2 sets it is evident that they share a lot of similarities in terms of DRL. Especially after the first heat treatment, performed at 450°C for 24 hours, the distribution of the DRL observed in the spectra and the images are remarkably similar (see

Figure 5.12 a.) and b.)). There are some small differences in intensity from the DRL in Figure 5.11, but when taking into account that the sample set was exposed to different annealing methods these are surprisingly small. After this a continuous growth of the peaks in the spectra could be observed with annealing time in sample S2-3-66 Figure 5.13. However, differences between the sample sets can be found in the results of the 99-hour heat treatment, as when comparing both the spectral and spatial distribution (see Figure 5.11 and 5.14) of the DRL, large differences can be observed. S1-2-99 shows a reduction in the intensity of the P-line while S2-5-99 shows no significant changes in intensity of the signal. Hence, it can be concluded that the development of the P-line results in both a decrease in intensity as in S1-2-99 and a standstill in S2-5-99. In section 3, Figure 3.1 was presented, showing the development of the P-line in the interval of 24-100 hours at annealing temperature of 450°C. These were taken from a study done by Mineav and Mudryi [23] which showed that the P-line decreased in this time interval while the other emission bands grew. No conclusions on why this occurred was drawn in their study, but similarities can be seen between their results and the spectral response of S1-1-99 and S1-2-99 in Figure 5.6.

Also, when comparing how donor concentration increases with annealing time in section 2.5.2 it is evident that a maximum in donor concentration can be reached. Further, research by C.S Fuller [2] showed that the donor concentration went down after maximum was reached. It was proven that the time it takes to reach a maximum and for the decrease to start was dependent on the samples and the temperatures. When comparing this to the development of the P-line in S1 and S2 set (see Figure 5.6 and Figure 5.7) both could fit with the behaviour of thermal donors. It can be speculated that the mean spectra of S1-2-99 show the DRL at a stage where the donor concentration has started to go down. And that sample S2-5-99 have reached its maximum donor concentration but not yet started the decrease. It should be noted that Fullers work was based on mapping the electron concentrations in the material. As this study has not performed any resistivity measurements due to the thinness of the wafer no certain conclusion can be drawn on this matter.

Sample sets S1 and S2 originates from two different ingots and even though they are samples from commercially produced ingots, the defect distribution will not be identical. So, if the emission lines at the energy levels of 0.66-0.767eV is due to interstitial oxygen then other point defects in the material will influence the formation rate of the defect. The presence of self-interstitials, vacancies and impurities all influence the diffusion rate of interstitial oxygen, and besides carbon content most of these factors are unknown. It would therefore only be speculation on how that could influence the growth rate of the DRL peak. High concentrations of substitutional carbon have been reported to inhibit the growth rate of thermal donors and the P-line. The carbon content in the S1 sample were below the detection limit and only at 0.07 ppma in the S2 sample set. This could contribute to the differences seen between samples S1-2-99 and S2-5-99 in figure 5.11, but due to the low carbon concentrations this is not considered to be a likely explanation.

The thermal history of the sample sets could cause differences in the development of the spectral responses. The S1 sample set had a slower cooling rate after the heating process, which adds to the total annealing time of the samples. However, the extra time spent in the temperature range where TDs form will only be a small portion of the total time spent at 450°C. Therefore, this is not considered to be enough to cause large deviations between the sample sets. Further, the S1 sample set was more exposed to contamination as the heating was performed in ambient air and in a box made of steel. Also, the silicon slices used between the samples and the steel may not have been sufficient to stop contamination. But it is important to keep in mind that 450°C is considered to be low temperatures when it comes to contamination caused by diffusion.

The purpose of the 650°C annealing was to see how the spectra evolved at this temperature, especially to check if emission lines disappeared or decreased. The short-time heat treatment did not eliminate the P-line signal in any of the seed end samples. Other large changes could be observed in the DRL, the peaks at D069, D070, D072 and D074 disappeared from the spectra, and the P-line was left as the sole peak of a broad emission band (see figure 5.11). However, MCR did divide this broad band into two signals, one with a peak at 0.767 and another at D1 (0.807eV). The broad band is therefore most likely a superposition of at least the P-line signal and D1. The result also confirms that the P-line can be present without the peaks at D070, D072 and D074, giving a greater cause to discuss the origin of the emissions seen between 0.66-0.74. A comparison is challenging as these have not been well documented in current literature. However, they have been proven to appear in samples with high thermal donor concentration [24]. As explained in section 2.5.2, TDs are clusters of electrically active interstitial oxygen. And the size and configuration of these clusters are believed to create multiple types of TDs with their own specific centers and introduce two energy levels. As the emissions seen at the energies below the P-line are highly affected by the performed annealing processes they also follow the behavior of TDs. It could therefore be speculated that the emission lines seen at 0.66-0.74 also are TDs.
The spatial distribution for the P-line in the as-cut samples Figure 5.5 showed a clear ring like pattern and relatively low signals in the areas in between. All the annealing steps of the samples in the S1 and S2 sets show a significant change in spatial distribution of the DRL (Figures 5.12-15). But the main features of the distribution that was identified for the as cut samples were still present after all the anneals.

One of the most interesting result can be seen in the image of the S1-2-99 wafer, Figure 5.14. a.) shows a complete redistribution in the DRL emissions at 0.667-0.767eV. The defect responsible for the P-line emission have diffused to the edges of the wafer and accumulated in to one ring formation. The DRL signal is now most prominent in areas where it was absent before the long annealing.

The distribution of DRL in the samples exposed to the short time annealing at 650C show a reduction of the ring-like pattern and in some the structure has completely vanished, see Figure 5.15. The signal is now present in the entire wafer and the high temperatures of 650°C seems to be high enough to cause the defect to diffuse throughout the whole sample.

5.2.4 Spatial distribution of defect related luminescence - spectral range 0.804-0.810eV

This section will present the spatially resolved images of samples S1-2-24, S1-2-99, S1-2-650, S2-2-24, S2-3-66, S2-4-650 and S2-5-99 for the DRL in the spectral range of 0.804-0.810eV, which covers the D1 emission line at 0.807eV. See Figure 5.16 for an overview.

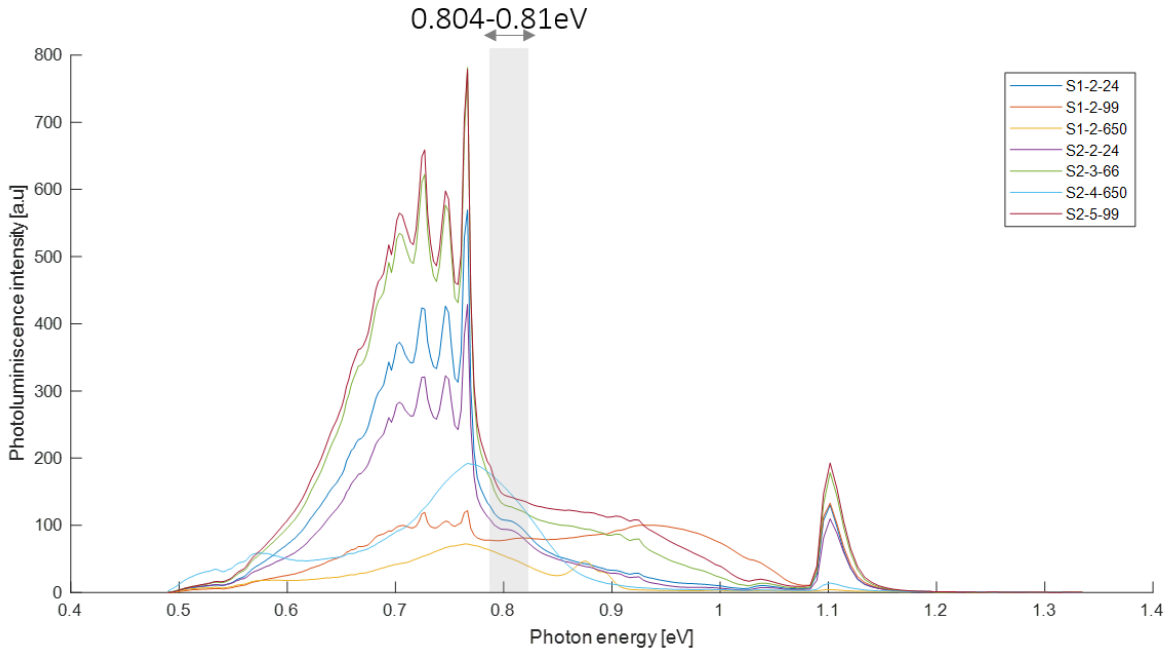

Figure 5.16: The covered spectra in this section is highlighted in the graph, the plot shows the mean spectra of some selected samples from both S1 and S2 set.

The spatial distribution of the D1 defect in sample sets S1 and S2 after various heat treatments can be seen in Figure 5.17 for samples a.) S1-2-24, b.) S1-2-99, c.) S2-2-24, d.) S2-3-66, e.) S2-5-99.

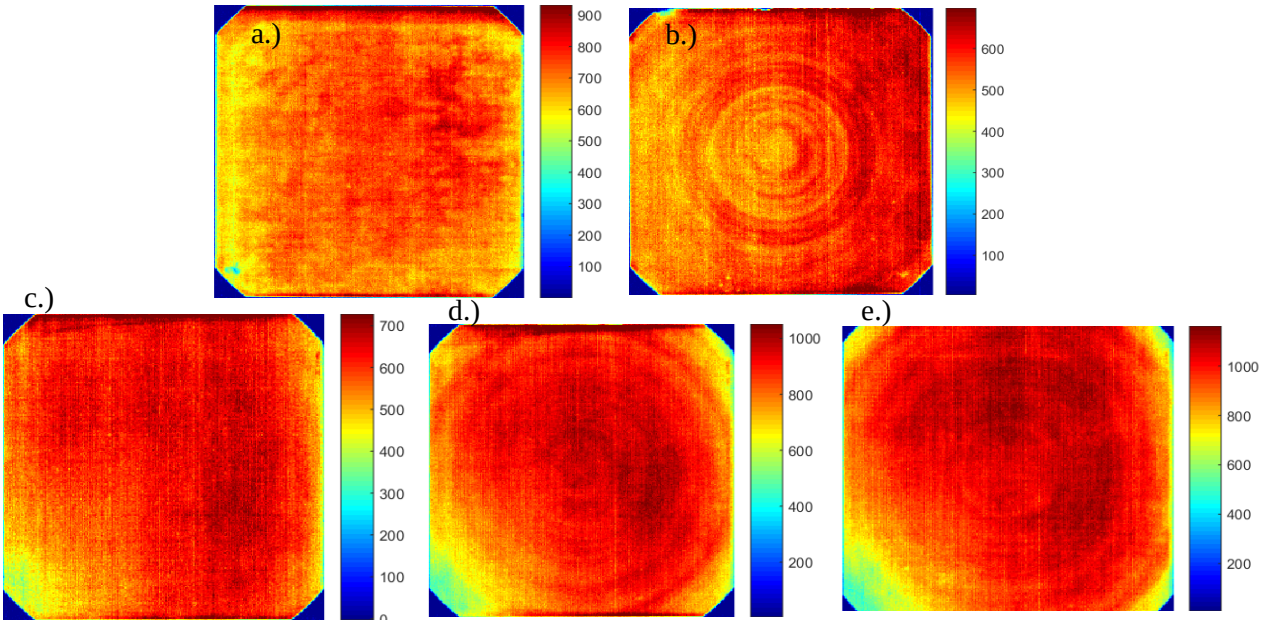

Figure 5.17: The spatial distribution of the D1 defect in sample sets S1 and S2 after various annealing process for samples a.) S1-2-24, b.) S1-2-99, c.) S2-2-24, d.) S2-3-66, e.) S2-5-99

No distinct attributes can be seen in the images of the D1 signal, besides that it is uniformly distributed in the majority of the samples, and some ring-like patterns can be found in the samples with the longest annealing time b.), d.) and e.)).

5.2.5 Section discussion of defect related luminescence - spectral range 0.804-0.814eV

The D1(0.807eV) signal is the only prominent signal in this spectral range and the only signal that will be discussed. This signal could not be detected in the as cut samples (Figure 5.11), and first appeared after the 24-hour annealing. This happened in all the wafers and is thus a reoccurring phenomenon. The D1 signal could also be identified with MCR.

The hyperspectral images show that the D1 signal is uniformly distributed throughout the whole wafer and that the signal is not restricted to any particular region. In the literature the D1 signal is well documented and have been connected to emissions caused by dislocations or oxygen precipitation at dislocations [27, 4]. Dislocations are expected to appear as localised lines or small rings. Therefore, none of the images seen in figure 5.17 matches with how dislocations are expected to appear. Also, the samples are commercially produced and not exposed to any treatment that could cause a uniform spread of dislocation throughout the sample. It is also unlikely that the annealing methods used in this study could create dislocations of this extent. The emission line at 0.807 eV was not present before the thermal treatment, implying that temperatures of 450°C is enough to form the defect.

It is possible that the 0.807 eV signal seen in this study is caused by another defect at very similar energy as the D1 defect, since it is well-established that the D1 signal is connected to dislocations.

5.2.6 Spatial distribution of defect related luminescence - spectral range of 0.895-1.01 eV.

This section will present the spatially resolved images of the emission lines at the energies between 0.895-1.010eV for the selected samples, as shown in Figure 5.18 it will cover the DRL at the H-line and the D090, and followed by a discussion.

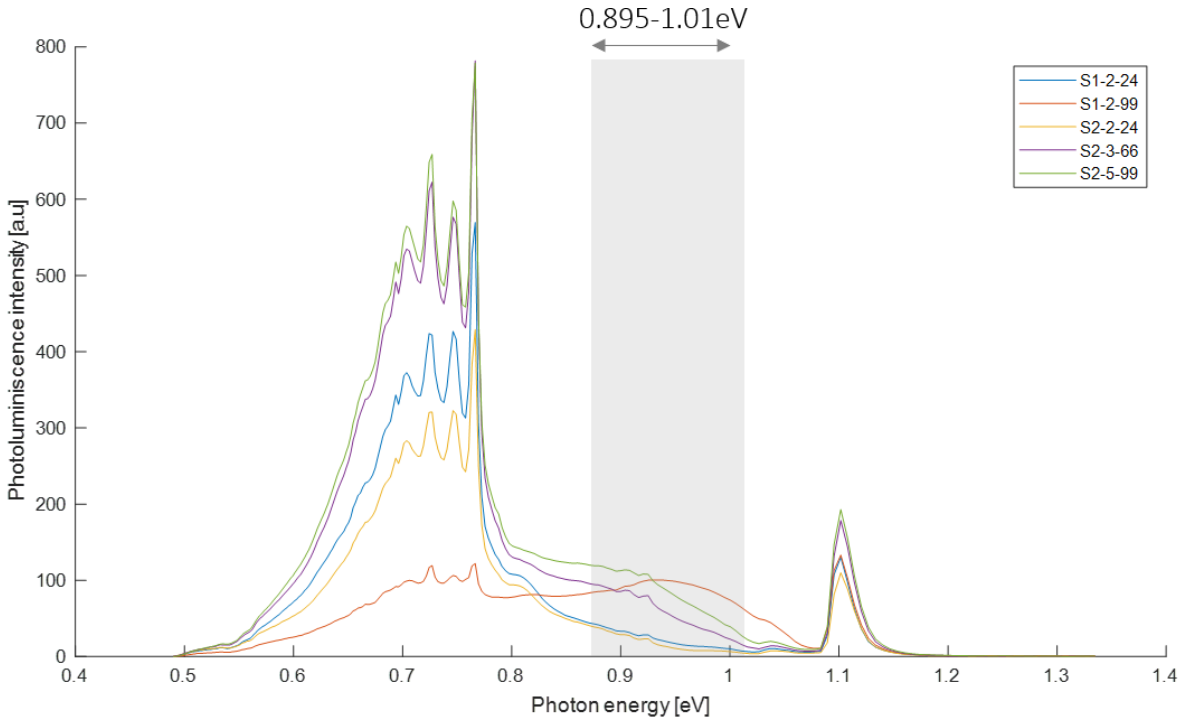

Figure 5.18: The covered spectra in this section is highlighted in the graph, the plot shows the mean spectra of some selected samples from both S1 and S2 set

Figure 5.19 shows the images of samples a.) S1-2-24, b.) S2-2-24, c.) S2-3-66 d.) S1-2 99 and e.) S2-5-99. The distribution of the defect follows the same characteristics as the spatial images of the P-line, with a ring-like pattern. The heating of the samples causes the distribution of the DRL to spread in the wafer and increase in intensity.

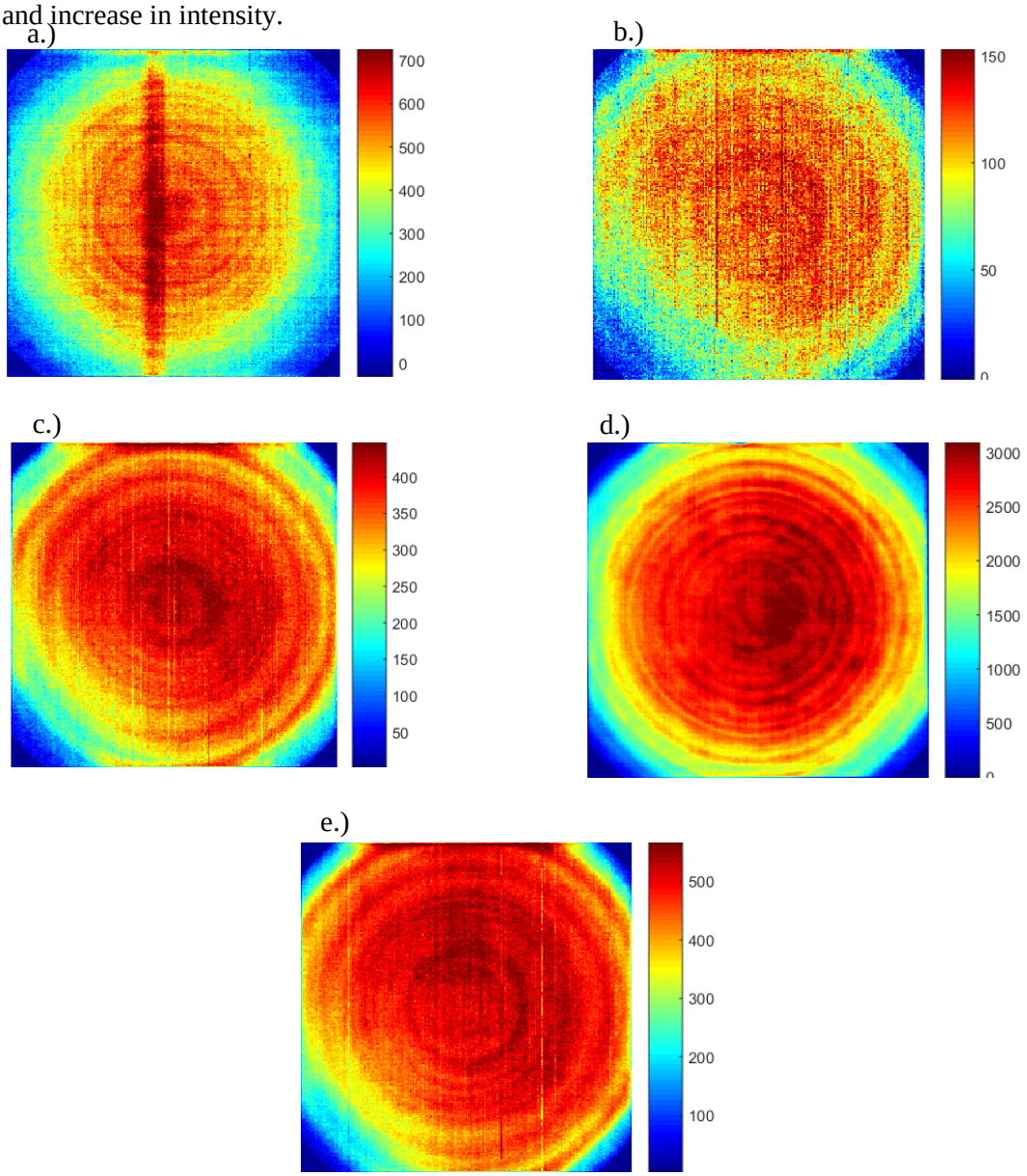

Figure 5.19: Spatial distribution of the DRL signals in the spectral range of 0.895-1.101eV a.) S1-2-24, b.) S2-2-24, c.) S2-3-66 d.) S1-2 99 and e.) S2-5-99.

In image a.) a line can be seen vertically along the sample, and this is a result of the direction of the sample under the hyperspectral PL imaging. It was found that if the wafer was placed with the sawing pattern in parallel with the laser beam this line appeared in the spatially resolved image, and this was later avoided by placing the sawing pattern normally to the laser beam. The line could possibly be due to increased scattering in the area due to irregularities in the saw pattern.

Section discussion of defect related luminescence - spectral range 0.895-1.01 eV

In this spectral range two peaks can be observed in the mean spectra, and an overview of the relevant peaks discussed in this section can be seen in Table 5.3.

Name	Peak
H line	0.925eV
D090	0.904eV

Table 5.3: An overview of the peaks that can be observed in the spectral range of 0.895-1.01eV in Figure 5.18.

The spectra in Figure 5.18 shows that temperatures of 450°C cause the H-line and D090 to form and grow. When observing the results in Figure 5.18 it can be concluded that higher temperatures of 650°C is enough to cause a dissociation of the defect. The spatial distribution of the DRL in figure 5.19 indicate that it could have a connection to oxygen as it is present with the same ring structures as discussed in section 5.2.3. As mention in section 3, the signal at 0.9251 eV, the H-line, was discussed by Minaev [23]. The spectral response (see figure 5.18) after the 100h annealing reminded of the mean spectra seen in S1-2-99. A wide emission band with a local peak at the H-line was present and the P-line had somewhat decreased. It was concluded that the H-line had a connection to oxygen and possibly carbon. The wide emission band seen in the mean spectra of S1-2-99 is most likely due to superposition of emission lines close in energy. MCR managed to separate the band into two, but with no distinct peaks as illustrated in figure 5.10. Its therefore probable that the emission band toward 1.0eV is a superposition of several emission signals. It is hard to conclude on which other emissions that could be a part of the superposition.

As mentioned in section 5.2.7 the spatial distribution of the DRL in the spectral range of 0.667-0.767 was redistributed in sample S1-2-99. Figure 5.20 shows the spatial distribution of DRL in sample S1-2-99 between a.) 0.667-0.767eV and b.)0.89-1.00eV. It can appear as the DRL associated with the P-line and TDs have been replaced by the DRL presented in this section. So, from this it could appear that the P-line signal is replaced by another signal.

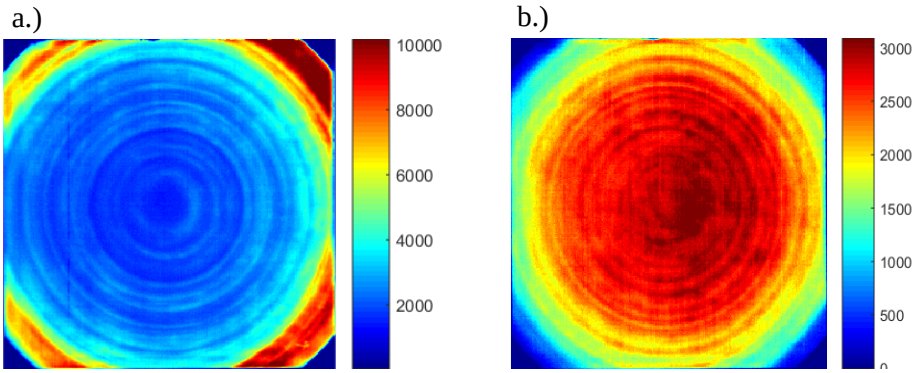

Figure 5.20: show the spatial distribution of the DRL signal in the range of a.)0.667-0.767eV and b.)0.895-1.01eV in wafer S1-2-99. The distribution of the DRL signals look like opposites of each other.

5.2.7 Spatial distribution of the band to band luminescence.

This section will present the spatial distribution of the BB signal in the seed end samples S1-2-24, S1-2-99, S1-2-650, S2-2-24, S2-3-66, S2-4-650 as shown in Figure 5.21. This was not a part of the DRL explained in chapter 2 but refer to the emission that occur at BB recombination.

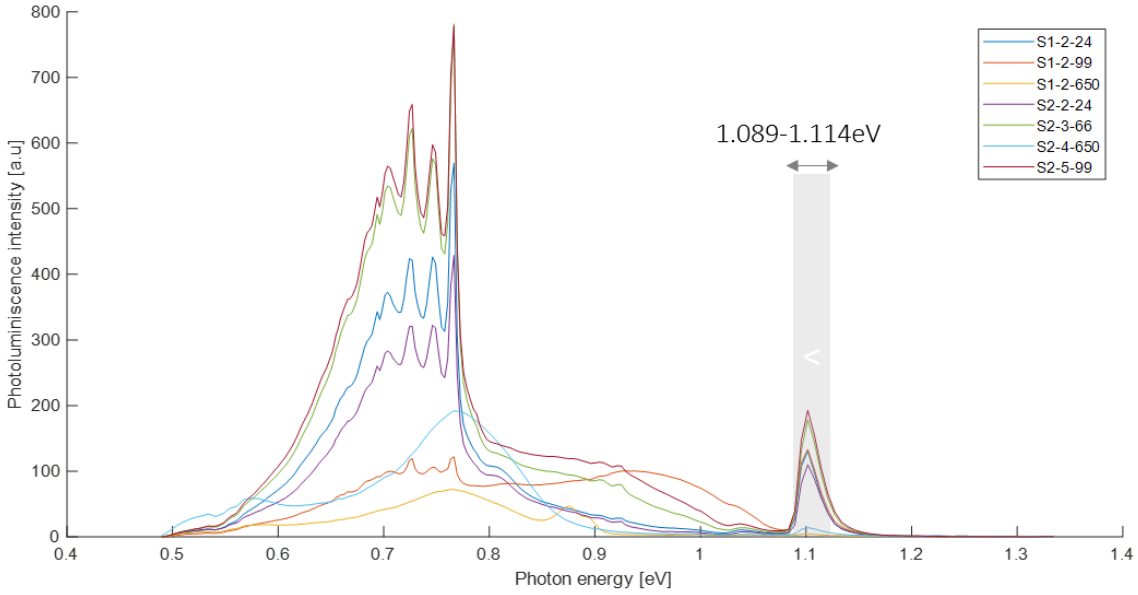

Figure 5.21: The covered spectra in this section is highlighted in the graph (BB luminescence.), the plot shows the mean spectra of some selected samples from both S1 and S2 set.

The effect of the various heat treatments on spatial distribution of the BB luminescence is presented in Figure 5.22. The image of the BB signal in the as cut sample appear as noise due to the low intensities (a.). The rest of the images show a steady increase in intensity with annealing time. The distribution of

the signal varies slightly between the samples, but all samples show low signals at the edges. Sample c.) S1-2-99 deviate from the other samples, where low BB signals can be seen in a ring pattern at the centre of the sample.

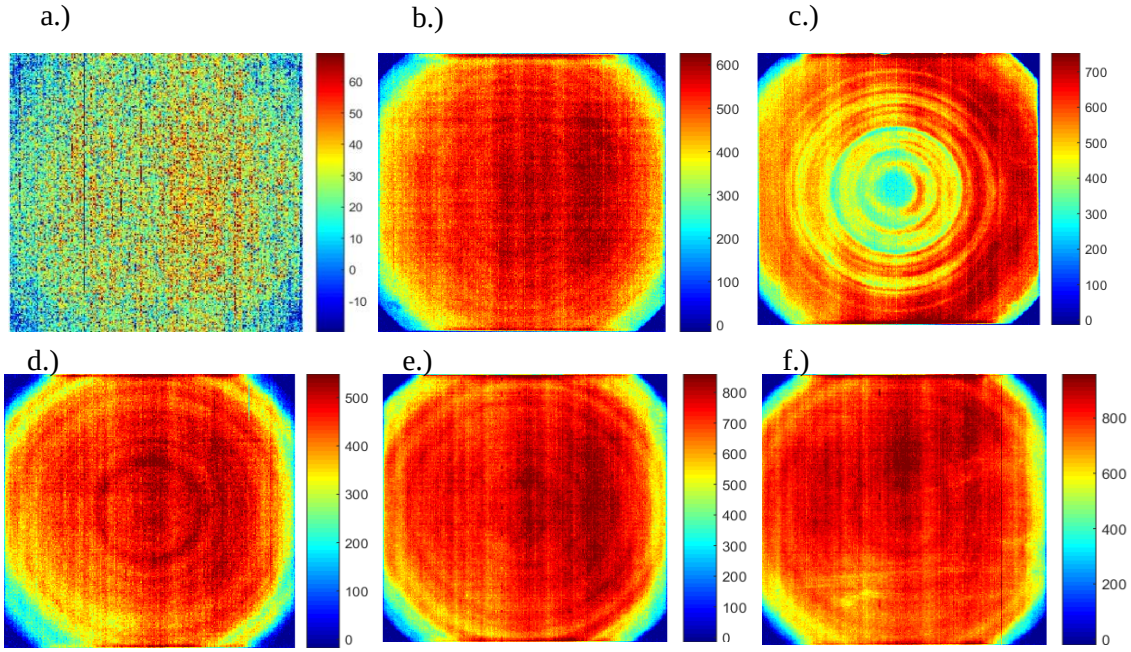

Figure 5.22: The spatial distribution of the BB signal in wafers a.) S2-1 b.) S1-2-24 c.) S1-2-99 d.) S2-2-24 e.) S2-3-66 f.) S2-5-99

5.2.8 Section discussion of band to band luminescence

The generally low intensity of the BB luminescence can be explained by a high level of surface recombination and scattering at the surface, as the wafers are not passivated or etched. However, the increase of BB luminescence as a response to the annealing process at 450°C is an unexpected result. As this occurs in all the samples at this temperature, and the fact that it grows with time, it is unlikely that this phenomenon is connected to the setup and annealing method. When the wafers are exposed to temperatures of around 650°C the intensity of the signal goes down to values similar to before heat treatment. It therefore appears as if the BB luminescence is influenced by the intensity growth in DRL. When comparing the mean spectra in Figure 5.6 and 5.7 it is not possible to link the increase directly to any of the DRL emissions.

Hypothetically, the defects behind the DRL emissions could be caused by thermal donors. A single interstitial oxygen atom is believed to be positioned between two silicon atoms as suggested in figure 2.12. When the interstitial oxygen agglomerates into larger oxygen clusters they become electrically active clusters of TDs. By forming into large clusters there are fewer connections made with silicon atoms, which could potentially leave more silicon atoms available to create covalent bonds with each other, and thereby increase the intensity of the BB signal.

Lastly, the low intensities at the edges (see Figure 5.22) can probably be connected to a high level of surface recombination as well.

5.3 THERMAL ANNEALING OF TAIL END SAMPLES

Spectral imaging was performed after each annealing step to document any development of the spectral response. Figure 5.23 shows the mean spectra of the samples in T1 set, the set exists of samples T1-1-24, T1-1-99, T1-2-24, T1-2-99 and T1-2-650 and these are the samples that were exposed to repeated heating and cooling. When studying the mean spectra of the T1 sample set the spectral response shows the same characteristics as the seed end samples. The DRL between 0.667-767eV increases in intensity with annealing time but at a much lower rate than in the previous samples. Again, the D1 signal is present already after 24 hours at 450°C. The H-line and D090 emissions do not appear in the spectra until after 99 hours and are present at very low intensities. The short time heating at 650°C results in one wide emission band with its peak at 0.767 eV. When comparing the mean spectra of T1-2-99 and T1-2-650 a significant difference can be seen between the two P-line peaks. This show that the intensity of the P-line emission can be reduced when the wafer is exposed to higher temperatures. As with the seed end samples, the intensity of the BB luminescence is strongly affected by the annealing performed at 450°C.

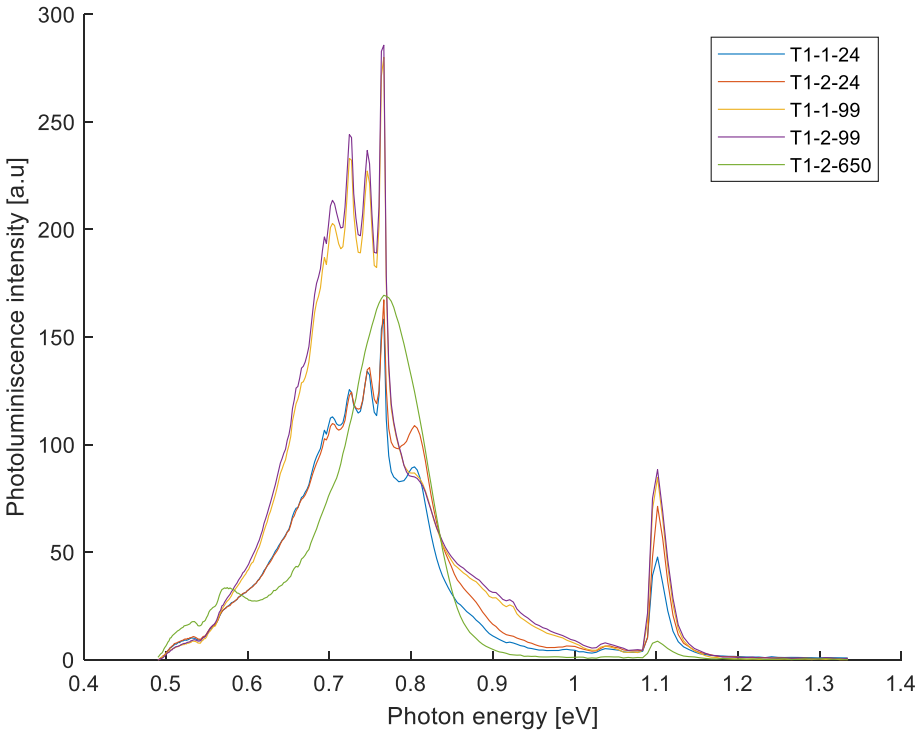

Figure 5.23: A comparison of the mean spectra from each heat treatment step of the samples in the T1 set. Multiple new emission lines were formed in the energy range of 0.807-0.925eV at temperatures of 450°C and at temperatures of 650°C many of the same emission lines is eliminated from the spectra.

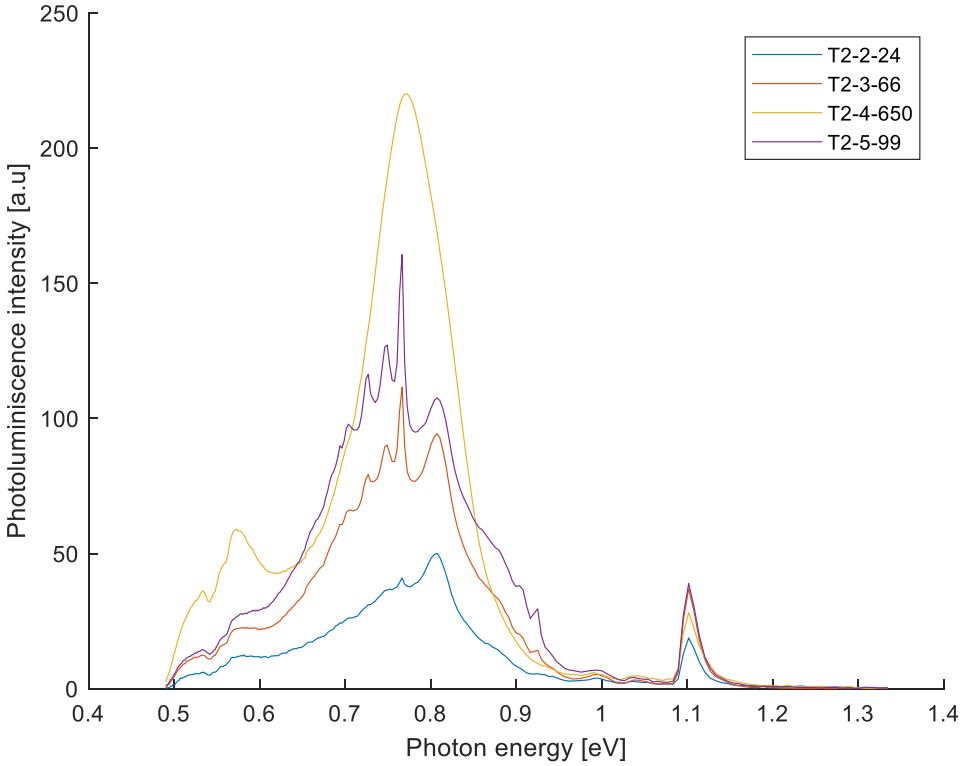

Figure 5.24: A comparison of the mean spectra from each heat treatment step of the samples in the T2 set. Multiple new emission lines formed in the energy range of 0.807-0.925eV at temperatures of 450°C and at temperatures of 650°C many of the same emission lines are eliminated from the spectra.

Further, the spectra of the T2 sample set can be seen in Figure 5.24, which presents the spectra from wafers T2-1, T2-2-24, T2-3-66, T2-4-650 and T2-5-99. Note that the integrated spectra from T2-2-24 is only from half a sample. When comparing the mean spectra found in this wafer with that of T1-2-24 in Figure 5.23, clear differences can be spotted in the distribution of DRL of 0.667-0.767, notably that the D1 peak is here higher than the P-line peak.

S2-3-66 provided a mean spectra with the common traits seen throughout this study, with a growth of the peaks between 0.701-0.767 eV together with the D1 signal, D090 and H-line. The shoulder next to the D1 line have grown wider and indicate a peak at 0.875 eV (D2).

The annealing process of T2-5-99 results in a P-line peak with slightly higher intensities than sample T2-3-66. The D090 signal in T2-5-99 is present at higher intensities than the H-line, and the D2 emission is also more prominent.

The short time heating of sample S2-4-650 resulted in a mean spectra where the DRL signals are the same as the other samples exposed to the temperatures of 650°C. The emission lines at D070, D072, D074, D090 and the H-line have all disappeared, and one wide emission band is left with a peak at the P-line. When observing the mean spectra in figure 5.24 it looks like the P-line peak of S2-4-650 is higher

than the other peaks in the mean spectra, indicating that 650°C annealing resulted in a growth of the P-line.

Again, an increase of the BB luminescence can be observed as a result of the annealing process. The BB luminescence does not go down to as cut values in the sample exposed to the short time annealing, T2-5-66

Table 5.4 gives an overview of the DRL that is present in the mean spectra of all the tail end samples.

SAMPLE	P LINE	H LINE	D1	D074	D072	D070	D069	D090	NOTES
T1-1-24h	✓		✓	✓	✓	✓	✓		
T1-2-24h	✓		✓	✓	✓	✓	✓		
T1-1-99h	✓	✓	✓	✓	✓	✓	✓	✓	
T1-2-99h	✓	✓	✓	✓	✓	✓	✓	✓	
T1-2-650C	✓								Broad band with P line peak.
T2-2-24h	✓		✓						Broad band over the D070-D074
T2-3-66h	✓	✓	✓	✓	✓	✓	✓	✓	Shoulder at 0.87 eV
T2-4-650C	✓								Broad band with P line as peak
T2-5-99h	✓	✓	✓	✓	✓	✓	✓	✓	Shoulder at 0.87 eV

Table 5.4: DRL signals identified in the seed end sample sets, T1 and T2, after the performed annealing processes.

5.3.1 MCR analysis thermally annealed tail end wafers

The MCR plot for a.) T1-2-99 and b.) T2-5-99 and c.) T2-4-650 are shown in Figure 5.25. For both a.) and b.) none of the signals between 0.667-0.767eV could be separated. The only signal that is extracted as its own is the D1 signal in component 3 in a.) and component 3 in b.). And the MCR loading plot in c.) show that the P-line and D1 signal can be separated as component 1 and 2, respectively.

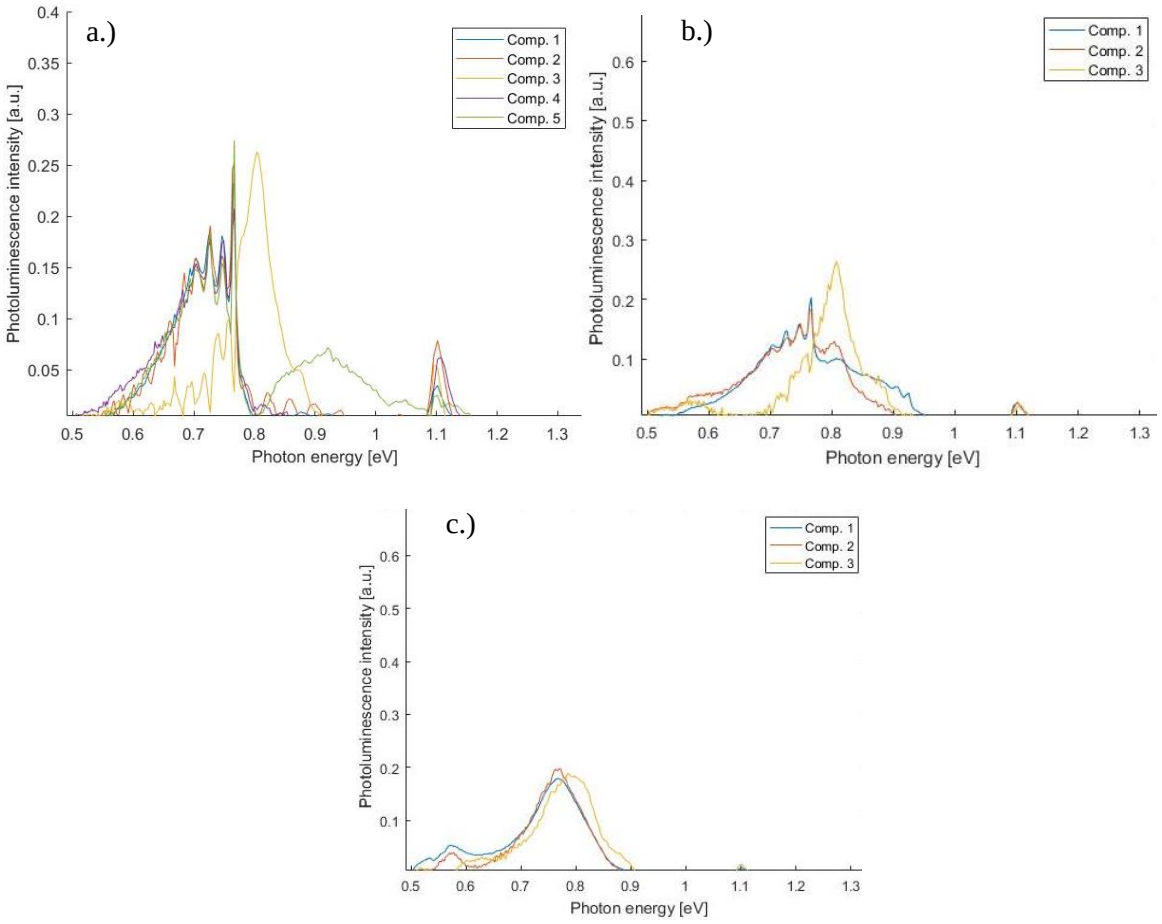

Figure 5.25: The loadings plots for the MCR analysis for a.) T1-2-99 with components 1-5, b.) T2-5-99 with components 1-3 and c.) T2-4-650 with components 1-3.

5.3.2 Spatial distribution of defect related luminescence - spectral range 0.667-0.767 eV

The spatial distribution of the DRL emissions in the range of 0.667-0.767eV for samples T1-2-24, T1-2-99, T2-2-650, T2-2-24, T2-3-66, T2-5-99 and T2-4-650, are shown in Figure 5.26 which highlights the spectral range this chapter will cover.

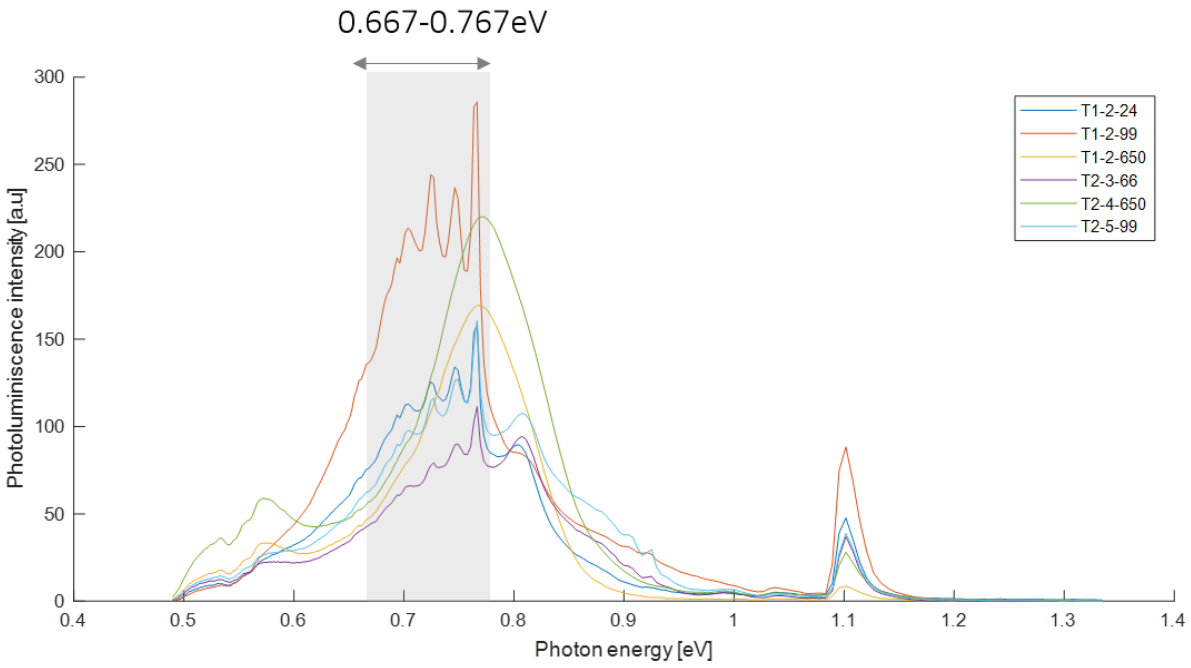

Figure 5.26: The covered spectra in this section is highlighted in the graph, and the plot shows the mean spectra of some selected samples from both T1 and T2 set

Spatial distribution of luminescence emissions in the energy range of 0.667-0.767eV from the tail end sample set T1 is presented in Figure 5.27 a.) T1-2-24 and b.) T2-2-24. The characteristic ring-like pattern is present in both wafers, where the highest DRL signals can be seen between the rings and at the centre. The only region where the signal is absent is at the edges a.). Image b.) show half of the T2-2-24 wafer, and it is challenging to conclude if there is a ring pattern present in the sample, but it appears that a clear difference can be seen compared to image a.).

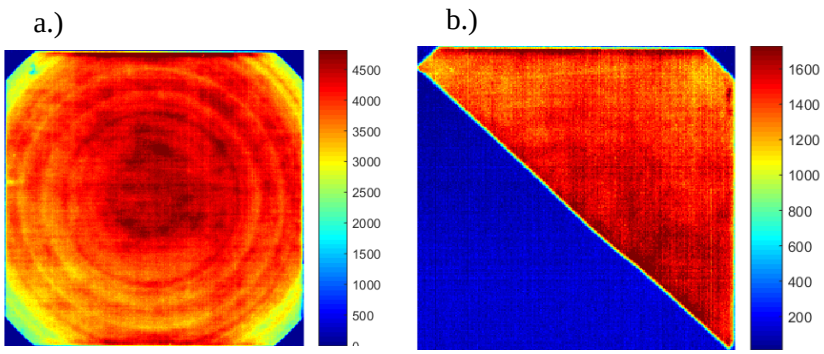

Figure 5.27: The spatial distribution of DRL signal in the spectral range 0.667-0.767eV in wafers a.) T1-2-24 and b.) T2-2-24.

Sample T2-3-66 is the only tail end wafer that was exposed to the 66-hour anneal at 450°C, and Figure 5.28 shows the spatially resolved image of the DRL. The highest intensities of the DRL signals can be seen inside the rings and with a decreasing trend radially toward the edges.

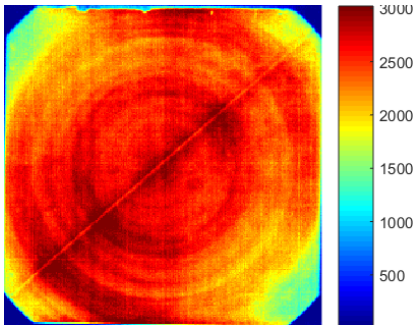

Figure 5.28: DRL signal in the spectral range 0.667-0.767eV in wafers T2-3-66.

The longest annealing interval at 450C° was performed on samples T1-2-99 and T2-5-99, and Figure 5.29 a.) and b.) show the spatially resolved images for these samples. Here the spatial distribution of the signal can still be seen as a ring pattern.

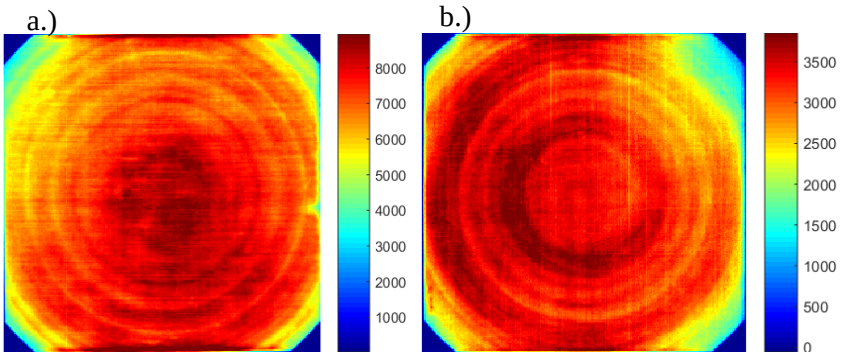

Figure 5.29: Distribution of the DRL signals in the range of 0.667-0.767eV in a.) T1-2-99 and b.) T2-5-99.

Samples T1-2-99 and T1-2-24 (seen in Figure 5.27 a.) are the same wafer but with different annealing time. When comparing the DRL between them it can appear as if the signal has switched sides, first being strongest at the top in T1-2-24 and then changed to being strongest at the bottom in sample T1-2-99. But it could be that the samples were accidently placed in opposite directions, implying being rotated 180°.

Figure 5.30 shows the short time heating at 650 °C of the tail end samples T1-2-650 a.) and T2-4-650 b.). As with previously described samples the spatial distribution of the DRL signal of 0.667-0.767eV changes at the higher temperatures. The ring pattern is completely absent, and in sample T2-4-650 the short time annealing process resulted in an increase of the DRL signal at the P-line, as can be seen in image b.). The line visible along the right side in image a.) is caused by accidently touching the sample when placed for hyperspectral imaging.

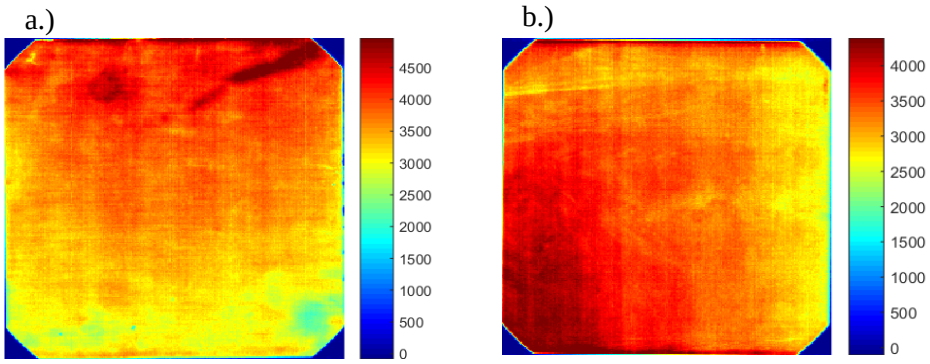

Figure 5.30: Spatial distribution of DRL signal in the spectral range 0.667-0.767eV in wafers a.) T1-2-650 and b.) T2-4-650.

5.3.3 Section discussion of defect related luminescence - spectral range 0.667-0.767

Several emission lines are present in this spectral range, and an overview of the relevant peaks discussed in this section can be seen in Table 5.5.

Name	Peak
P line	0.767eV
D069	0.693eV
D070	0.702eV
D072	0.724eV
D074	0.746eV

Table 5.5: An overview of the peaks that can be observed in the spectral range of 0.667-0.767eV.

The DRL signals that are present in the spectral range of 0.667 - 0.767eV in the tail end samples matches well with the findings from seed end samples. The peaks at D069, D070, D072, D074 all form simultaneously as the P-line after 24 hours and increase at the same rate. The growth rate is considerably slower in sample T2 set compared to T1 set (see Figure 5.26) and the peaks ends up at lower intensities after 99 hours at 450°C. Due to such clear differences in the intensities of the DRL these are unlikely to be caused by differences in the set up. As discussed in section 3 close relations between the P-line, interstitial oxygen, temperatures of 450°C and thermal donors have been established [6, 24]. The P-line is indeed present in the samples with low oxygen content, but the growth rate is significantly lower. Since sample T2 have such a low interstitial oxygen concentration (2.68 ppma.) and still show a significant presence of the defect, it confirms a clear dependency on the temperature of 450°C. It is natural to propose that the differences in the growth rate between the samples are caused by interstitial oxygen content, as T1 had a concentration of 12.05ppma which is substantial higher than had T2.

Short time anneals at 650°C resulted in the disappearance of several DRL peaks. In accordance to seed end samples, only one wide DRL emission band with a local peak at the P-line can be observed in the mean spectra of T1-2-650 and T2-4-650 in Figure 5.26. However, the most interesting result can be seen in the mean spectra of sample T2-4-650, where the P-line is present at intensities above all the samples exposed to 450°C. This deviates from all the other samples that was exposed to these temperatures and most of available literature. But as discussed in section 2.5.2 in the study performed by Götz a similar behaviour could be observed regarding donor concentration [21]. After exposing samples of temperatures of 650°C he reported of an initial increase in donor concentration in samples with low oxygen concentration. Meanwhile in the samples with high oxygen content they followed what other experimental work have established, that annealing temperatures above 650°C eliminates the TDs in the material. The results of the tail end wafers fit well with this observation and the

connection with thermal donors should not be rejected because of the results from T2-4-650. The spatial distribution of the signal does not appear in a ring-like pattern and has increased in intensity, showing that temperatures of 650°C is enough to cause the defect to diffuse out of the ring pattern and distribute uniformly in the wafer (see Figure 5.30).

The concentration of substitutional carbon is also high in the T2 sample set, and carbon is claimed to have an inhibiting effect on the generation of thermal donors. It could be suggested that this also could lower the growth rate of the P-line, but due to the low oxygen concentrations it is hard to draw any conclusions.

5.3.4 Spatial distribution of defect related luminescence - spectral range 0.804-0.810eV

This chapter covers spatial distribution of the DRL emission in the spectral range of 0.804-0.810eV and Figure 5.31 shows which spectral range this will cover in the mean spectra and give an overview of the samples discussed in this section.

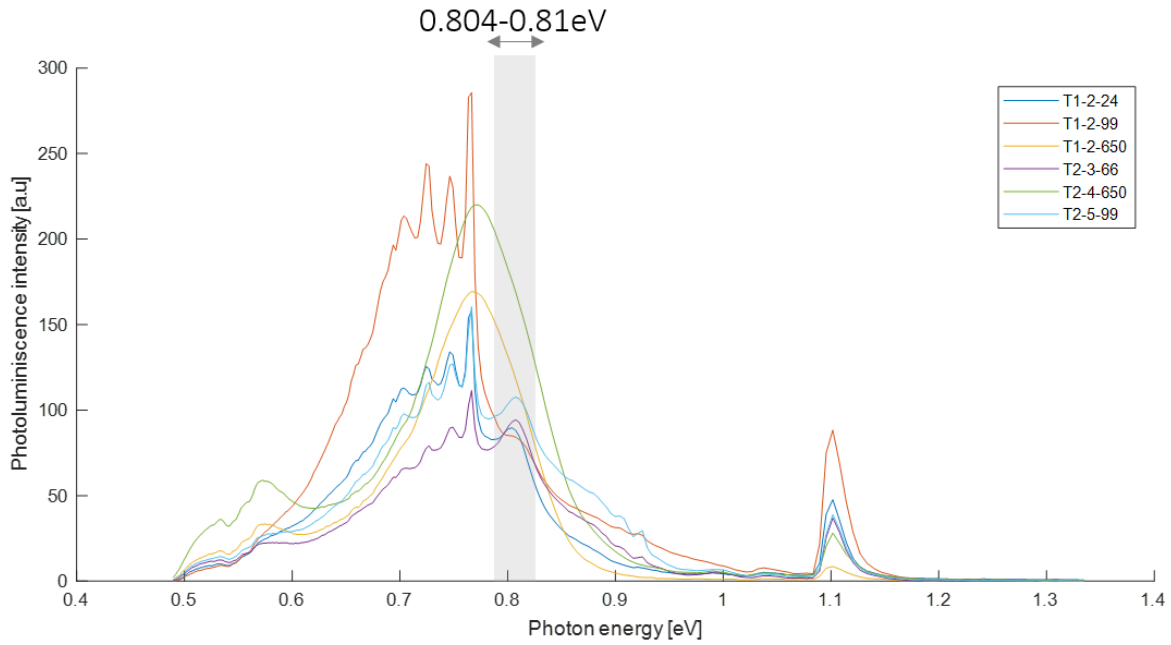

Figure 5.31: Covered spectra in this section is highlighted in the graph, and the plot shows the mean spectra of some selected samples from both T1 and T2 set.

The luminescence at the D1 emission became present in wafers after the first heating process at 24 hours and increased with each annealing process at 450°C. As the spatial characteristics did not change under the process the spatial distribution of the D1 signal in the samples will be presented together, and only the samples with the same annealing time will be chosen. Figure 5.32 shows samples a.) T1-2-24, b.) T2-2-24, c.) T1-2-99, d.) T2-5-99, e.) T1-1-650 and f.) T2-4-650. As in the seed end samples the D1 is

uniformly distributed throughout the entire wafer, where the highest intensities can be seen in the in samples exposed to the short time annealing.

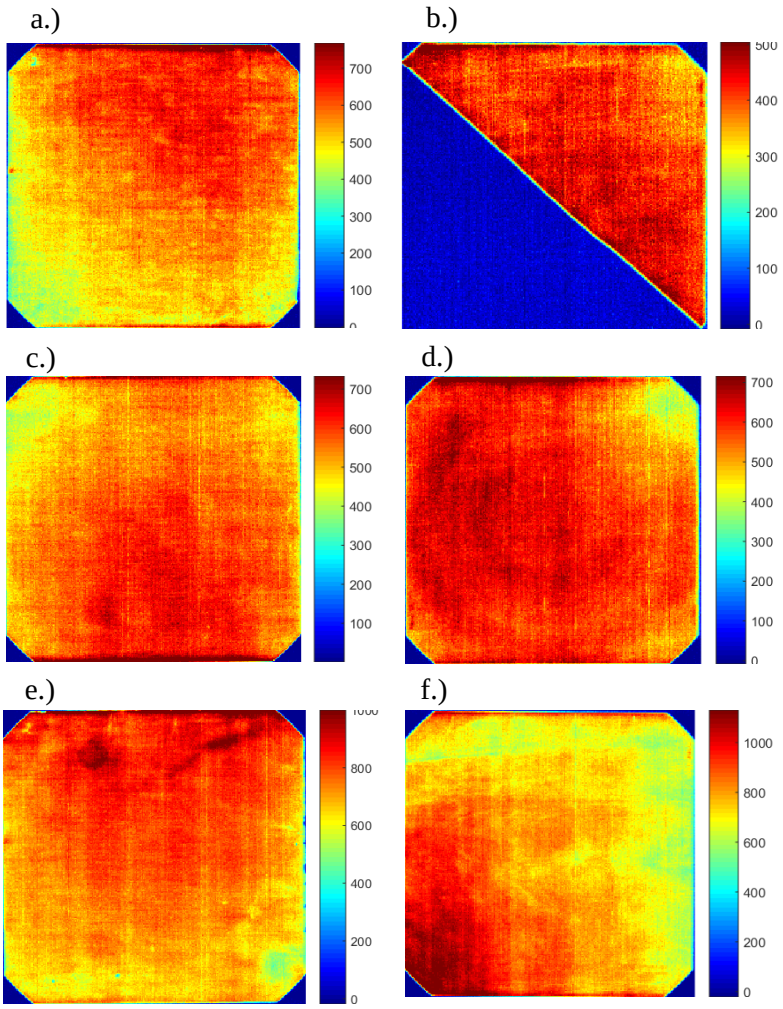

Figure 5.32: The spatial distribution of the DRL in the spectral range of 0.804-0.810 eV samples a.) T1-2-24, b.) T2-2-24, c.) T1-2-99, d.) T2-5-99, e.) T1-1-650 and f.) T2-4-650.

5.3.5 Section discussion of defect related luminescence - spectral range 0.804-0.814eV

The D1 signal (0.807eV) is the only prominent signal in this spectral range and the only signal that will be discussed. As with the seed end samples, this signal is also present in the tail end samples after 24 hours at 450°C. When comparing with other peaks in the mean spectra the D1 peak appear at the same intensities as the D070 peak in Figure 5.31. Again, the spatial distribution of the D1 defect does not match the characteristics of dislocations as discussed in section 5.2.5, and the temperatures at which the D1 emission form in this study does not comply with other literatures. The broad band that is present after the 650°C heating has been concluded to be an overlap of both the D1 and P-line. It can therefore be shown that the D1 signal is not absent after higher temperatures and has actually grown in intensity in the T2-4-650 sample.

5.3.6 Spatial distribution of defect related luminescence - spectral range 0.895-0.925eV

The spatial distribution of the DRL emission in the spectral range of 0.895-0.925eV in samples, T1-2-99, T2-3-66, T2-5-99 will be presented. Figure 5.33 highlights which spectral range this till cover in the mean spectra and give an overview of the samples discussed in this section.

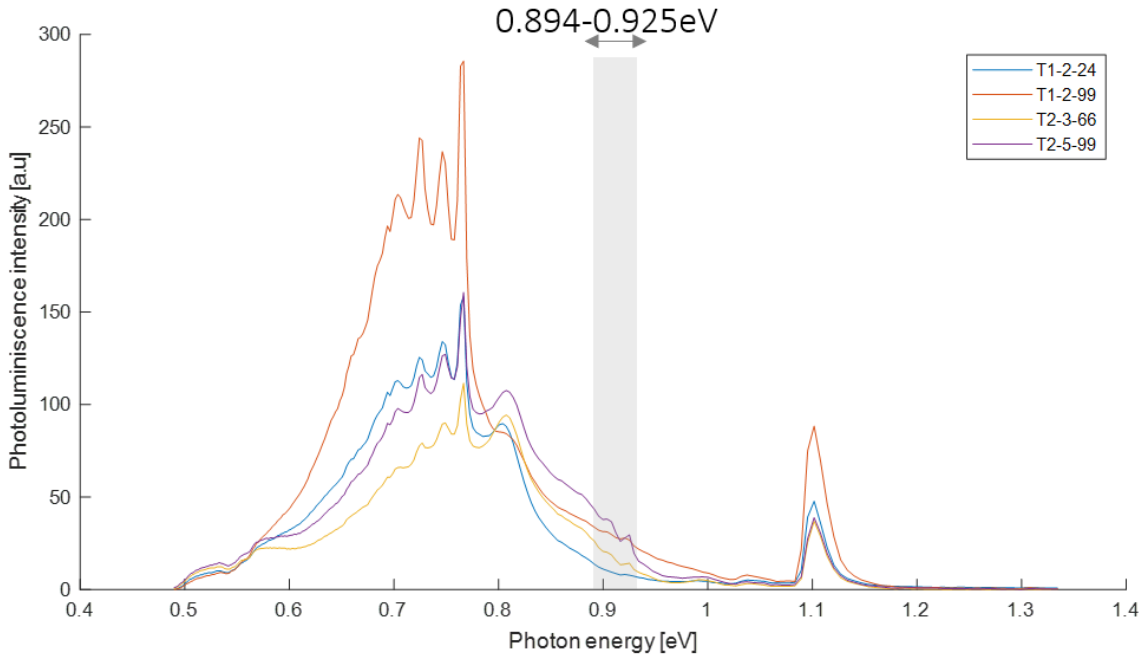

Figure 5.33: The covered spectra in this section is highlighted in the graph, the plot shows the mean spectra of some selected samples from both T1 and T2 set.

The DRL emissions in the energy range of 0.904-0.925 started appearing in the samples after the 24 hour anneal at 450°C, but due to low signals the spatial distribution appear as noise, after the long-time annealing of 99h the structure of the signal can be observed and is presented in Figure 5.34 a.) T1-2-99 and b.) T2-5-99. As in the seed end samples it is distributed in a ring like pattern formed from the centre.

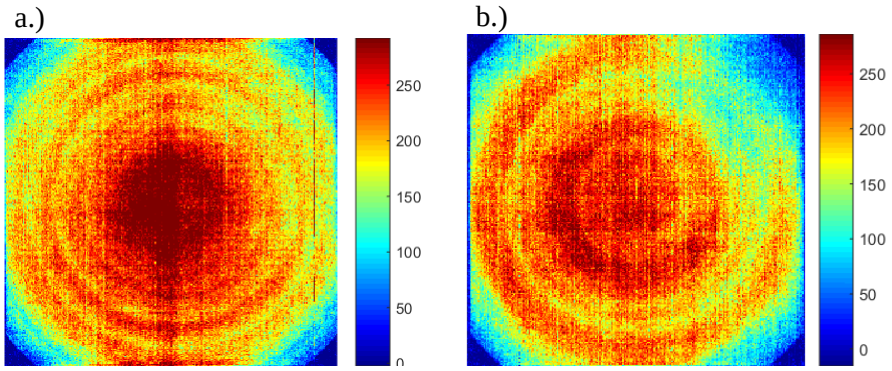

Figure 5.34: The spatial distribution of the DRL signal in the spectral range of 0.895-0.925eV in wafers a.) T1-2-99 and b.) T2-5-99.

5.3.7 Section discussion of defect related luminescence - spectral range 0.895-0.925eV

In this spectral range two peaks can be observed in the mean spectra, and an overview of the relevant peaks discussed in this section can be seen in Table 5.6.

Name	Peak
H line	0.925eV
D090	0.904eV

Table 5.6: An overview of the peaks that can be observed in the spectral range of 0.89-0.925eV.

When comparing the mean spectra in figure Figure 5.33 the emissions in the spectral range of 0.895-0.925 eV is not present in the sample T1-2-24 and T2-2-24 after the first heat treatment. It appears first in sample T2-2-66 and T1-2-99 which show that long annealing time is needed to form the defect in the tail end samples. Both D090 and the H-line appear simultaneously in the samples and D090 exceed the intensities of H-line. The low presence of the signal could be related to low oxygen content in the tail end samples. However, the differences in oxygen concentrations between T1 and T2 sets does not reflect in the results as when comparing T1-2-99 and T2-5-99 as the peaks reach similar intensities. Both signals disappear at temperatures of 650°C showing that the defects behind the emissions diffuses out rapidly. This matches with the temperatures needed to eliminate thermal donors.

5.3.8 Discussion across seed and tail end sample sets

It is evident that the seed and tail end samples shares many of the same characteristics in terms of DRL emissions that evolve at temperatures of 450°C and 650°C. The majority of the samples show the same DRL emissions in the mean spectra, where the main difference can be observed in the intensities of the signals and in the relationships between the peaks. The spatial distribution of the DRL emission over the whole spectral range all appear with the same features throughout the various heating treatments. Table 5.7 give an overview of the spatial characteristics that can be ascribed each DRL peak in this study. The spatial characteristics that are listed applies for both seed and tail end wafers.

Emission line	Main characteristic in spatial distribution	Notes
D069-D070	Ring like distribution Decrease radially toward edges Absent at edges	• Anneals of T=450°C cause the defect to diffuse into a more uniform distribution in the wafer. • In 2 of the wafers the long anneal redistributed the signal as a concentric ring at the edges. • Not present at T=650°C.
P line	Ring like distribution Decrease radially toward wafer edges Absent at edges	• Anneals of T=450°C cause the defect to diffuse into a more uniform distribution in the wafer. • In 2 of the wafers the long anneal redistributed the signal as a concentric ring at the edges. • Anneals of T=650°C the defect diffuse out of the ring structure and is evenly distributed in the wafer
D1	Evenly distributed	• Appear at T=450C°C
D090	Ring like distribution	• Appear at T=450°C • In 2 of wafers the long anneal showed an complementary spatial distribution to the distribution of D069-D070 and P line • Not present at T=650°C
H line	Ring like distribution	• Appear at T=450°C • In 2 of wafers the long anneal showed an complementary spatial distribution to the distribution of D069-D070 and P line • Not present at T=650°C
BB	Highest intensity in centre, slight ring like distribution Absent at edges	• Anneals of T=450C° increase signal

Table 5.7: give an overview of the spatial characteristics that can be ascribed each DRL peak seen in both seed and tail end samples.

In the theory of this thesis it has been discussed how TD concentrations and the intensity of P-line have a dependence of interstitial oxygen (section 2.5.2 and 3). It is therefore of interest to compare the growth rate of the P-line between seed and tail end, as the samples differs significantly in terms of interstitial oxygen concentration. As mentioned, caution should be advised when comparing intensities between the sample set. But as there is such evident differences in the intensities of the DRL emission between seed and tail end set, it is highly unlikely an effect of set up differences. To create a clearer overview of the growth rate differences between tail and seed at 450°C, Figure 5.35 shows the mean spectrum for S1-2-24, S2-2-24, S2-2-66, S1-2-99 and S2-5-99 in a.) and T2-2-24,T2-2-66, T1-2-99 and T2-2-99 in b.), where half the sample of T2-2-24 is not present as it is not representative.

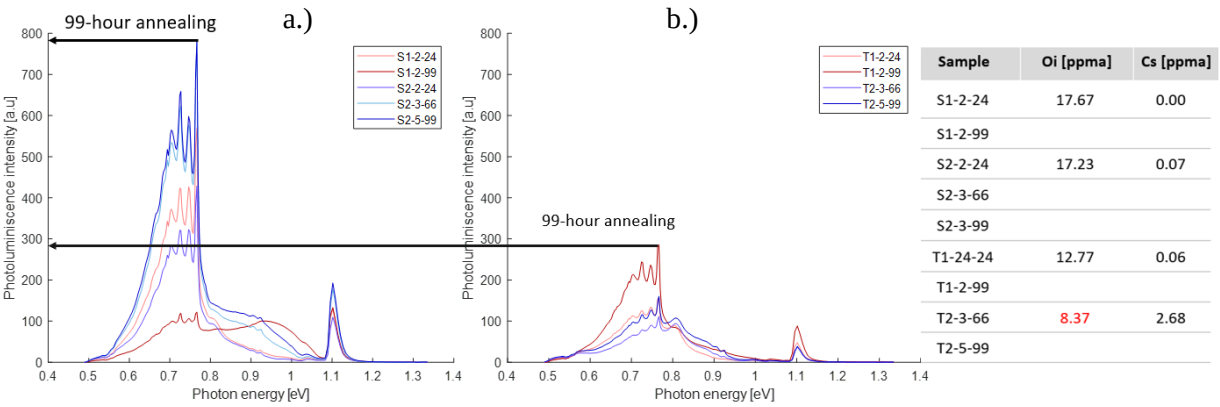

Sample	Oi [ppma]	Cs [ppma]
S1-2-24	17.67	0.00
S1-2-99		
S2-2-24	17.23	0.07
S2-3-66		
S2-3-99		
T1-24-24	12.77	0.06
T1-2-99		
T2-3-66	8.37	2.68
T2-5-99		

Figure 5.35: Mean spectrum for a.) S1-2-24, S2-2-24, S2-2-66, S1-2-99 and S2-5-99 in b.) and T2-2-24,T2-2-66, T1-2-99 and T2-2-99 in. Illustrates the differences in intensity of the DRL between seed and tail end.

The longest annealing time is marked on the highest peaks of sample S2-2-99 and T1-2-99. When comparing a.) and b.) graphs the DRL emission appear significantly lower in tail end samples. In both seed and tail end the highest intensities occur after the 99-hour annealing, but differ strongly in intensity. When observing graph a.) the 99 hour annealing of S1-2-99 stands out as it have a P-line peak at a low intensity. It is important to note that the DRL in this wafer got redistributed between the 24 and 99 hours anneals and it is suspected that the signal has come down from a maximum with much higher intensity. From observing both a.) and b.) it can be concluded that the trend is that the growth rate of the DRL emissions between 0.667-0.767eV occur at a slower rate in the tail end samples. The growth rate of the D1 signal appear less affected by both time and ingot part.

The 650°C annealing of the seed and tail end samples resulted in a very similar evolvement of the DRL emissions. It eliminated the sharp peaks between 0.66-0.74 eV, and Figure 5.36 shows the mean spectrum of a.) S1-2-650 and S2-4-650 and in b.) T1-2-650 and T2-2-650. The only sample that shows a clear reduction in the intensity of the P-line after short annealing is T1-2-650 (see figure 5.23). However, it can be concluded the anneals at 650°C does not eliminate the P-line as this is the only observation in this study where the P-line does not match the generation of thermal donors.

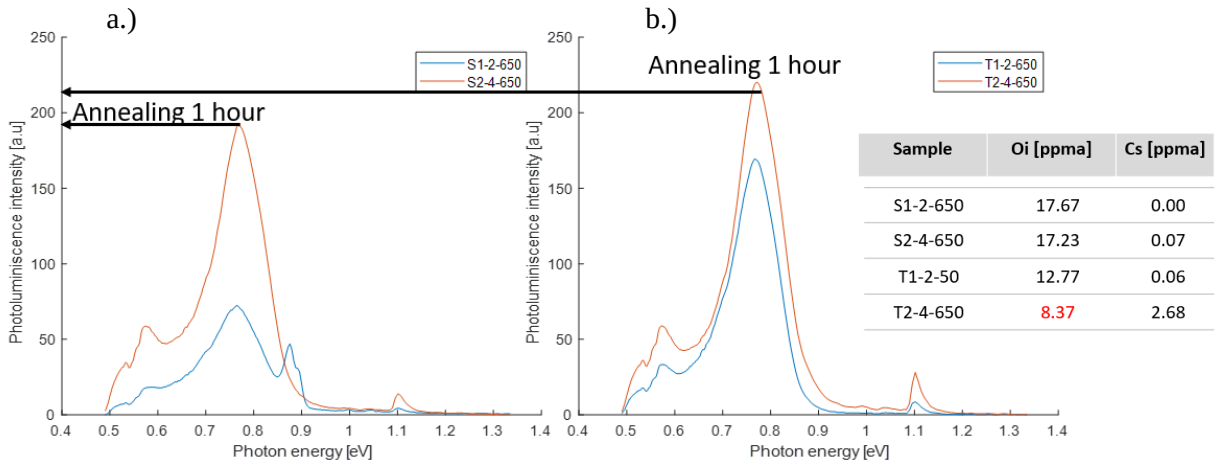

Sample	Oi [ppma]	Cs [ppma]
S1-2-650	17.67	0.00
S2-4-650	17.23	0.07
T1-2-50	12.77	0.06
T2-4-650	8.37	2.68

Figure 5.36: Mean spectrum for wafers a.) S1-2-650 and S2-4-650 and b.) T1-2-650 and T2-4-650. To illustrate the differences in intensity of the DRL between seed and tail end after the 650°C.

If the P-line in fact is due to thermal donors, it is possible that the heating at 650°C for 1 hour was not enough to cause the TDs to diffuse out of the clusters. It is also possible that the TD concentration was not high enough in the wafers before the high temperature annealing. As mentioned in section 2.5.2, Götz reported that low initial TD concentration caused slower decrease in donor concentration at higher temperatures. The progress of the P-line in the tail end sample T2-4-650 support Götz results [21].

The MCR analysis that was performed and presented in section 5.2.1 and 5.3.1 showed that DRL emission with the local peak at the P-line after 650°C was a superposition of multiple peaks. It extracted the D1 as a separate signal in all the samples. This indicate that the annealing of 650°C did not eliminate the D1 signal at 0.807 eV. The D1 signal appear in all the samples after the 24 hour anneal at 450°C and is clearly affected by temperatures at 450°C. As the D1 signal has been connected to dislocations in prior research (section 3) these temperatures do not match the required temperatures to cause dislocations in the wafers and the spatial distribution presented in this thesis do not match the existing literature. Therefor it is suspected that signal detected in this study is another signal at very similar energies as the D1 signal.

The D090 emission and the H-line signal at 0.90eV and 0.925eV formed in all the samples. It took more time for the signal to form in the tail end samples, therefore showed a slower growth rate in

samples with low oxygen content. No connection was found between the H-line intensity and carbon concentration in the samples. Also, the wide band that formed in S1-1-99 and S1-2-99 could be an overlap of the D3-0.934eV and D4-1.000eV signals but this has not been confirmed by the MCR analysis or mean spectra so no conclusion can be drawn. It is more likely that the D09 and H-line has a connection to interstitial oxygen as both emission lines is present at higher intensities in the seed end samples.

Discussion thermal history of samples

From observing the results in this study, it is challenging to tell if any of the differences are caused by the thermal history of the samples. The only annealing process that resulted in a deviation in the DRL emission was the heating of 99 hours of the seed end samples. S1-1-99, S1-2-99 and S2-2-99 showed large differences in the spectral and spatial distribution of the DRL emissions. This could be an effect of the repeated heating and cooling of the samples in the S1 sample sets or possibly be a result of contamination from the steel box. It is hard to completely exclude these two factors but as both samples produced identical spectral responses, it makes it unlikely. All the samples in S1 and T1 sample set were stacked on top of each other and separated by slices of silicon, so if contamination occurred between the S1 samples it should also be expected to influence the T1 samples. This study therefore concludes that contamination neither form the box nor air caused these results as this should have affected the T1 sample sets as well. However, it cannot be ruled out that oxygen present under the annealing process enhanced the growth rate and redistribution of the DRL in the spectral range of 0.667-0.767eV.

Improvements of the study

In hindsight, there are parts of the approach that could have been performed differently and perhaps helped create a more solid result. Among these are using a larger sample set to easier separate deviations that are not representative of the results.

By having a larger sample set the annealing process could have been performed in more stepwise manner and the changes that appeared in the DRL emission could have been monitored more closely, hence giving a more qualitative comparison of the observed growth rates in DRL emissions. It could have helped to identify when maximum of the DRL emission occurred.

A more structured approach could have been beneficial throughout the process of annealing and hyperspectral PL imaging. By performing all the anneals simultaneously, with the same annealing intervals, followed by hyperspectral PL imaging under the same settings etc, this would have eased the comparison between the sample sets.

And lastly, the study presented in this thesis could have been largely improved by using some complementary methods, such as point resistivity measurements or FTIR measurements of O_i along the diagonal of the wafers. At the start of the study one of the objectives was to perform a complementary

method on the samples. This was not possible however due to the thinness of the wafers, thicker samples could therefore have helped improving the result.

6 CONCLUSION

CZ silicon wafers with both high and low interstitial oxygen concentration has been exposed to several annealing steps in the temperature range of thermal donors, where temperatures of 450°C and 650°C was used for generating and eliminating TDs. Hyperspectral PL imaging was performed after each process step, and the spectral and spatial results of the luminescence detected was compared to investigate if links could be found between one or several emission and TDs.

In the unprocessed wafers several DRL emissions was detected at 0.696eV, 0.702eV, 0.724eV, 0.746eV and 0.767eV (P-line.). Before heating the highest intensities could be seen in the samples with high interstitial oxygen and absent in the sample with the lowest concentration. The emissions grew and developed in intensity with annealing time at 450°C. A decrease in the intensity of the signals could also be seen in the one of the oxygen rich samples, and it is suspected that this sample was coming down from a maximum. Other emission lines were detected at 0.90eV and 0.925eV (H-line.) after the first heat treatment at 450°C of 24 hours in the oxygen rich sample, and after 66 hours in the samples with low oxygen concentration. This lead to the conclusion of that all these emission lines had a higher growth rate in the oxygen rich samples. When the wafers were exposed to a 1-hour heating at 650°C the emissions lines at 0.696eV, 0.702eV, 0.724eV, 0.746eV, 0.904 and H-line disappeared, with only the P-line left as a DRL emission in the spectra. The shape of the P-line peak changed character and went from a sharp peak to a peak on broad band. From this it was concluded that as the peaks between 0.696-0.746 was highly affected by heat treatments it was suggested as a possible connection to thermal donors. The P-line was not excluded nor concluded as a signal caused by TD as the 1 hour annealing may not have been sufficient.

Two more unexpected results could be observed from the spectral response. First, the BB luminescence increased with annealing time at 450°C, and this happened for all the sample sets and appeared to follow the same development as the DRL signals in the samples. The cause of this has not been identified but should be looked into in future work, with a heating

process on samples that varies more in oxygen concentration. Second, the D1 signal could be detected in all the samples after the heating at 450°C for 24 hours even though the samples used in this study was commercially produced and considered dislocation free. Neither the spectral or spatial results connected to the signal matched with how dislocation should be distributed in the wafer, hence it was suggested that the signal seen in these results is due to an emission close to the D1 signal.

The results of this study show that hyperspectral imaging can be suitable for tracking oxygen related defects in CZ silicon n-type material. This is confirmed by the many emission lines that became present with heat treatments at 450°C and the possible connection to oxygen. It is difficult to draw conclusions on the origin of the emission lines based on these results alone, but this hypothesis could be further strengthened by performing an annealing process on CZ silicon n-type material together with measurements of both resistivity and interstitial oxygen. By comparing regions with both high interstitial oxygen concentration and low resistivity with the spectral and spatial results obtained by hyperspectral PL imaging, one can possibly create a connection between the emission lines seen in this study and thermal donors. This would be a natural next step take in future studies.

7 REFERENCES

[1] G. Eranna, Crystal Growth and Evaluation of Silicon for VLSI and ULSI, Tayler and Francis Group, LLC, 2014.

[2] C. S. Fuller, R. A. Logan, «Effect of heat treatment upon the electrical properties of silicon crystals,» *Journal of Applied Physics 28.12,* 1957.

[3] W. Kaiser, H. L. Frisch, H. Reiss, «Mechanism of the formation of donor states in heat-treated silicon,» *Physical Review,* 1958.

[4] S. Pizzini, The photoluminescence emission in the 0.7-0.9 eV range from oxygen precipitates, thermal donors and dislocations in silicon, journal of physics: condensed matter 12.49, 2000.

[5] D. K. Schroder, «Number of oxygen atoms in a thermal donor in silicon,» *Journal of applied physics,* 1988.

[6] M. Tajima, P. Stallhofer and D.Huber, «Deep Level Luminescence Ralated to Thermal Donors in Silicon,» *Japanese Journal of Applied Physics 22.9,* 1983.

[7] U. Gösele and T. Y. Tan, «Oxygen diffusion and thermal donor formation in silicon,» *Applied Physics A, 28(2), 79-92.,* 1982.

[8] I. Burud, et al., «Hyperspectral photoluminescence imaging of defects in solar cells,» 2016.

[9] E. F. Schubert, T. Gessmann og J. K. Kim, Light emitting diodes, John Wiley & Sons, Inc., 2005.

[10] S. Rein, Lifetime Spectroscopy: A Method of Defect Characterization." Silicon for Photovoltaic Applications 85, 2005.

[11] D. A. Neamen, Semiconductor physics and devices. Vol. 4, McGraw-Hill, 2012.

[12] C. Hu, Modern semiconductor devices for integrated circuits. Vol. 1, Upper Saddle River, NJ: Prentice Hall, 2010.

[13] G. Coletti, Impurities in silicon and their impact on solar cell performance, Utrecht University, 2011.

[14] W. Lin, The incorporation of oxygen into silicon crystals., Semiconductors and Semimetals. Vol. 42. Elsevier 9-52, 1994.

[15] E. Dornberger, «Thermal simulation of the Czochralski silicon growth process by three different models and comparison with results,» *Journal of Crystal Growth 180 461 467,* (1997).

[16] V. Voronkov, «Grown-in defects in silicon produced by agglomeration of vacancies and self-interstitials,» *Journal of Crystal Growth 310 (2008) 1307–1314,* vol. 2008, 2008.

[17] R. C. Newman, «Oxygen diffusion and precipitation in Czochralski silicon,» *Journal of Physics: Condensed Matter 12.25,* 2000.

[18] P. Wagner and J. Hage, «Thermal double donors in silicon,» *Applied Physics A 49,* 1989.

[19] D. K. Schroder, et al., «Number of oxygen atoms in a thermal donor in silicon,» *Journal of applied physics 63.1,* (1988): 136-141.

[20] V. V. Voronkov, et al., «The Sensitivity of Thermal Donor Generation in Silicon to Self-interstitial Sinks,» *journal of the electrochemical society 147.10,* (2000): 3899-3906.

[21] W. Götz, et al., «Thermal donor formation and annihilation at temperatures above 500° C in Czochralski-grown Si.,» 1998.

[22] T. Niewelt, et al., «Interstitial oxygen imaging from thermal donor growth—A fast photoluminescence based method,» *Solar Energy Materials and Solar Cells 131,* (2014): 117-123.

[23] N. S. Minaev and A. V. Mudryi, «Thermally-induced defects in silicon containing oxygen and carbon,» *physica status solidi (a) 68.2,* (1981): 561-565.

[24] T. Mehl, et al., «Oxygen-related defects in n-type Czochralski silicon wafers studied by hyperspectral photoluminescence imaging,» *Energy Procedia 124,* (2017): 107-112..

[25] N. A. Drozdov, A. A. Patrin and V. D. Tkachev, «Recombination radiation on dislocations in silicon,» *Jetp Lett 23.11,* (1976): 597-599.

[26] E.C. Lightowlers and V.Higgs, «Luminescence Associated with the Presence of dislocations in silicon,» *physica status solidi (a) 138.2 ,* (1993): 665-672.

[27] S. Pizzini, et al., «Luminescence of dislocations and oxide precipitates in Si,» *Solid State Phenomena. Vol. 95. Trans Tech Publications,* 2004.

[28] G. M. Wyller, «Correlation of defect luminescence and recombination in multicrystalline silicon,» *MS thesis. Norwegian University of Life Science,* Ås, 2015..

[29] A. Juan and R. Tauler, «Multivariate Curve,» i *Practical Guide to Chemometrics,* Taylor & Francis Group, LLC, 2006.

Norges miljø- og biovitenskapelige universitet
Noregs miljø- og biovitskapelege universitet
Norwegian University of Life Sciences

Postboks 5003
NO-1432 Ås
Norway